PHD

Optical Drilling of the Human Nail Plate to Facilitate Transungual Drug Delivery

Vanstone, Simon

Award date:
2017

Awarding institution:
University of Bath

Optical Drilling of the Human Nail Plate to Facilitate Transungual Drug Delivery

A thesis submitted by

Simon Vanstone

for the degree of Doctor of Philosophy

University of Bath

Department of Physics and Department of Pharmacy & Pharmacology

May 2017

Abstract

The nail plate is a thick, tightly bound structure that protects the underlying nail bed from water loss, physical abrasion and infections. Despite its barrier properties, organisms are capable of traversing across and around the plate causing infection to the nail unit. Nail disease represents a time and cost intensive problem for the healthcare industry, with current topical and systemic treatment methods failing to stop the rise in incidence. Physical poration of the nail plate is discussed here with the first use of a femtosecond pulsed, fibre optic delivered, visible-light laser for drilling.

Optical, Scanning Electron (SEM) and Atomic Force (AFM) microscopies were used to characterise the physical appearance of the nail plate before drilling. In addition, Fourier Transform Infrared (FTIR) and Raman spectroscopies were employed to investigate variation in the chemical structure of the nail plate across its thickness.

Poration of the nail plate was facilitated using a dye to increase absorption of the laser radiation. Pores were drilled to various depths and widths by varying the amplitude of light pulses and exposure time. Incorporation of an optical chopper into the setup reduced thermal damage to the surrounding nail tissue. The geometry of pores, and the damage to the tissue surrounding them, was characterised with optical, electron and confocal microscopies.

A novel technique to measure thermal damage surrounding the pore was developed. An empirical relationship between the Raman scattering and the temperature was established for nail pieces heat-treated at specific temperatures. This relationship was used to create temperature maps across porated areas. It was revealed the centre of pores were drilled by plasma-mediated poration, whilst thermal effects were responsible for removing material around the edges and damage to the remaining tissue.

Verification of drilling as a suitable technique to reduce the resistance of the nail to topical delivery, was demonstrated with the delivery of caffeine across nail samples. Poration through the entirety of the plate effectively circumvented the barrier provided by an intact, untreated sample. Partial poration reduced the lag time for diffusion across the plate thus speeding up the drug delivery process.

Acknowledgments

Firstly, I would like to thank my two supervisors Sergey Gordeev and Richard Guy for their support, advice and patience. Both have always made time to help me with any problems I encountered during my PhD.

A special thanks to Sarah Cordery who not only taught a clumsy physicist how to use a pipette but has given plenty of her time discussing and reading my work. Many others assisted me over the course of the 4 years in a variety of way, including Hazel Garvie-Cook, Peter Holt, Begoña Delgado-Charro, Wing Sin Chiu, John Mitchel, Ursula Potter, Phillip Fletcher, Anne Gesell, Jim Stone, and Joana Martir.

I would like to thank the EPSRC for funding my project.

Lastly, I would like to thank my parents Jane Vanstone and Brandon Turk. They devoted time and attention to ensure I was interested in the world around me, pushed myself to the best of my ability and have always provided support when needed.

Contents

Abbreviations & Definitions

Acronyms & Expansions

AFM	Atomic Force Microscopy
FTIR	Fourier Transform Infrared Spectroscopy
HPLC	High-Performance Liquid Chromatography
LSCM	Laser Scanning Confocal Microscopy
NR	Nile Red
RR	Ruthenium Red
SEM	Scanning Electron Microscopy

Acronyms, Expansions & Definitions

CCD	Charged coupled devices	Multichannel array detector of light used to detect Raman scattering
CRI	Characteristic Raman Intensity	The sum of the intensity beneath a Raman spectra between two points
HC-PCF	Hollow Core Photonic Crystal Fibre	Optical fibre with the ability to guide femtosecond pulsed laser light
MIC	Minimum Inhibitory Concentration	Lowest concentration of a chemical that prevents infection an antimicrobial that will inhibit the visible growth of a microorganism following overnight incubation
PBS	Phosphate Buffered Saline	Water-based salt solution buffer

Chapter 1

Introduction

The integumentary system protects the body from water loss, physical abrasion and infections. One component of this system is the nail; the unit consists of a transparent, many layered, dead keratinaceous plate atop the nail bed. Unlike the skin covering the rest of the body, the nail bed lacks a stratum corneum, the protective outer layer of the epidermis, and so relies on the nail plate as a barrier. Despite this, organisms are capable of traversing the plate causing infection to the bed or plate itself; the most prevalent onychomycosis affects 2-10% of the population.

Two primary treatments are currently prescribed: oral systemic and topical. Unfortunately, both treatment methods have signification drawbacks. Oral therapy requires a long duration of treatment and has a high relapse rate, incompatibility with other medication is also an issue for vulnerable populations including the elderly and those suffering from immuno-compromising diseases. Topical therapies include drug-containing lacquers, solutions and gels, which all have low efficacy. The poor permeation across the nail plate (transungual) results in an insufficient concentration of the drug reaching the bed to kill the infecting organism.

Efforts to cure nail disease has seen a large body of research, with multi-billion dollar expenditure. In addition to the development of new topical and oral drugs, alternative techniques are being developed to solve the problem. One potential solution, optical drilling of the plate with a laser, uses a focused beam of energy to ablate tissue, leaving pores for a topically applied drug to permeate directly to the bed. This technique has been extensively studied as a method to overcome the skin barrier, but as yet, research into

laser poration of the nail is minimal. The attempts at poration have used CO_2 lasers to burn holes into the plate, but thermal damage associated with the long pulses caused discomfort to the patients and required post-operative management.

The heating problem can be solved through the use of pico- or femtosecond pulses. These ultrashort pulses are capable of removing tissue with minimal thermal damage to the surroundings. In contrast to the photothermal mechanism of long pulses, ultrashort pulses remove tissue by a plasma mediated mechanism in which the radiation causes breakdown and ejection of tissue in a confined volume. Thanks to recent advances in fibre technology, visible wavelength ultrashort pulses can be guided and delivered with great precision, thus making potential clinical use easier and safer.

Characterisation of the nail, before and after poration, is important for interpreting the beam tissue interaction. Imaging techniques including optical, Scanning Electron (SEM), Atomic Force (AFM) and Laser Scanning Confocal Microscopies allow the study of the nail plate from a macroscopic level down to nanometre resolution. Raman microspectroscopy has seen increased use for studying biological materials. Modern systems possess the ability to study chemical structure with a 1 μm resolution. Furthermore, detected Raman spectra have previously shown sensitivity to thermally-altered materials and so the technique has potential to quantitatively analyse thermal damage. This is of special interest as there are currently no techniques to measure burning or damage to a porated nail, preventing quantitative comparison between different laser systems.

This thesis discusses the development of a technique to optically drill nail, with a view to improving transungual delivery. Femtosecond pulsed, fibre guided visible light was used to fractionally ablate the nail leaving behind pores into and through the plate. These pores were characterised using microscopy and spectroscopy techniques to obtain insight into the mechanisms governing the interaction and the effects on the surrounding tissue. Raman microscopy was used to develop an empirical relationship relating the intensity of signal measured to the temperature from nail pieces that had been heat-treated at specific temperatures. This allowed the generation of temperature maps around the pore and optimisation of laser parameters to drill the nail. Samples were prepared for permeation experiments by drilling plates with arrays of pores, and caffeine was used as a model drug to test the effectiveness of the technique.

Chapter 2 provides a background of material relevant to this thesis. It opens with a discussion of the nail's anatomy and physiology, the diseases that can affect it and an overview of treatment strategies currently in clinical use and those being developed. Following this, laser poration of tissues including nail and skin are discussed. Finally, an overview of Raman and AFM is given, including the principles behind their operation and their use on biological tissue. Chapter 3 contains the materials and methods used for all studies in the thesis, including preparation of nail plate for microscopic study and the setup of the laser system for poration.

A detailed microscopic study of the nail plate was conducted to provide an understanding of the structure. Chapter 4 presents data from the surfaces of nail plates, their cross section and individual cells isolated by tape stripping. Optical and SEM images were used to study the layered structure. AFM provided the means to investigate nanometre scale details. Fourier Transform Infrared (FTIR) and Raman spectroscopies were employed to investigate whether the chemical structure of the nail plate varies across its thickness.

Chapter 5 details the development of an optical drilling technique. The appropriate selection of a dye that strongly absorbed visible light was important to entrap radiation in a small focal volume. Upon selection of an ink, a study of the laser parameter's effect on pore geometry, and the damage caused to the surrounding region was conducted. The introduction of an optical chopper allowed variation to the grouping of pulses delivered onto the nail. These studies provided a series of parameters for the preparation of samples for permeation experiments.

Chapter 6 describes the novel use of a Raman microscope for mapping the thermal damage caused by drilling. Raman spectra were obtained for *in vitro* nail pieces deliberately heated in the furnace. This allowed an empirical relationship between the background intensity signal and temperature of treatment to be established. Cross-sections of pores were prepared and two-dimensional arrays generated using the Raman microscope to record the intensity at each point. Subsequently, these data were used for the creation of two and three-dimensional temperature maps leading to further understanding of the mechanism of poration.

The efficacy of optical drilling as a method for reducing the nail barrier was tested in Chapter 7. A model drug, caffeine, was chosen for delivery across *in vitro* nail samples which were either intact, had pores that stopped inside the plate or pores that fully

penetrated the plate. Sampling of the permeated caffeine was quantified with high-performance liquid chromatography.

Chapter 8 summarises the work performed, and draws conclusions on the findings. There are also suggestions for further work that would develop this technique for use in a clinical setting.

The work presented in this thesis describes the use of techniques to study the nail plate before and after optical drilling. Optical drilling of the plate with femtosecond pulsed, fibre optic delivered, visible light provides a controlled method to remove tissue. Optimisation of the drilling mechanism allows partial or full poration of the nail plate, whilst minimising thermal damage to the regions surrounding. Raman microscopy provided a useful tool to analyse the drilling mechanism. The permeation of caffeine was seen to increase drastically as complete poration effectively circumvents the nail plate barrier. Partial poration of the plate offers a unique opportunity to enhance permeation whilst easing post-operative management.

Chapter 2

Literature Review

2.1 Nail structure

2.1.1 Purpose and Function

The nail unit covers the upper part of the distal end of the human phalanges. Figure 2.1 displays the nail unit from above, and a cross sectional view. The nail has several functions, it protects the tips of the fingers and toes from blunt trauma, allows manipulation of fine objects, enhances the sensation of touch and is used for scratching and grooming. It starts to develop in the 9^{th} week of embryogenesis, by week 14 the plate starts to emerge from beneath the proximal nail fold and after 17 weeks it covers most of the nail bed [1].

2.1.2 Anatomy of the Nail

Nail Matrix

The nail matrix is a germinative tissue, which is comprised of layers of cells that divide to form the nail plate [2]. The process by which cells divide and migrate distally is known as terminal differentiation. During migration, the cuboidal shape of the divided cells is flattened and nuclear fragmentation occurs. At this point, the cells are considered to be nail plate cells, onychocytes. At the site of growth of the nail plate, the size and shape of the matrix influence the shape of the plate. The zones of growth in the matrix can be split

into three sections; the dorsal, intermediate and ventral [3]. The lunula, the white semi-circle observed in some digits, is the end of the matrix.

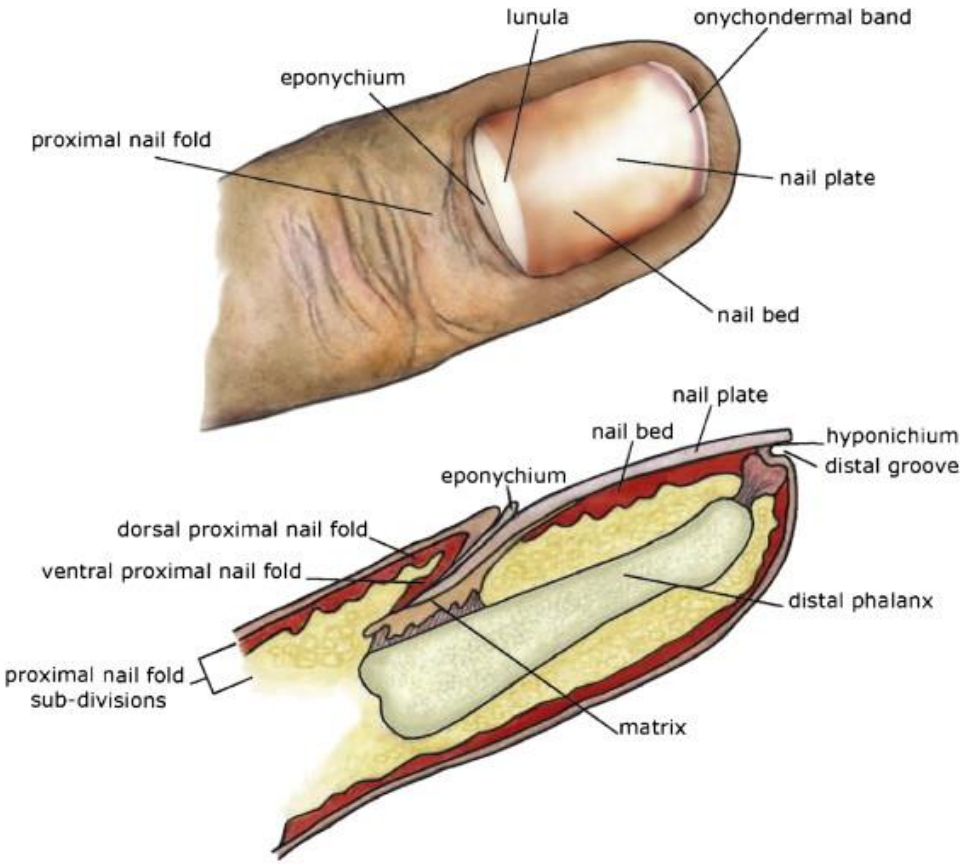

Figure 2.1: *Cross-section displaying the components of the nail and its attachment to the underlying phalanx. Reproduced from [4] with permission.*

Nail Bed

The nail bed is the skin region immediately beneath the nail plate. Unlike the skin located on the rest of the body, the dermis underlying the nail bed attaches directly to the periosteum with no subcutaneous fat present. Another difference from normal skin is the lack of a stratum corneum, the outer protective layer. In fact, the epidermal region overlying the dermis is only 2-3 cells thick. However, this region contributes to forming a protective barrier; the epidermal cells rapidly differentiate and integrate into the ventral region of the nail plate [5]. Longitudinal ridges in the dermis of the bed interlock the ridges on the ventral surface of the plate and provide the strongest site of attachment for

the plate to the nail apparatus. The nail bed is well vascularised, with a network of arteries responsible for the pink appearance through the translucent nail plate.

Nail Folds

Seventy-five percent of the nail plate is enclosed by the proximal and lateral skin folds. The proximal nail fold is a continuation of the skin on each digit and forms the eponychium or cuticle. The cuticle aids in the protection against foreign material entering the nail matrix, by firmly attaching to the surface of the nail plate. The lateral nail folds are a continuation of the skin from the side of the digits and attach medially to the nail plate. The skin comprising the folds is similar to the epidermis of the normal skin, but has no hair follicles or sebaceous glands.

Nail Plate

The nail plate is a hard, transparent structure that lays atop the nail bed. It is curved in both the longitudinal and transverse directions and inserts under the nail folds. Age, site and gender are all factors that influence the properties of the nail plate such as its size, shape, thickness and mechanical properties. An investigation into the number of layers in the nail found 134-226 cells across the thickness of the toenails plates, these measured between 500-1340 μm [6]. The growth of the plate is different for fingernails and toenails. Fingernails grow at an average rate of 3mm/month whilst toenails grow at 1 mm/month. As a consequence, fingernails are replaced in 6 months, while toenails take between 12-18 months to grow through[7].

The three zones of growth in the matrix correspond to the three loosely defined layers of the nail plate. There is variation in the proteins and lipid content across these layers. The plate is primarily protein, specifically keratin. Both of the two types of keratin that exist in the human body are present in nails: epithelial skin type keratins and hair type keratins [8]. There is an 80-90% majority of the hair type [9]. As a result the nail is harder than the skin due to the higher content of cysteine - an amino acid which forms chemical cross-links between filaments and the non-filamentous matrix- present in the hair type keratin. However, hair keratin is only present in the intermediate layer [10]. Scanning Electron Microscopy (SEM) has revealed that the dorsal surface is flat with cell edges overlapping

and no apparent gaps in the plate. On the other hand, the ventral surface is rough with more free edges and less overlapping. This structure enables the tight binding between the nail bed and plate [11].

The lipid content of the nail is less than 1% w/w, compared to the stratum corneum which contains 10% w/w. Despite this lipids demarcate the plate well when stained. Figure 2.2 displays an optical image of a nail plate stained with Sudan Black B. Most of the lipid content in the dorsal and ventral regions of the nail with a 3:5:2 ratio for the thickness of the dorsal, intermediate and ventral layers [12]. The nail plate cells are tightly bound, but the space between onychocytes was identified under an electron microscope. It measures 25-35nm; this space is filled with a cement thought to contain protein & polysaccharides [13]. In the dorsal region, the cement completely fills the space between the cells, but is discontinuous in the intermediate region.

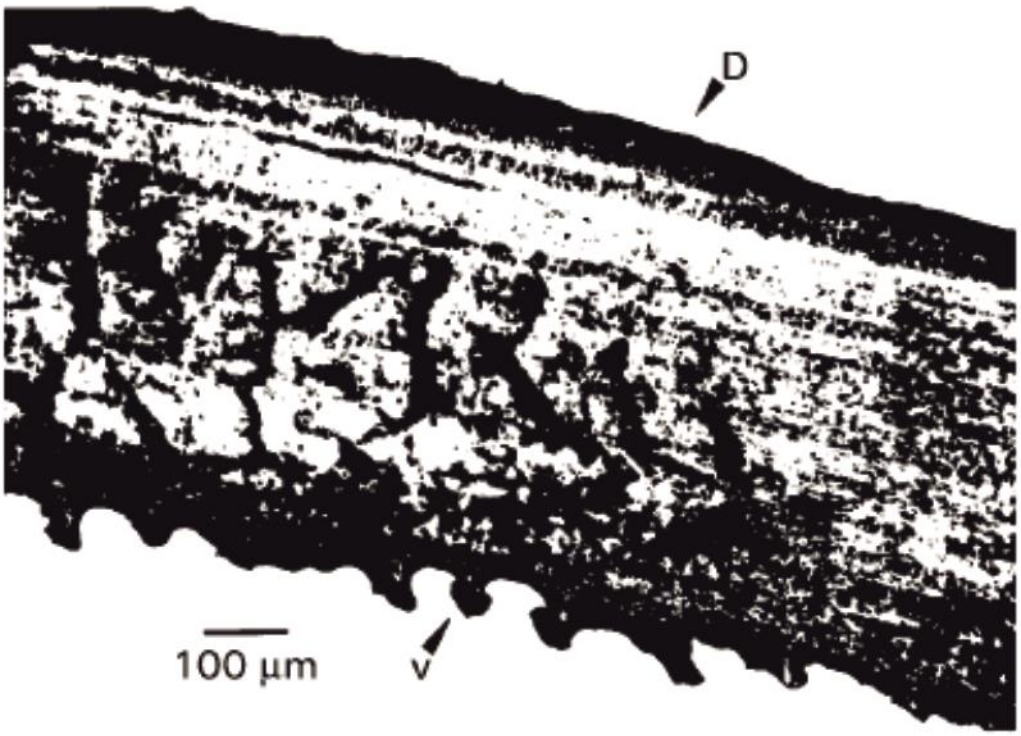

Figure 2.2: Optical image of a nail plate stained with Sudan Black B, which stains most lipids. The majority are concentrated in the dorsal region, D, and ventral region, V. Reproduced from [12] *with permission.*

Water is also present in the nail and acts as a plasticiser, increasing the nail's flexibility and elasticity [11]. The amount present varies between volunteers and depends on

environmental conditions such as the humidity. For instance, the water content in the nail has been reported at 8-22% and 5-30% w/w [14,15]. Water in contact with the nail is rapidly absorbed causing the nail to swell in size.

2.2 Nail Disease

Diseases that affect the nail have become increasingly prevalent, with the elderly, diabetics and immunocompromised especially vulnerable to infection. Contributing factors include tight fitting shoes, the increased use of damp communal spaces such as locker rooms and the declining health of the growing elderly population. Nail disease cannot be considered a minor cosmetic problem, it has been reported to impact on patient's emotional, social and occupational functioning. The embarrassment of a disfigured nail unit and a fear of spreading the infection to others can make social interaction difficult for sufferers. Sufferers may face discrimination from employers who will not hire individuals with abnormal nails, especially in roles that involve face to face interaction with customers such as the food or fashion industries. In addition, physical discomfort can be experienced by those who are required to stand for long periods of time, or sufferers who must type or write for long periods of time [16]. The two most common diseases, onychomycosis and nail psoriasis, will be discussed in greater detail below.

2.2.1 Onychomycosis

The most common nail disease is onychomycosis; it is a fungal infection caused primarily by dermatophytes, although yeasts and moulds are responsible for some instances. Onychomycosis can manifest in different ways depending on where the fungus infects the nail. As a result, four clinical classifications have been assigned [17].

Distal and Lateral Subungual Onychomycosis (DLSO)

DLSO is the most common form of fungal infection of the nail. It occurs when the nail apparatus is invaded at the underside of the plate at the hyponychium. As a result, the distal and lateral nail bed is infected, as is the underside of the plate overlying these regions. If left unchecked the invading organisms migrate proximally through the bed, infecting the plate from its underside as it progresses. Additionally, microscopic studies have revealed, tunnels through the nail plate, along which the microorganisms have migrated. The spread of the disease causes onycholysis, a process in which the nail plate detaches from the nail bed, leaving a thickened subungual region. The yellow/brown appearance of the nail is caused by the space between the nail bed and plate filling with bacteria and moulds.

White Superficial Onychomycosis (WSO)

WSO accounts for 10% of cases of onychomycosis [18]. It occurs when the plate is directly invaded by fungi; this causes well-delineated opaque white islands to form on the dorsal surface of the nail plate. Unless treated, these regions coalesce with the entire surface becoming rough, soft and crumbly. Fortunately, inflammation is unusual for those affected, since no viable tissue is involved with WSO.[19]

Proximal Subungual Onychomycosis (PSO)

PSO occurs when fungi penetrate through the proximal nail fold and under the cuticle. Consequently, a white discolouration of the lunula is observed in the newly formed plate. The infection moves distally across the nail apparatus as the nail plate grows out. Furthermore, microscopic slits occur in the plate which causes onycholysis and destruction of the proximal plate. PSO is the most infrequent form of onychomycosis, but is common amongst AIDS sufferers. A study found that 54 out of 62 patients with AIDS or HIV presented with PSO [20]. Thus, PSO might be useful as an early clinical marker for HIV.

Total Dystrophic Onychomycosis (TDO)

If the aforementioned cases of onychomycosis are left unchecked to spread and infect the entire nail bed, TDO occurs [21]. Therefore, it is considered as the endpoint for all forms of onychomycosis. Extreme nail alteration occurs, the entire plate can crumble off, revealing a thickened and abnormal nail bed beneath.

2.2.2 Nail Psoriasis

Psoriasis is a chronic, incurable, skin disease that causes significant tissue distress. The disease is most common in Caucasian patients, with a greater prevalence in those living at higher latitudes. Psoriasis affects an estimated 2.1 to 2.6 % of the population in the US (4.5-7 million people), with this number rising to 3% in Canada (over 1 million) [22]. Moreover, 50% of patients presenting with skin psoriasis show nail psoriasis. In fact, 80-90% of those with skin psoriasis will suffer an incidence of nail psoriasis at some point during their lifetime [23]. Psoriasis affects different structures within the nail, resulting in a variety of dystrophies related to the disease. Firstly, pitting, the most common dystrophy involves regions of the plate becoming depressed as poorly bound onychocytes flake off. Psoriatic lesions within the matrix are the cause of pitting. Although pitting occurs in other diseases of the nail, the pits are typically deeper for those who suffer from psoriasis. Secondly, ‘oil-drop’ discolouration of the nail plate causes it to appear salmon coloured. Thirdly, the plate-bed border region can experience both onycholysis and subungual hyperkeratosis, the deposition and collection of cells under the nail plate. Finally, psoriatic nail folds result in paronychia, a soft tissue infection which causes ridging to the nail plate [24].

2.3 Current Treatment Methods

The treatment of onychomycosis, psoriasis and other diseases is a challenging prospect. Low cure rates and high re-occurrence rates even after the disease has apparently cleared, are reported [11]. This results in a huge time commitment from medical professionals in the treatment of diseases. Financial investment in the treatment of nail disease is vast,

with an estimated $2.1 billion being spent on the dermatophytic onychomycosis market in the USA in 2010 [25]. With the exception of simply removing the plate, two treatment regimens are commonly used. The first technique is topical treatment; a formulation containing the drug is applied to the surface of the nail, the drug then diffuses into the plate. However, due to the nail's effective barrier properties, the permeation of the drug is generally low. The alternative is systemically treating the disease using oral medication. Although success has been seen with systemic treatment, several problems exist: medication courses are long, side effects are common and interference with other prescription drugs results in unsuitability for many of those affected. More recently, devices that reduce the barrier properties of the nail and make topical treatment a more effective option have been developed. An explanation of these treatment options is given below.

2.3.1 Nail Avulsion

The simplest way to treat nail disease involves the partial or total removal of the nail plate, either with surgery or chemicals. Nevertheless, most patients wish to avoid this unattractive option, due to the painful and disfiguring nature of the operation it is only used in severe cases. Chemical nail avulsion involves the use of keratolytic compounds such as urea and salicylic acid. These compounds work by softening the plate, which eases its detachment from the nail bed [26,27].

2.3.2 Systemic Therapy

Systemic therapy via oral administration is the most common approach for the treatment of onychomycosis. After ingestion, the drug enters the blood stream diffusing through blood vessels, into the matrix and nail bed, from where it progresses into the nail plate [28]. Due to the extreme location of the nail apparatus, a large dosage of the drug is required to achieve a sufficient concentration at the infection site to kill the fungi. In addition, extended medication courses are needed to eradicate these resistant diseases, which requires a high level of patient compliance.

Griseofulvin represented a promising advance in antifungal treatment when it was first used nearly 60 years ago. Griseofulvin works by forming a barrier in the nail matrix against fungi, as the plate grows out the barrier continues to build in the new nail. In the 1980s the first orally active imidazole, ketoconazole, was developed. Ketoconazole is effective against a broad spectrum of invading organisms including; dermatophytes, yeasts and several moulds. However, the long-term usage of ketoconazole is limited by serious side effects and significant drug interactions [18,29,30]. The newer formulations such as itraconazole, fluconazole and the allylamine, terbinafine, affect the fungi membrane permeability. This results in lysis, a process during which the cell disintegrates after leakage of the cellular contents.

Treatment with systemic therapy still leaves much to be desired. Despite the availability of these drugs, treatment failure is common, with studies quoting 30% of patients failing to respond [31,32]. This high failure rate is due to several problems. Firstly, drug resistant fungal spores lie dormant during treatment and can become active, re-infecting the nail after apparent clearance of the disease. Secondly, disease-induced changes to the nail plate such as thickening or extensive onycholysis, prevent the drug from reaching the target site. Thirdly, poor patient compliance is an issue which, given the length of treatment, is unsurprising. These factors combined with the significant drug interactions that occur with other medication leave many of those affected by nail disease requiring alternative treatments.

2.3.3 Topical Therapy

Topical therapy involves the application of a formulation to the surface of the nail. Topical therapy is often combined with oral treatment and monotherapy is generally only used to treat mild infections when there is no matrix involvement and less than 50% of the distal end is infected [33]. However, in instances where systemic drugs are inappropriate for treatment, topical therapy provides an alternative solution. After application of the formulation to the nail surface, the drug is expected to diffuse across the plate and into the nail bed. The first concern for effective topical treatment is reducing the loss of formulation from the nail surface due to routine activities [34]. The next requirement is for the concentration of the drug permeating across the nail plate to be

greater than the minimum inhibitory concentration (MIC). The rate of drug permeation across the nail plate is dependent on the permeant properties, the characteristics of the formulation and the properties of the plate.

Permeant Properties

Three permeant properties affect drug diffusion across the nail plate: molecular weight, charge and lipophilicity of the permeant. The most significant property is the molecular weight; permeation significantly decreases as the molecular weight increases. Drug molecules must navigate narrow and tortuous pathways through the dense keratin network in the nail plate. As smaller molecules pass through this with less interactions they move across the barrier more quickly. It was found that the molecular weight of a drug is inversely related to its permeation [35].

Another key parameter for passive diffusion across the nail plate is the charge of a permeant. Non-ionic drugs were found to have a ~10 fold greater permeability than ionic drugs [36], regardless of the charge. There are several theories for this, one of which involves hydration of the ionic agents, with the resultant increase in apparent molecular weight reducing permeability. The other is attributed to the "Donnan effect", whereby the charged keratin membrane repulses the charged molecule of ionic drugs [37]. Regardless, delivery of a non-ionic permeant is desirable.

The lipophilicity of the drug is also thought to influence permeation. The permeation of homologous alcohols with increasing chain length and lipophilicity has been investigated [38]. The nail plate is hydrophilic and so, generally, the permeation rate decreases with an increase in carbon-chain length or lipophilicity.

Formulation Characteristics

The characteristics of the formulation impact the diffusion of the drug by causing changes to the plate. The strongest changes occur to the nail plate due to the formulation's water content [39]. The nail swells, and the keratin expands, due to uptake of water by the nail. Hence, larger spaces are available between cells for the drug to travel through. A 5-fold increase in the permeability coefficient for alcohols diluted in saline, compared with neat

alcohol, across the plate has been demonstrated [38]. As well as directly adding water, formulations affect the distribution of water already in the nail plate. For example, water loss from the nail surface to the atmosphere is reduced by polymeric films. Water is trapped in the upper layers of the plate, increasing hydration and diffusion. In addition, drug-resistant spores germinate into drug-susceptible hyphae, which will be eradicated [40].

The pH of the aqueous vehicle is an important factor in drug diffusion because of its effect on ionisation; avoiding ionisation of the permeant is desirable. A general rule governing ionisation is that basic drugs remain unionised at high pH values and that acidic drugs remain unionised at low pH values. Consequently, acidic drugs permeate best in formulations with a low pH and basic drugs permeate best in high pH formulations [41,42].

Nail Plate Properties

Topical diffusion is heavily influenced by the properties and condition of the nail plate. As discussed, infection results in changes to the plate's structure; thickening of the nail plate, separation of the plate from the bed (onycholysis) and the plate becoming crumbly. Thickening of the plate will result in a longer pathway way for the drug to traverse and lower permeation across the plate. If onycholysis has occurred and the plate is separated from the bed, the drug will struggle to pass from the nail into the bed. However, when the distal edge is the site of detachment, the formulation can be applied directly into space beneath the plate: aiding treatment [11]. In contrast, crumbling of the plate increases porosity, resulting in a rise in permeability. Kobayashi et al investigated the permeation for 5-fluorouracil across diseased nail plates [36]. Unfortunately, this study excluded heavily diseased plates amid concerns they would crumble in the solution; healthy and mildly affected plates showed similar levels of permeation. It has been postulated that these factors account for the large variation in clinical outcomes of topical therapy.

2.3.4 Topical Therapy - Current Formulations

Current topical therapies for the treatment of the nail plate include lacquers, solutions, semisolids, films and nail powders. Nail lacquers were developed from conventional

beauty products designed for the nail. Several reasons led to lacquers becoming the preferred topical formulation: the long residence time on the nail surface, their aesthetically pleasing appearance and patient familiarity with the application [43]. When applied to the nail with a brush the medicinal lacquers require several minutes to dry, leaving a water-insoluble polymeric film on the surface of the nail. Meanwhile, the high drug concentration drives trans-ungual delivery from the lacquer across the nail plate.

Currently, the two most popular active ingredients used for nail lacquers are amorolfine and ciclopiroxamine. Loceryl (Galderma, Belrose, Australia) is a lacquer containing amorolfine; it is applied once a week for up to six months on fingernails and 9-12 months for toenails [44]. Penlac (Valeant Pharmaceuticals Inc, Bridgewater, USA) is a ciclopirox based lacquer; it requires a daily application for up to 11 months [45].

Nail solutions are highly concentrated, containing the active drug in a solvent. The choice of solvent is important due to its effect on the penetration of the drug. For treatment, solutions are applied to the surface of the nail with a brush and allowed to dry. Unlike nail lacquers, solutions do not always form a film on the surface. The efficacy of topical solutions is hampered by the poor penetration of active ingredients into the nail unit; debridement of the nail surface through clipping or filing is recommended before application of most solutions.

Tioconazole is an imidazole derivate used in topical monotherapy of the nail, with Trosyl© (Pfizer, Tadworth, Surrey) the best-known brand in the UK, Ireland and Canada [46]. Treatment is recommended for 6-12 months and cure rates varying from 20% to 70% have been reported in studies.

A variety of semisolid formulations has been developed to treat nail disease: gels, ointments, creams, lotions, films and patches. Gels are the most popular semisolid formulation. The main reason is the increased hydration resulting from the water content of gels. The penetration of Ciclopirox derived from a marketed gel and a marketed lacquer, along with an experimental gel has been tested *in vitro* [47]. The marketed gel showed the highest penetration into the nail plate. However, gels are easily removed from the surface of the nail during the day-to-day activities. In contrast, ointments have so far had limited application to the nail due to their hydrophobic nature. Generally, creams are not used for onychomycosis unless it is superficial in nature, but they have been found to be useful in treating psoriatic nails [48]. One percent 5-fluorouracil was used on nails in

which nail thickening and pitting were the major issues, but were suggested as inappropriate if onycholysis was a major feature [49] In addition, topical steroids are useful in the treatment of psoriatic changes in the nail fold [50]. Recently, the use of films and patches have been investiged; these may allow application of a concentrated drug to the nail surface for a prolonged period [39].

Despite the time and financial commitment to development, topical therapy leaves a lot to be desired. The drug concentration in the nail is often greater than the quoted MIC required to treat the disease, yet the disease is still present after treatment. It appears a steep gradient of concentration leaves the dorsal layers saturated whilst minimal drug reaches the deeper layers. A considerable amount of drug is unavailable due to binding with keratin in the plate, and so the real MIC is probably much higher than those calculated in standard media. In conclusion, current topical treatment although suitable in some instances cannot be considered as a complete solution to nail disease [51].

2.4 Enhancing the Nail Plate Permeability

The issues associated with systemic and topical therapies have led to a great deal of research to increase permeation across the nail barrier. The techniques can be those that are based on chemical alteration of the plate or which physically reduce the barrier.

2.4.1 Chemical Treatments

The first chemical treatments used on the nail were those that had been shown to facilitate permeation across the skin [38]. However, most of these work by enhancement of the lipid pathway; the low lipid content of the nail plate meant that little impact is seen in transungual delivery. The focus has since shifted onto disrupting the keratin matrix. This is achieved by cleaving of the chemical bonds that give the nail plate its strength. The disulphide bond has received the most interest due to its key role in nail stability. Thiols (-SH containing compounds), sulphites and hydrogen peroxide have all shown success in cleaving the bonds, resulting in an increased permeability [11,52,53].

2.4.2 Physical Treatments

Most physical techniques work by shortening the distance drug has to travel to cross the nail. As mentioned, the filing of the nail surface reduces the distance topically applied drugs have to diffuse. Medicinal lacquer packs contain abrasive sticks (emery boards) which the user is instructed to use before application. Filing was essential in clinical trials for successful treatment [54,55]. However there is likely to be considerable variation in the amount of nail plate removed, as the procedure is left in the hands of an untrained operator.

Iontophoresis is a technique to improve drug delivery whereby the application of an electric current across the nail increases permeation. The flux for both uncharged and ionic molecules across the plate increases: uncharged molecules are driven by electro-osmosis; ionic molecules are primarily driven by electro-repulsion, with a small contribution from electro-osmosis. Model drugs that have been delivered across the nail by iontophoresis include salicylic acid, mannitol and urea [56-58]. Antifungal drugs have also been tested, ciclopirox was delivered across the nail with iontophoresis and a 10-fold increase in permeation over passive delivery was observed [59].

Acid etching is a simple technique involving the application of acid to the nail surface [51,60]. Disruption of the dorsal nail plate provides a rougher, microporous surface; the increased surface area is ideal for lacquers or films to bond on. In addition, the membrane thickness is reduced.

Low-frequency ultrasound has been investigated as a technique to enhance permeation in both human nail plates and bovine hoof membranes [61]. The mechanism has yet to be fully understood. It has been postulated that inside the nail gas bubbles form, which collapse and cause micro-jets of liquid to penetrate the membrane. These new routes provide alternative pathways for a drug to travel through the plate.

Microporation of the nail with a hand-held cutting device – PathFormer (Path Scientific, Carlisle, USA) was used to make holes in the nail (Figure 2.3). The depth of the hole is controlled by electrical resistance. An undrilled nail has a resistance of 5 MΩ, when the drill penetrates to the nail bed the resistance drops down to 10-20 kΩ. A topical cream

and a placebo cream were used to treat porated nails [62]. Little detail is given on the number of holes or the depth to which they were drilled, and the lack of a control group in which no holes were formed makes comparison difficult. A study investigated patient compliance when holes 400 μm in diameter were drilled down to resistances between 25-90 kΩ [63]. The treatment was well tolerated by patients with no pain issues reported. The biggest drawback for the PathFormer is the time taken to drill multiple holes.

Another physical microporation technique was performed with a Derma Roller (Infinitive beauty®, Birmingham, UK): a device consisting of 250 μm long titanium needles designed for poration of the skin [64]. The derma roller was rolled across a nail plate, and a fluorescent dye (Nile Red, NR) applied. The movement of the dye molecules through the plate was recorded with Laser Scanning Confocal Microscopy (LCSM), as shown in Figure 2.4. Permeation was enhanced, when in comparison to control nails, and the pores provided a reservoir for the NR to diffuse laterally and deeper into the plate.

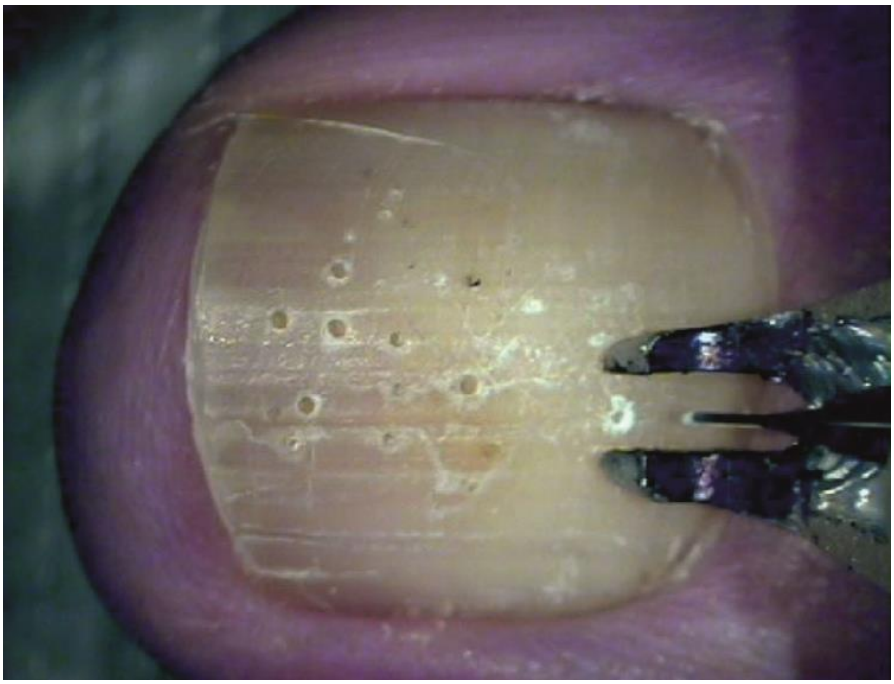

Figure 2.3: Photograph showing drilling of holes in the nail plate using the PathFormer [65].

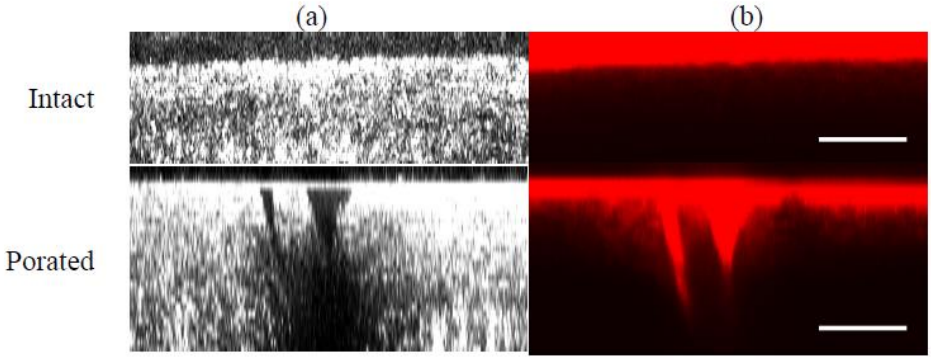

Figure 2.4: Reconstructed cross-sectional images recorded 48 hours after the application of NR loaded nanoparticles to intact and microneedle-porated nails as a function of depth. a) Displays reflectance signal from the nail plate, whilst b) displays the NR fluorescence. Scale bars = 50 μm. Reproduced with permission from [65].

2.5 Laser Poration

Lasers have been used for medical purposes since Leon Goldman employed a ruby laser to remove birthmarks and melanomas from the skin in 1963 [66]. Fifty years later, surgeons, ophthalmologists and dermatologists consider lasers an important tool in their practices. One area that has seen work in recent years is laser poration of tissue, an ablative process in which tissue is removed as a result of the beam energy. Uses include the resurfacing of skin, to deal with cosmetic issues, or as a technique to bypass a tissue barrier. An important aim with this type of work is to minimise the damage to the surrounding tissue. This has become easier to manage as laser technology has improved, moving from continuous wave lasers to increasingly shorter pulses. Early pulsed laser systems had milli- and microsecond length pulses, which are considered ‘long’ for tissue surgery. The heating caused to tissue by these is similar to the continuous wave lasers. Nanosecond systems proved effective in reducing the heating and burning in tissue, especially with pre-treatment of a dye or ink to stain the target structures [67,68]. With the advent of picosecond pulses, dissection and removal of intracellular components have been achieved [69]. Now, femtosecond pulses are commonplace thanks to passively mode-locked lasers [70].

2.5.1 Light-Tissue Interactions

The nature of the light-tissue interaction is largely dependent on the properties of the laser: the wavelength and the pulse duration. The interactions between laser light and tissue are split into three major mechanisms: photochemical, photothermal and plasma-mediated ablation. The photochemical mechanism is based on the build-up of pressure caused by the photochemical dissociation of macromolecular bonds. Ultraviolet radiation (λ = 180 – 400nm) provides photons with high energies (6.5-3.1 eV), that are sufficient to destroy macromolecular bonds and cause photochemical ablation processes. The peptide bond in proteins is generally the target of UV photons. The photothermal mechanism involves a specific constituent in the tissue absorbing light and being heated. Visible radiation (λ=400-780 nm) is absorbed primarily by melanin and haemoglobin and so it is suitable for pigmented tissues including skin, hair and the eye. In contrast, infrared radiation (IR) (λ = 780 nm – 15 μm) is primarily absorbed by water with significant absorption above λ > 900 nm, although, some protein bond vibrations also absorb IR. Regardless of the wavelength, when radiation is absorbed by chromophores, a local temperature rise occurs with water in the surroundings being vaporised. Subsequently, the mechanical pressure builds up and tissue is ejected, leaving a pore behind.

The pulse duration is the main factor for governing the cut-off between photothermal and plasma ablation; with pico- and femtosecond pulses capable of causing plasma formation. Plasma-mediated ablation begins when photons liberate bound electrons so they become quasi-free. These electrons then absorb photons during collisions with heavy charged particles in the tissue; after several of these ‘inverse-bremsstrahlung’ absorption events, the electron will have enough energy for impact ionisation, which in turn frees more electrons. If the number of electrons generated through these processes, outweighs the loss of electrons that diffuse out of the focal volume or recombine with molecules, an avalanche in the number of free electrons occurs. This is where the short pulses are key as the energy is confined in a small volume of tissue. If the free electron density in a focal volume reaches critical values, 10^{18}-10^{20} cm^{-1}, a plasma is formed. The material is then explosively ejected.

2.5.2 Laser Poration of the Skin

The majority of the work in which a laser has been used to overcome a biological barrier has been performed on skin. An excimer laser with 193 nm wavelength and 14 ns pulse duration was used to remove layers from the stratum corneum and then the permeability of tritiated (^3H_2O) water was measured. The greatest enhancement (124-fold) was seen for a radiant exposure of 70 mJ/cm^2, an unexpected decrease in permeability occurred when the fluence was increased to 170-480 mJ/cm^2 per pulse, with only a 45-fold enhancement achieved. This was likely the result of thermal damage causing the tissue surrounding the pore to coagulate and preventing the transfer of water [71] . Guinea pig skin was ablated and then studied histologically, the thermal damage caused by microsecond pulses was compared directly with nanosecond pulses. A 5-10 fold reduction in visible thermal damage was measured when the nanosecond pulses were utilised [72]. Ablation of the skin by IR, visible and UV sources was compared and the permeation of 5-fluorouracil measured. A significant increase was obtained with all wavelengths, but visible light caused the least damage to the surrounding tissue [73]. A fibre-guided femtosecond laser beam used in combination with an ink facilitated poration of skin, with average powers as low as 0.06 W achieving removal of tissue [74].

2.5.3 Laser Poration of the Nail

With respect to laser poration of the nail the literature is more limited. A proof-of-concept used four different laser systems to create pores, with pulse lengths of 350 fs, 15 ns and two 250 μs systems [75]. The 350 fs system was demonstrated as the most efficient for ablation, left the tissue free of cracks and showed the least visible thermal damage. More recently, poration of the nail was achieved with CO_2 lasers. As expected the high power and long pulse length (3.5 ms) resulted in pores with a large surrounding region of visible damage [76]. In a clinical study, 92% of patients showed a positive response to the application of a topical cream on nails porated with a millisecond pulsed CO_2 laser [77]. Exposure to laser ablation was not without noticeable pain, probably resulting from heating caused by the long pulse duration.

2.6 Raman Spectroscopy

Raman scattering, the phenomenon in which light is inelastically scattered, causing a change in its frequency was first reported in 1928 by the Indian physicist Raman earning him the 1930 Nobel Prize [78]. Despite this, it was not until the 1990s that a revolution in technology drove Raman spectroscopy forward as a method to investigate materials. Nowadays, scientists from a broad range of disciplines can straightforwardly perform complicated experiments, analysing a broad variety of samples, providing a deep understanding of the chemical structure.

Raman can be thought of as a complementary technique to the better established Infrared spectroscopy (IRS). The two differ in mechanism: IRS is based on the absorption and emission of infrared light that is in resonance with the energy level transition of the material being investigated; Raman is an inelastic scattering process. Although the spectra generally present similar information, there are some frequencies permitted in Raman that are forbidden in IRS and *vice versa.* In addition, there are several practical advantages for using Raman microscopy. Firstly, the spatial resolution of Raman microscopy is far higher than IRS, with most modern systems easily achieving 1µm. Secondly, Raman can be carried out *in situ* or *in vivo*; on samples in gaseous, liquid, solid, crystal or film state; and on very small quantities of material. Thirdly, unlike IRS, Raman does not require any contact with the sample and providing the power of the device is monitored the technique is non-destructive.

The technology involved in Raman spectroscopy has advanced rapidly in the previous 20 years. The main components of a Raman microscope include a monochromatic light source, generally a laser, a spectrometer, detectors and the optical setup. The coupling of the spectrometer with a standard optical microscope and a spatial filter is the reason for the high spatial resolutions that are achieved. If the setup includes a confocal microscope the interior of samples can also be investigated. An important aspect to be considered is the choice of laser, this is often determined by the sample being investigated, with the avoidance of fluorescence that obstructs detail in the spectra the primary concern. Numerous setups use Charge Coupled Devices (CCD) for detection, their high sensitivity to light is advantageous when dealing with weak Raman signal intensities.

2.6.1 Raman Scattering

Understanding of the processes that happen during a scattering event, leading to the generation of Raman scattered radiation is better understood using quantum theory. According to quantum mechanics, electromagnetic radiation such as light is comprised of photons, elementary particles with an energy proportional to their frequency; $E = hf$ where h is Planck's constant. If a photon impacts a molecule, is absorbed and subsequently re-emitted, it can be scattered either elastically with the same energy as before (Rayleigh scattering) or inelastically, losing or gaining energy (Stokes and anti-Stokes scattering, respectively). Figure 2.5 displays both of these processes. In a) the molecule is in state m, and upon incidence of the photon jumps to a state, r, before emitting a photon and settling back to a higher energy level n; the scattered photon's frequency is reduced from the incident by $h\nu_{mn}$, this is Stokes scattering. Conversely, anti-Stokes scattering occurs if the molecule is in a higher state n and finishes in m as shown in b). The result is an increase in the photon's frequency $h\nu_{mn}$. The change in frequency ν_{mn} is the Raman shift and corresponds with the vibrational or rotational transitions of the scattering molecule. Detectors measure the intensity of scattered radiation, and a plot can then be generated for the intensity as a function of the Raman shift. Several things to note: the molecule never actually moves to the state, r, it is purely virtual; as no transition occurs v_0 need not match any absorption frequency of the scattering molecule; the absorption and emission are actually two simultaneous processes.

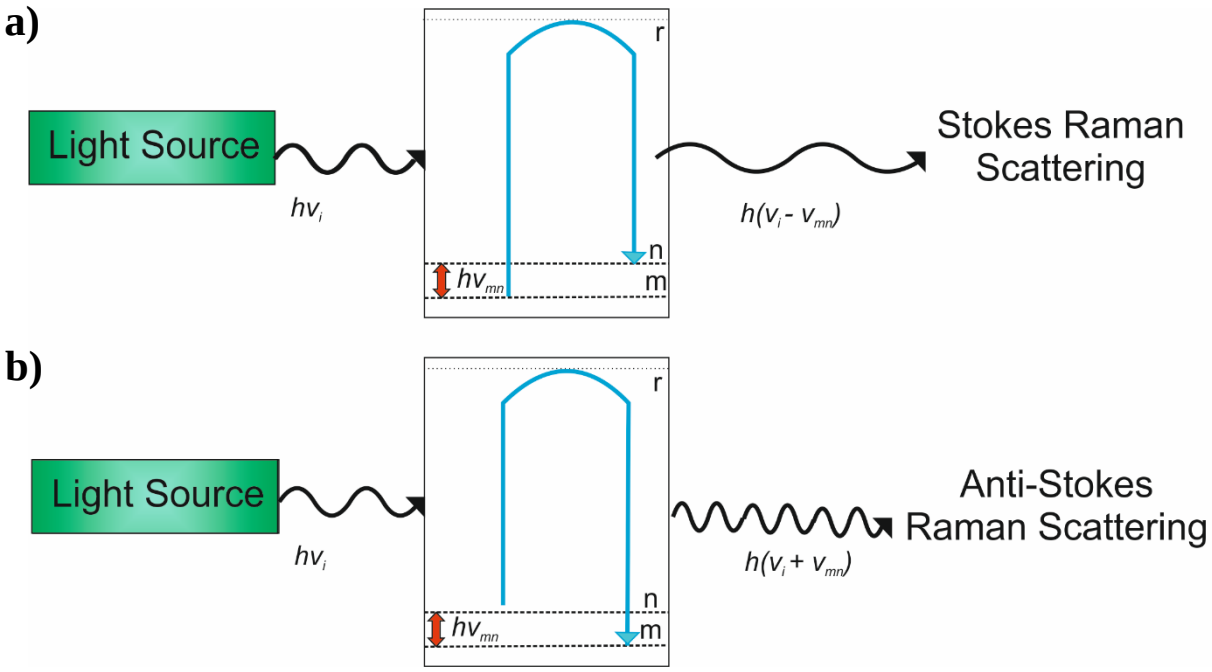

Figure 2.5: Mechanism of Raman scattering. Stokes scattering is shown in a) with the molecule moving upto a higher energy state and the photon emitted photon having a lower energy. Anti-Stokes scattering is shown in b) with the scattering event causing the molecule to fall to a lower energy state and the emitted photon being greater in energy than the incident.

The intensity for a particular Raman transition can be established mathematically from the induced electric moment matrix element P_{mn}, for a transition between state m to n, we write[79]:

$$P_{mn} = \int \varphi_m P \varphi_n \, d\tau \tag{2.1}$$

where φ_m& φ_n are the time independent wave functions of the states. The quantum-mechanical result is of the form:

$$P_{mn} = \frac{1}{h} \sum_r \left(\frac{M_{mr} M_{rn}}{\nu_{rm} - \nu_0} + \frac{M_{mr} M_{rn}}{\nu_{rm} - \nu_0} \right) E \tag{2.2}$$

where ν_{rn} & ν_{rm} are the frequencies that correspond to the difference between the states defined in the subscript, M_{mr}& M_{rn} are the corresponding transition moments and E is the electric field.

The square of P_{mn} determines the intensity of Raman scattering occurring for the transition m →n, in addition to the biquadratic of the frequency of scattered light, the "ν^4 rule", and the intensity of incident light:

$$I_{mn} = \frac{128\pi^5}{9c^4}(\nu_i \pm \nu_{mn})^4 I_i P_{mn}^2 \quad (2.3)$$

Generally, detectors record Stokes scattering as it is the more common process. The underlying reason for this imbalance results from the distribution of energy states molecules are in. At room temperature the majority of molecules will be in their ground state and when inelastic scattering processes occur, it is more likely that the transitions will be for a molecule moving to a higher energy state. The result is a higher intensity of Stokes scattered photons than anti-Stokes.

2.6.2 Raman Spectroscopic Study of the Human Nail

The non-destructive nature of Raman spectroscopy makes it a useful tool for the investigation of biological tissue. Keratinaceous tissues are stable at room temperature and so are especially simple to study with Raman spectroscopy. Initially, spectral bands were assigned to the chemical bond in proteins and lipids in the stratum corneum [80]. Following on, the structural state of proteins, water and lipid in the skin, hair and nail spectra was studied [81]. Raman was then used for an in-depth study of keratinaceous materials from across the animal kingdom: hoof, horn, tortoiseshell and nail. The protein secondary structure was identified in an α-helical conformation for mammalian keratins, whilst the β-sheet conformation was seen in the reptilian tortoiseshell [82].

With technological advances, modern detection equipment has seen some innovative uses of Raman spectroscopy on the nail. One group found they could differentiate the spectra between fingernails and toenails to an accuracy of 95%, using Raman spectroscopy and a multivariate classification technique [83]. This technique was enhanced and subsequently used to identify the gender of the nail clipping donor, this type of investigation is of particular interest for application to forensic science [84].

Raman spectroscopy has the possibility to help diagnose diseased tissue. During onychomycosis, fungal erosion leads to changes in the secondary structure of proteins and spectra revealed a significant decrease in the content of the sulphur-containing amino

acids in diseased nails [85]. The specific causative organisms in nail samples infected by onychomycosis were determined using Raman Spectra [86]. If these techniques could be exploited in a clinical setting, a quicker diagnosis and appropriate treatment for onychomycosis would be possible. Monitoring of the nail during treatment would ensure the new nail is disease free.

Currently, there are no suitable techniques to quantify the damage caused to biological tissue by laser poration. Raman spectroscopy offers a solution to this problem, and can be exploited to increase the efficiency of laser poration. In the case of biological materials, Raman spectra generally show a broad featureless background signal, across the entire spectral range of standard spectrometers (400 - 4000 cm^{-1}). This signal is usually attributed to fluorescence [87-89], although the morphology of the sample has also been shown as a contributing factor [90,91]. An increase in intensity of the signal was found in skin samples heated above 100 °C, this likely resulted from the denaturation of cellular proteins and collagen.

2.7 Atomic Force Microscopy

2.7.1 AFM Background

Atomic Force Microscopy (AFM) is an imaging technique that comes from the Scanning Probe Microscopy (SPM) family. Binnig created the first SPM device, the Scanning Tunnelling Microscope, in 1982 and from this device the principles for the AFM came about [92], with the technology developed and the first study published in 1986 [93]. The two basic components of the AFM are a probe, generally an ultra-sharp tip at the end of a silicon nitride cantilever, and a detection system. Cantilever movement is controlled through the use of a piezoelectric actuator: a ceramic device which converts electrical energy directly into linear motion, with virtually unlimited resolution. The tip's movement is detected using a laser; the beam is reflected from the top of the cantilever onto a photodetector. Modern detectors are capable of measuring minute changes in the cantilever's positon. When a scan is performed the tip rasters across a two-dimensional matrix, with the feedback signal recording a height measurement at each pixel. These data allow the generation of pseudo-three-dimensional images of the sample. AFM has

multiple imaging modes: the first, contact mode, involves the tip being kept in constant contact with the surface of the sample whilst the applied force and cantilever height are kept constant through a feedback system. The height at each point is measured from the movement required by the piezo actuator to keep the frequency and height of the cantilever constant. Unfortunately, contact mode suffers from large lateral forces exerted by the tip on the sample, which results in damage to either the tip, sample or both. A solution to this problem was found in tapping mode, the cantilever is driven to oscillate and only briefly comes into physical contact with the sample. When the tip is brought closer to the sample the amplitude and frequency of oscillation changes; the feedback circuit adjusts the system to return to the original amplitude and frequency. The forces that cause this are recorded by the detection system and are converted into the heights at these points.

2.7.2 AFM on Biological Materials

AFM is a versatile tool that can be used to investigate biological materials. Samples need little preparation for AFM thus avoiding the introduction of artefacts. Exploration can be performed in liquids and so live cells can be viewed at resolutions unachievable with optical or confocal microscopy. The biological material that has been most extensively studied with AFM is DNA, which was first investigated in 1992 [94]. In addition, imaging has been performed on other biological materials such as single proteins [95,96] and various types of cells including red blood cells, epithelial cells, glial cells and skin cells [97-100]. The single study using the AFM on the human nail was performed in 2002 [51]: samples were exposed to the chemical penetration enhancers' dimethyl sulfoxide and urea, as well as being covered in two acids; tartaric and phosphoric. After exposure, 10 x 10 μm^2 scans were taken and the roughness on the dorsal surface measured. Unsurprisingly, the acids caused a large increase in the roughness of surfaces.

Chapter 3

Methodology

This chapter details all methodology employed within the thesis, including preparation of the nail samples for various experiments, the microscopy techniques employed to study the nail plate, the laser setup used for poration and the caffeine permeation experiments used to investigate the efficacy of the poration.

3.1 Nail sample preparation

3.1.1 Nail Collection

All experiments involving fingernail in this thesis were performed on *ex vivo* nail samples. Nail plates were obtained (using a protocol approved by the University of Bath Research Ethics Approval Committee for Health (EP 15/16 71)) from healthy adult donors, who had given their informed consent. Clippings were taken from the plate that had grown sufficiently past the hyponychium in the same way as nails are removed cosmetically. Volunteers were asked to avoid using any type of varnish or decorative objects during the 2-3 months they were required to grow the nail plate to the minimum requested length of 8 mm. This reduced the chance of chemical or physical alteration of the nail plate. Individual samples were stored in a zip-lock bag, with all samples from the same volunteer being stored in a larger zip-lock-bag. The bag was then stored in a freezer at -20 ^{o}C until use.

3.1.2 Nail Preparation for Poration

Upon removal from the freezer, nails were submerged in deionised water for 30 minutes to rehydrate and restore flexibility. As has been shown previously the staining of tissue aids laser poration [74]. Nails were stained before poration experiments to facilitate ablation. A Lyreco (Telford, UK) permanent marker was used to stain nails for preliminary experiments. Four dyes that absorbed strongly at the wavelength of light generated (λ=532 nm) were used. Ruthenium Red (RR), iodine and Nile Red (NR) were separately made into solutions at a concentration of 1 mg/ml. Both the RR and iodine were made in methanol, whilst the NR was made up in a solution with propylene glycol. The plate was then soaked in a container for 15 minutes, removed and left to dry for a further 5 minutes. The carbon cement (Agar scientific, UK) was applied to the surface using the applicator brush supplied and left to dry.

For the ease of discussing procedures throughout the thesis, a coordinate system for the nail plate is illustrated in Figure 3.1. The x-axis is parallel to the direction of growth, distally from the matrix to the hyponychium. The y-axis is perpendicular to the direction of growth, from lateral nail fold across to lateral nail fold. The z-axis corresponds to the nail thickness, i.e from the dorsal surface to the ventral.

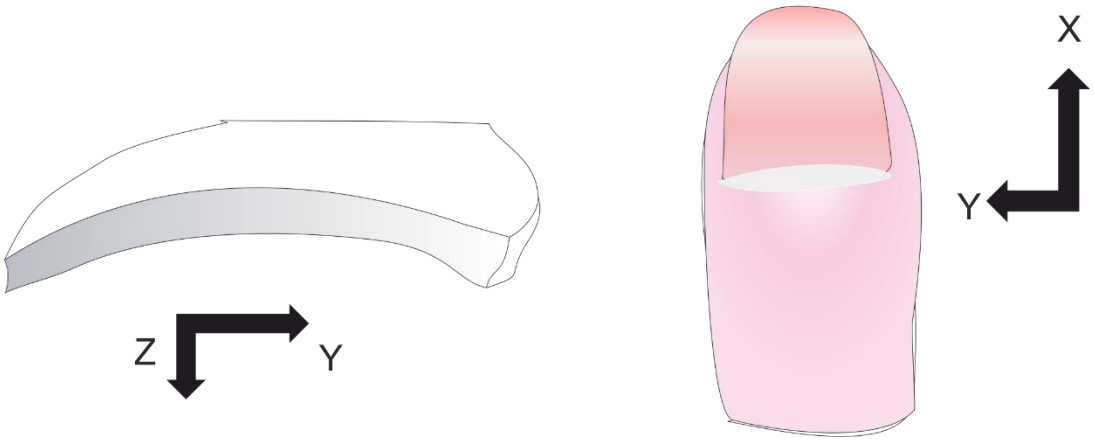

Figure 3.1: Schematic of the nail plate with the xyz coordinates marked.

3.1.3 Heat Treatment of Nail Plates

For the experiments in which the nail was deliberately damaged by heat treatment, nail plates were cut using a razor into pieces roughly 1 mm^2 in the x-y plane. The furnace temperature was set electronically. When a sample was installed the internal temperature dropped rapidly. Subsequently, upon closing of the door the feedback system overcompensated and reached temperatures greater than the set point. The solution to this problem required a surface to be kept at a constant temperature, providing better control over heat treatment of the nail plate. A schematic of the setup used is in Figure 3.2. A brass block was placed inside the furnace, with the internal temperature of the block measured using a k-type thermocouple. A basket was made from a sheet of copper and placed atop the block, two handles allowed the basket to be picked up easily with tongs. A second thermocouple was attached to measure the surface temperature of the sheet and ensured it was maintained throughout the heat treatment period. Nail pieces were placed on top of the sheet and heated for the required period of time before the basket was lifted out and the sample removed. In total, 8 temperatures (50,70,90,120,160,175,190 and 210 ^oC) and 5 contact times (1,2,4,6,8 minutes) were used on nail plates from 3 volunteers.

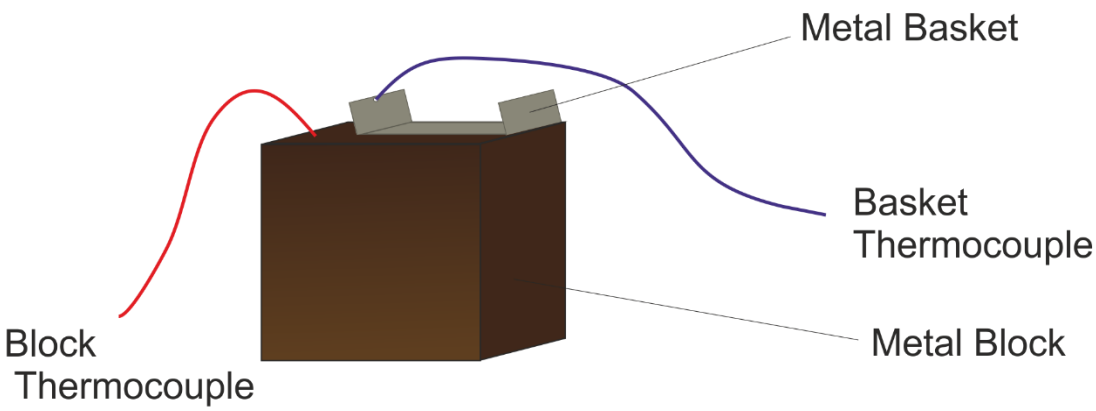

Figure 3.2: Schematic illustration of apparatus used to heat the nail. This block was kept inside the furnace, and the nail placed directly on the basket.

3.1.4 Cross-section Preparation

Two cross-section preparation techniques were performed. In the first, nail samples were embedded in a resin-acetone solution for 4 days. Samples were mounted in a Reichert–Jung Ultracut E microtome (Nussloch, Germany) and sliced into 0.5 µm sections. The slices were collected into a water bath and lifted away with tweezers. They were then placed on glass slides and imaged.

For the second, the nail sample was trimmed and slotted into resin stubs, which had been sawn with a low speed saw (Bueler, Lake Bluff, USA). The nail was then fixed in place with super glue (Loctite, Westlake, Ohio). Subsequently, the stub was placed in the Ultracut E microtome and tissue removed.

3.2 Optical Microscopy

Two optical microscopes were used for imaging. A Leitz HM LUX microscope (Wetzler, Germany) with 10, 20 and 50x magnifications was used for detailed imaging of single pores, or the interior of pores when they had been cross-sectioned. A digital USB microscope (Conrad Electronics SE, Hirschau) was used to capture images of the entire nail plate surface. A calibration grid with a known spacing between the lines was used to determine the number of pixels per µm for microscope images at each magnification. For measurement of pores or other features on samples, FIJI was used [101].

3.3 Scanning Electron Microscopy

Scanning Electron Microscopy (SEM) was used to provide high magnification images of the nail plate. A JEOL JSM-6480 (Peabody, USA) was used to record micrographs of the samples. For imaging, an accelerating voltage of 20 kV was used. Before imaging, all samples were coated with a thin layer of gold with an Edwards's s150b sputter coater to provide the highest reflectivity of electrons.

Several preparation techniques were used for samples to be examined with SEM. The resin stubs, in which cross-sectioned nails were mounted, were placed in a SEM holder with a clamp and sputter coated together. Individual cells from the dorsal and ventral surface were imaged after 'tape stripping': A highly adhesive scotch tape (3M, St Paul,

USA) was applied to the nail surface, the pressure applied and then pulled off from the sample. Any loosely bound cells were ripped off and then the tape was gold coated and viewed using SEM. Samples were treated with a urea solution (Sigma-Aldrich, UK) to disrupt the bonding and make individual cells more visible [51]. Samples were microtomed and then agitated for 30 minutes in 2.5 ml of a 20% urea solution.

3.4 Raman Microspectroscopy

Raman measurements were taken with an inVia microscope (Renishaw, Gloucestershire, UK), which records the Stokes shift. The 5x, 20x and 50x air objectives were used to record the spectra from nail samples. Figure 3.3 shows two spectra obtained when the dorsal nail plate was excited by the different lasers in the Raman setup, the wavelengths of these lasers were 532 and 785 nm. It should be noted that the 532 nm laser is used at a lower power than the 785 nm as it can cause damage to the sample. For better comparison the 785 nm spectra intensity was multiplied by 20. The spectra acquired with the 532 nm laser presents a strong noisy background, with no discernible peaks. In comparison, key peaks are seen in the spectra recorded when the sample was excited at 785 nm, the amide I band in protein is seen at 1660 cm^{-1} and at 1447 cm^{-1} the CH_2 peak is seen.

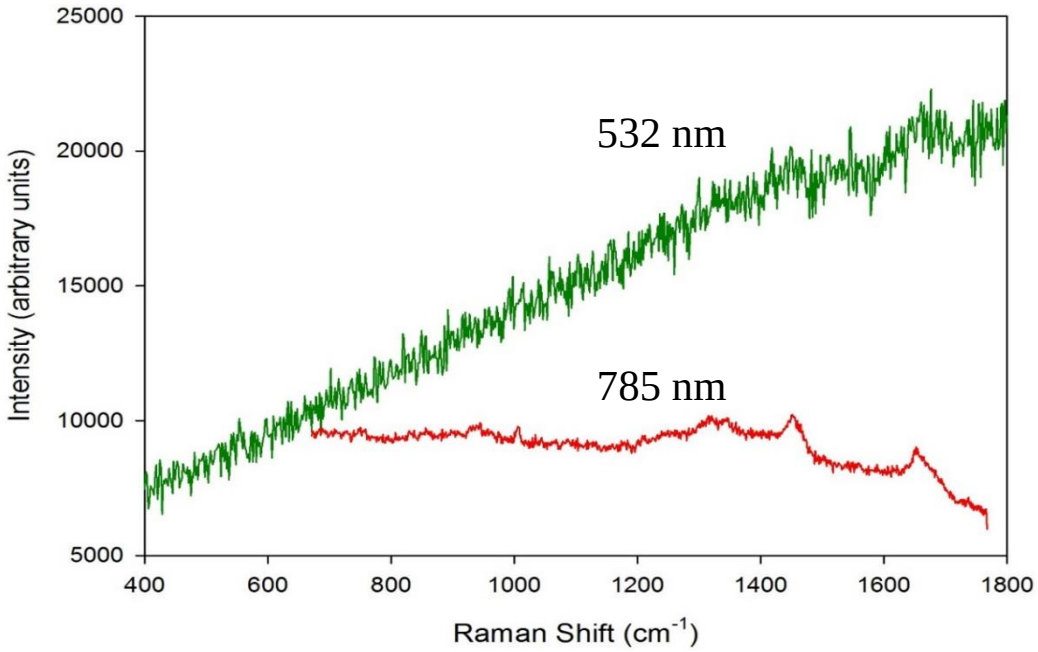

Figure 3.3: Raw Raman spectra taken from the surface of a nail plate, two lasers were independently used for excitation, with wavelengths of 785nm (Red) and 532nm (Green).

For study of the chemical properties of the nail, the 785 nm laser was used to excite samples. After the spectra were obtained post-processing was performed using Renishaw's WIRE software. Artefacts occur in the spectra if the detector is hit by a cosmic ray during acquisition. Fortunately, these manifest as an enormous peak several orders of magnitude larger than the rest of the signal, and so can be removed easily by the function in WIRE. Noise was addressed with a filter that utilised the 2 points before and 2 points after to smooth the curve. The strong background signal was then removed, with an 11^{th} order polynomial providing the highest quality spectra. Finally, spectra were normalised so that comparisons could be made for different regions. The normalising filter integrates the area under the curve and sets it equal to 1.

The 532 nm laser was used to investigate the thermal damage caused to samples during poration with the laser. The Raman response in samples that had undergone heat treatment in the furnace was shown to increase, therefore the signals from these samples were measured and used to generate a calibration curve. For each spectrum 10 one second acquisitions were averaged, three measurements were taken for each sample. A measurement, henceforth referred to as the Characteristic Raman Intensity (CRI), was calculated by integrating the total area under the curve between 700 and 1700 cm^{-1}. The spectra were normalised by the CRI taken from a sample that had undergone no heat treatment for that volunteer. To create a universal calibration curve the log of the normalised CRI was plotted for all three donors against temperature in SigmaPlot (SYSTAT, San Jose, USA). A trial and error approach was taken utilising the inbuilt SigmaPlot dynamic curve wizard, equations of different form were tested, with the software performing many iterations changing the coefficients to fit the curves to the data points.

The temperature profile surrounding pores were calculated using the calibration curve. Profiles were generated either on the surface of the nail plate or on the cross section of a pore. The optical microscope of the Raman could then be used to take either a line scan or a two-dimensional 'map' of the feature of interest, recording spectra at regular intervals. For the maps each pixel has a spectrum taken for it, depending on the size of the map the pixels were either 5x2 or 10x10 μm^2. Subsequently, the CRI value was taken for each pixel and converted to a temperature. The 'colourmap' function in MATLAB (MathWorks, Natick, USA) was used to assign each pixel a colour from a range, and then colourized maps were plotted in two- and three-dimensions.

3.5 Laser Poration

3.5.1 Laser Setup

Two laser systems were used for poration, both were Ytterbium-doped fibre lasers with a wavelength of 1064 nm (Fianium, Southampton, UK). The first laser (laser A) produced an average power of 1 W with a 20 MHz repetition rate. The second laser (laser B) produced 5 W of average power with a 80 MHz repetition rate. Figure 3.4a) shows the entire laser setup: upon exiting the laser the beam passed through a half-wave plate and polarising beam splitter. The beam was converted from a wavelength of 1064 nm, by a frequency doubling crystal (lithium triborate), to a wavelength of 532 nm. To control the sample exposure time, a camera with a mechanical shutter was used; this had fixed exposures of 1, $\frac{1}{2}, \frac{1}{4}, \frac{1}{8}, \frac{1}{15}$ seconds or could be opened continuously when the capture button was depressed. The beam was then guided into a hollow core photonic crystal fibre (HC-PCF) that was designed specifically for guiding 532 nm wavelength light, with a diameter of 16 μm (Figure 3.4b shows a similar fibre with a slightly larger diameter). After these stages, the pulse lengths were 300 and 200 fs respectively. The peak intensity was 0.8 & 3.2 GW/m^2 for lasers A and B at the maximum powers of 0.33 & 1.3 W.

The fibre was mounted on a micrometre stage that could be adjusted in 3 dimensions via screws. The average power was measured as the beam exited the fibre, to change the power the half-wave plate was adjusted. The energy per pore could then be calculated by multiplying the average power by the exposure time. To porate the nail plate, samples were placed on a mount and in front of the fibre tip. Nail samples prepared for the permeation experiments were placed in the adapter and arrays of 100 holes were created inside the diffusion area.

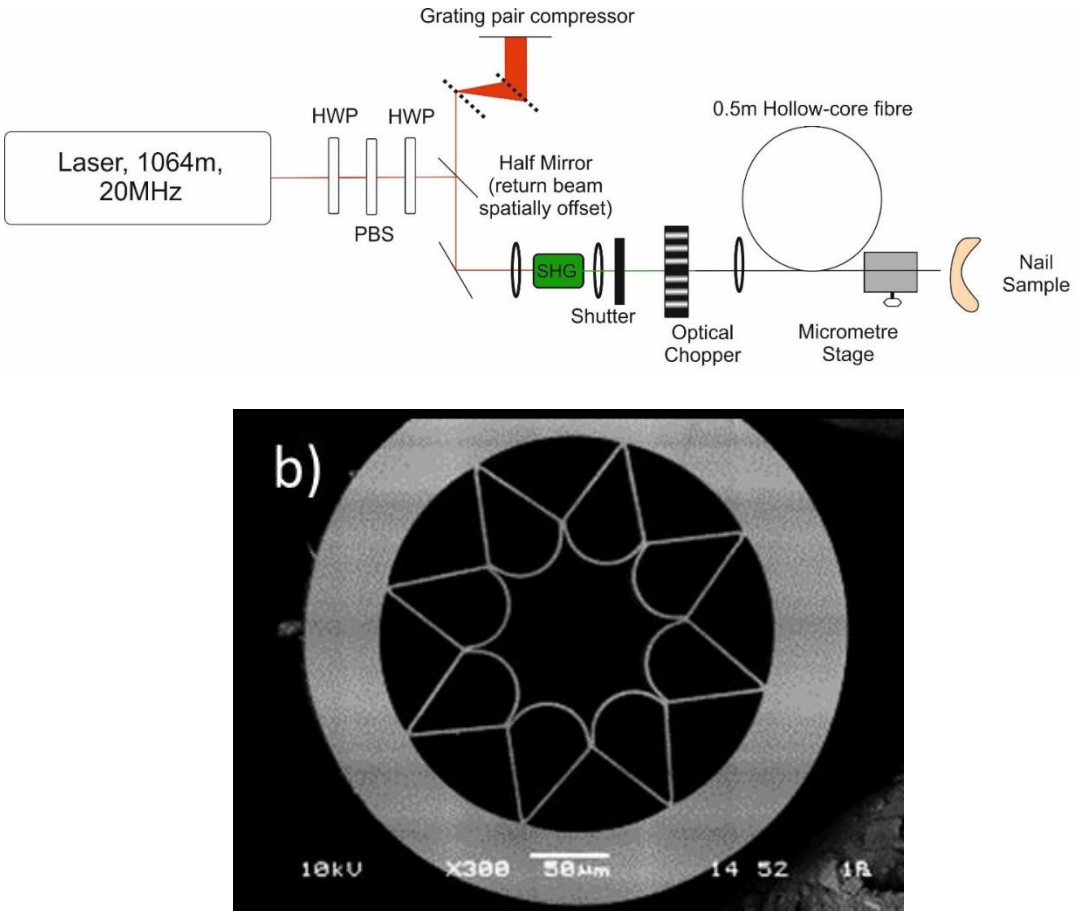

Figure 3.4: a) Schematic layout of the laser setup used. When the optical chopper was added to the system it was placed after the shutter. b) SEM image of a hollow core PCF with the same structure, but larger diameter, than the fibre used to guide the laser radiation [74].

3.5.2 Optical Chopper

For further control of the grouping of pulses, an optical chopper was used. This device consisted of the motor with a windmill-style blade attached to it. As the motor rotates the beam was chopped with windows between the solid spaces allowing the beam to pass through. The first chopper blade used had 1:1 open/closed ratio with 10 openings and 10 closings. Table 3.1 lists the frequencies used, the duration of an ‘open’ window and the number of pulses in this window. A second blade was used that was solid except for a single slot that was cut out equal to 10% of the area.

Table 3.1: Chopper frequencies and window durations.

Frequency (Hz)	20	200	1000
Window length (s)	2.5×10^{-3}	2.5×10^{-4}	5×10^{-5}
No of pulses per window	50 000	5000	1000

3.5.3 Tip Contamination

Keeping the fibre tip clean was important to ensure power remained high throughout experiments. It was noticed that the fibre tip would often become blackened, presumably from the ejection of material from the pore, which would reduce the power output of the fibre. When blackening was observed the fibre tip would be cut with a ceramic tile to remove the section nearest the sample.

3.6 Caffeine Permeation

Experiments were performed to measure caffeine permeation across intact nails or those that had been porated. Samples were rehydrated before experiments to restore flexibility. The samples were mounted in a curved adapter with a 0.2 cm^2 diffusion area (PermeGear Inc., Bethlehem, PA, USA,). Figure 3.5 illustrates the entire setup, the nails were mounted so that the dorsal side faced the donor chamber, and the ventral side faced the receptor chamber. The experiments were run in side by side Franz diffusion cell with a 3.5ml chamber volume. The plastic adapter was lined with 3M (St Paul, USA) foam to maintain a close seal and prevent leakage of caffeine around the edge of the nail. To verify there was no leakage before each experiment, the apparatus was placed on the blue roll and both cells were filled with 3.5 ml of phosphate buffered saline (PBS, pH = 7.4). If leakage occurred on the blue roll, the apparatus was tightened and retested. PBS was used to maintain hydration in the nails whilst all the samples in a run were prepared.

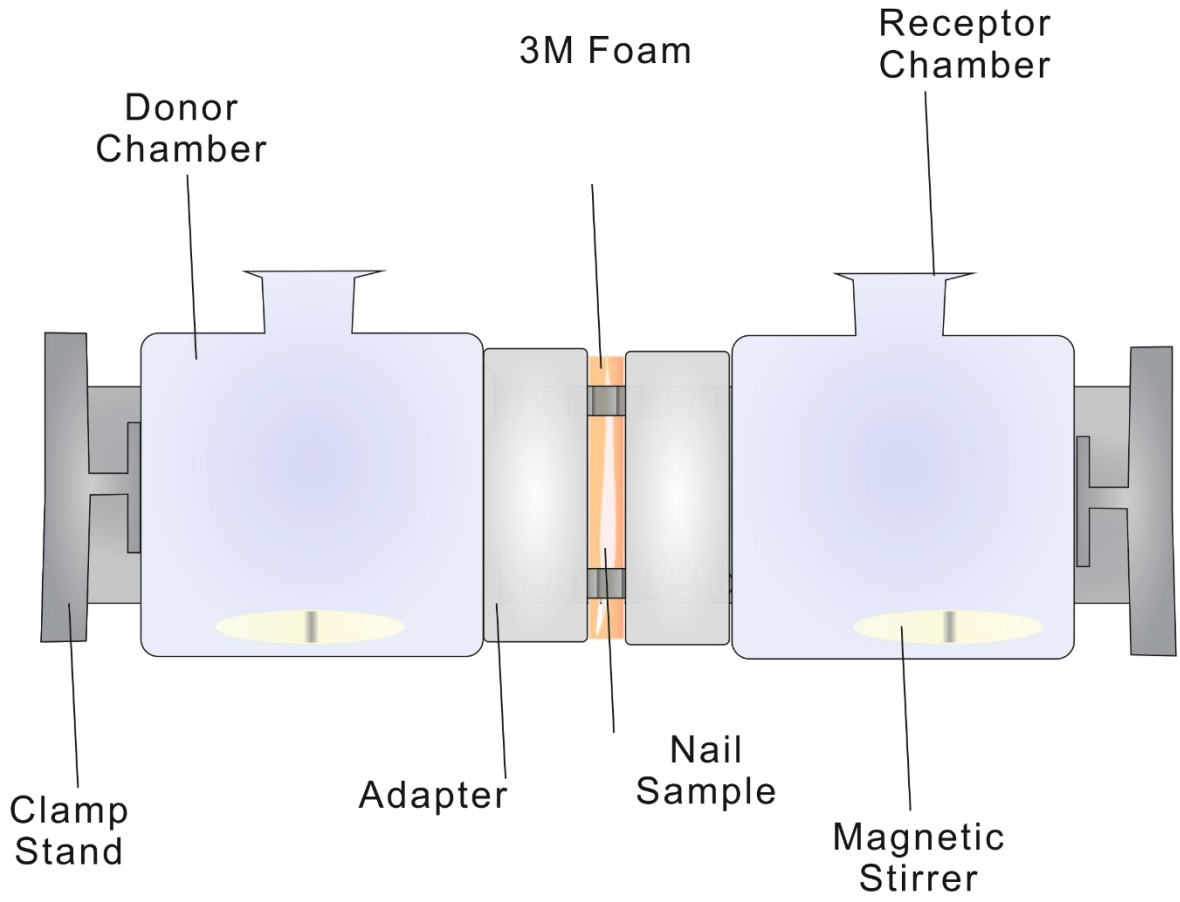

Figure 3.5: Schematic of apparatus used for the permeation experiments

The whole apparatus was kept at 37 ^{o}C in an incubator to mimic physiological conditions. Both chambers were emptied of the PBS and then 3.5 ml of a 20 mg/ml aqueous solution of caffeine was placed in the donor chamber facing the dorsal surface, a fresh 3.5 ml of PBS was placed in the receptor chamber. Both chambers were continuously stirred by magnets. Sampling was performed at 0.25, 0.5, 0.75, 1, 2, 3, 6, 24, 48, 72 hours with 1 ml of receptor solution removed and filtered (0.45 μm nylon filters, Whatman, Maidstone, UK), and then 1 ml of PBS added back into the receptor chamber.

The concentration of caffeine in the receptor solution was measured by high-performance liquid chromatography (HPLC). A calibration curve was created from solutions of known concentration ranging between 1.25-50 μg ml^{-1}. The mobile phase consisted of 20% acetonitrile, 0.1% diethylamine in water and 79.9% deionized water at pH 2.5. A 75 μl injection volume was used, with receptor samples diluted when necessary. The retention time of caffeine was 5.2 min at a flow rate of 1.0 ml min^{-1}. Detection was performed with a UV source at 273 nm.

3.7 Laser Scanning Confocal Microscopy

A 510 Meta inverted Laser Scanning Confocal Microscope (Carl Zeiss, Jena, Germany) was used to measure the geometry of pores in the arrays before permeation experiments. The pore interior auto-fluoresced and so no fluorescent marker was required. Either a 10x or 20x objective was used with consecutive scanning performed by a 405 nm diode laser and a 488 nm argon laser to acquire the two channels used in the images. The confocal images displayed are composites created by merging the two channels: the undamaged tissue of the nail was clearly shown in the channels captured with the 405 nm laser, whilst the damaged region immediately bordering the pore edge fluoresced more strongly under the 488 nm laser. To measure the height of the pores the *z* value at the surface was recorded and the focal plane was moved to the base of the pore, the height was calculated from the difference. Three-dimensional reconstructions of pores were obtained from a series of cross-sectional images acquired at regular intervals and 'stitched together' using FIJI's 3D project software. The contrast and brightness were adjusted to maximise the pore edge and then two-dimension captures were obtained for the images presented in this thesis.

3.8 Atomic Force Microscopy

Atomic Force Microscopy (AFM) was performed using a Veeco Multimode IIIa (Plainview, USA), controlled by Nanoscope software version V6141. Data was recorded in tapping mode with Tap300-G silicon cantilevers (Budget Sensors, Sofia, Bulgaria), the quoted force constant is 40 N/m, with a resonant frequency of 300 KHz. The height map, cantilever amplitude and tapping mode response were all recorded. Images were manipulated using Nanoscope analysis version 1.5. The section tool allowed a line to be drawn across an image and a plot of the height versus position created. Pseudo-three-dimensional images of the sample surface were created and processed by adjusting the light angle, pitch and specular intensity.

Chapter 4

Microscopic Study of the Nail Plate

4.1 Introduction

Before attempting to optically drill the nail it was important to gain an understanding of the physical characteristics of the nail plate. The physical appearance of the nail has been previously investigated with a variety of techniques: optical and electron microscopy have been used to study the structure [102-104]; whilst infrared and Raman spectroscopy allowed study of the chemical properties of the plate [81,82,105]. However, due to the age of these studies they lack the details needed for discussion of experiments performed on porated nails.

This chapter describes the preliminary work performed on the nail using a range of microscopy and spectroscopy techniques. The physical and chemical characteristics were studied, with special attention given to how the plate varies along the direction of laser drilling, the z-axis. Optical microscopy was the first technique used, providing an overview of the plate before more time- and cost-intensive techniques were applied. Images of cells, tape stripped from the plate's surface, provided a reference to their shape and size. However, the depth of focus of the microscope and the poor contrast of the plate made it challenging to study at higher resolutions. These shortcomings were remedied using a Scanning Electron Microscope (SEM), which provides greater magnifications to study the microstructure of the plate. Micrographs were acquired of the plate's surfaces and the differences between the dorsal and ventral sides were studied. Tape stripping cells

from the bulk meant fibrillar structure across the surface and interior of cells was observed. It was observed that the nail is a densely packed solid, often 300 μm or thicker. Identification of individual cells in the plate was challenging, as it was shown they lay in unordered stacks, overlapping and tightly interlocked. The plate's surface and cross sections were studied with Atomic Force Microscopy(AFM). The topographical data recorded was used to construct pseudo-three-dimensional images, which provide detail unavailable from optical or SEM images.

Spectroscopic study of the plate revealed several differences across the z axis of the plate. Changes in the secondary structure of the protein for different layers of the plate was observed with Fourier Transform Infrared Spectroscopy (FTIR). Raman spectroscopy provided complementary information to that given by infrared spectroscopy. It was found that the Raman spectra were superimposed with a very broad featureless background signal. The intensity of this background between 700-1700 cm^{-1}, termed the "Characteristic Raman Intensity" in the group, was measured and a strong variation was discovered. With post processing, this background signal was removed and the spectra were studied. Raman spectra were found to be identical across the nail thickness. Several peaks present in IR were not visible in the Raman spectra and *vice versa*. Variation between spectra in different regions were below the noise tolerance. To investigate if the removal of lipids from the plate varied across the thickness, samples were treated with a solution of chloroform and methanol. Several lipid-dependent peaks were reduced after this treatment.

4.2 Optical Microscopy of the Nail Plate

When the dorsal surface of the nail plate was studied with optical microscopy little detail was observed; the curved nature of the surface meant it was difficult to bring a sizeable region into the focal plane, whilst for the few regions that could be brought into focus it was impossible to demarcate cells. As an alternative, cells were removed from the surface of the plate by application of a strongly adhesive tape. This was performed on the dorsal surface of two nail samples and an example tape is displayed in Figure 4.1. In each panel it is possible to identify individual cells, some of which are marked with white arrows, it can be seen that the cells are irregular polygons with a varied number of sides. In addition,

clusters of cells that are still connected to each other can be observed; black arrows indicate points at which cells overlap. For the larger clusters, it is more challenging to identify individual cells and their boundaries; this may be because more than one layer has been removed.

a)

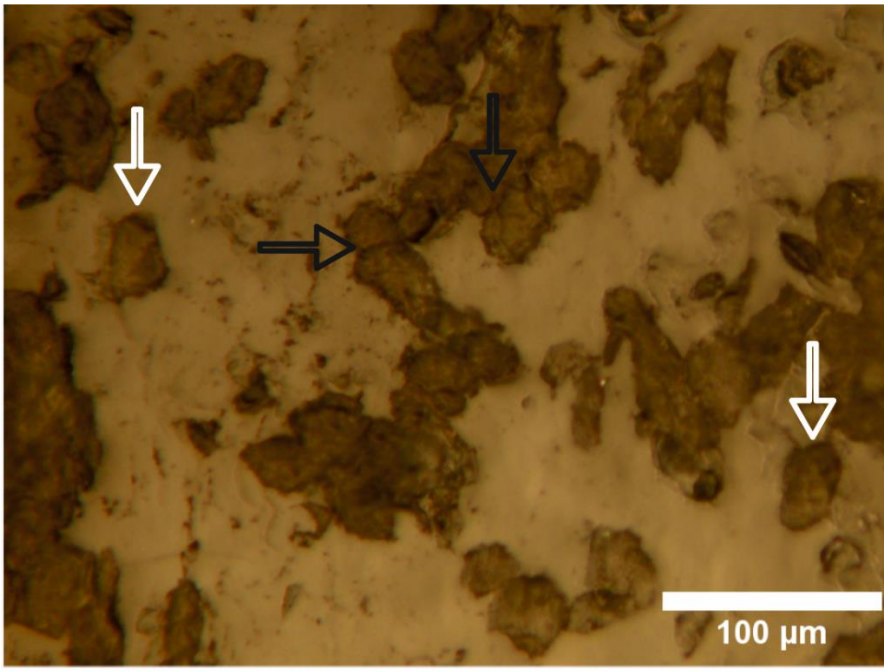

b)

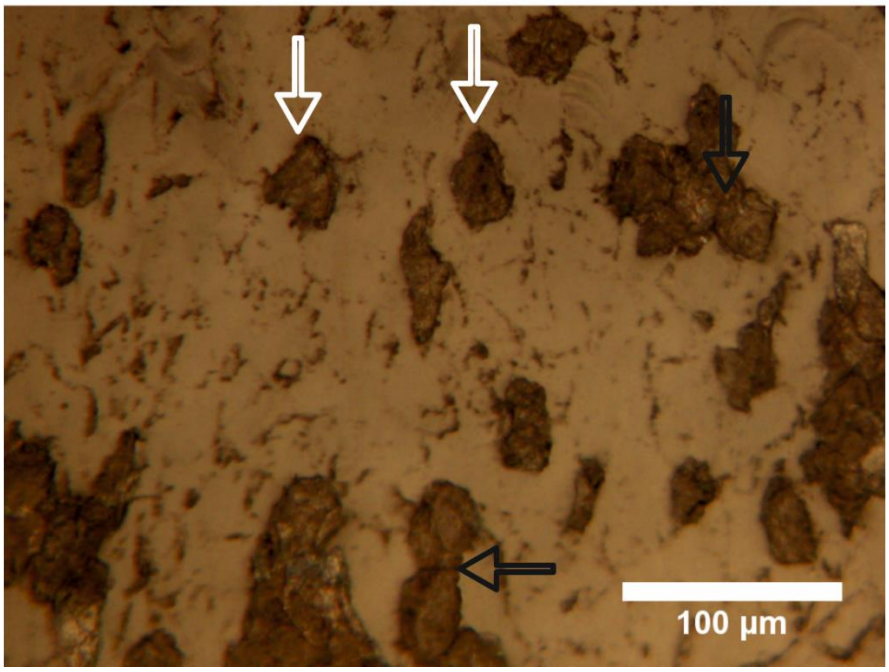

Figure 4.1: Optical images of nail cells removed from the dorsal surface using the tape stripping technique. White arrows indicate individual cells, black arrows indicate edges where two cells overlap.

The next stage involved study of the nail plate's cross-section, both in the XZ plane and YZ plane (see Figure 3.1), in an attempt to identify the cell packing structure. The conventional histological technique that is used to view a cross-section of tissue requires the soft tissue to be embedded in a wax or resin, after which thin sections are cut with a microtome and viewed under a microscope. The embedding process is necessary to preserve tissue in a 'life like' state: preventing it from collapsing due to cell death and also to provide rigidity for cutting. In contrast to viable tissue, an ex vivo nail plate remains virtually unchanged even when left for weeks. This opens up an 'alternative' cross section preparation technique; the nail plate can be cut in the x-z or y-z plane and the bulk sample studied.

During the first stage of preparation for the conventional technique, nail samples were embedded for 4 days. Subsequently, the sample was mounted in a microtome and sliced into 0.5 µm sections. The slices land into a water bath, where the surface tension causes them to lay flat on the surface. They are then lifted away with tweezers and placed on a glass slide. Unfortunately, due to the stiffness of the nail, sections would roll up during transfer from water bath to glass slide obscuring any detail. Figure 4.2 displays an optical image of a section that has rolled up during transfer to the slide.

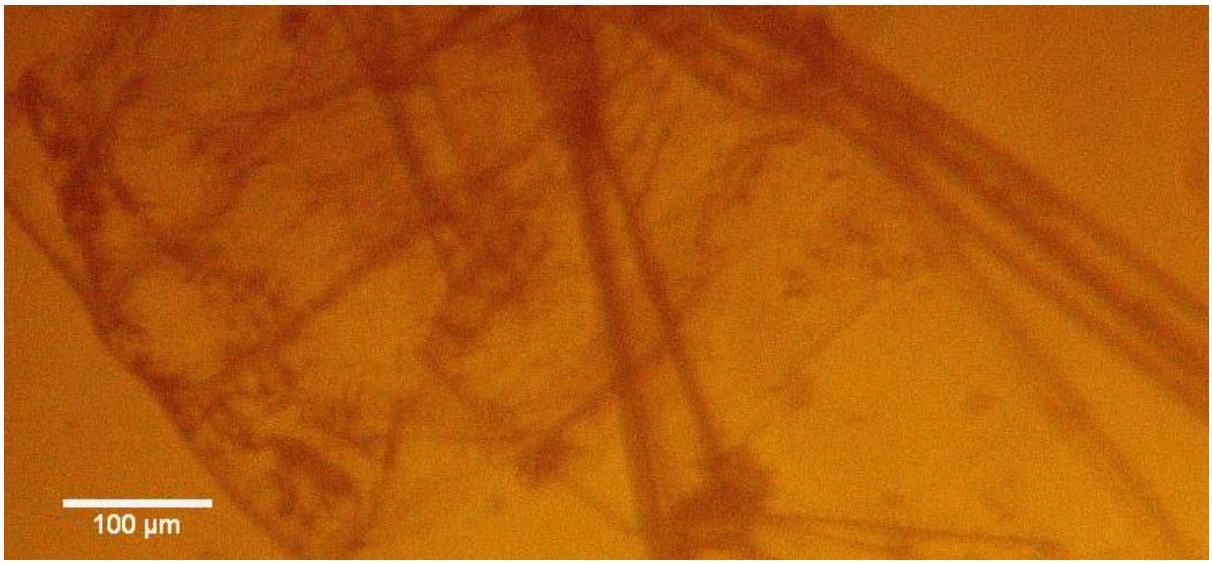

Figure 4.2: Optical image of a section prepared by the conventional technique, that rolled up due to the stiffness of the nail.

To prepare for the alternative technique nail plates were trimmed with a razor and slotted into resin stubs. The rough exposed plane was unsuitable for high-magnification optical imaging and so the nail samples still required microtoming. Unfortunately, the removed sections crumbled apart and could not be collected for viewing.

Despite this preparation, it was difficult to identify individual cells. However, a solution was found by the drastic adjustment of image properties. Figure 4.3 shows a 20x magnification optical image of a cross-section of the y-z plane of a nail plate in which the contrast has been increased, brightness reduced and the colour balance adjusted. For this nail, and throughout the thesis, the dorsal surface is orientated at the top of the image and the ventral at the bottom. Post-processing has revealed a rippling layered structure across the plate. However, at this magnification cell boundaries are difficult to identify due to interdigitation and tight packing. It was found that the two planes of the plate are indistinguishable, with both displaying a layered structure across the z-axis, with the cells lying along the x- or y-axis.

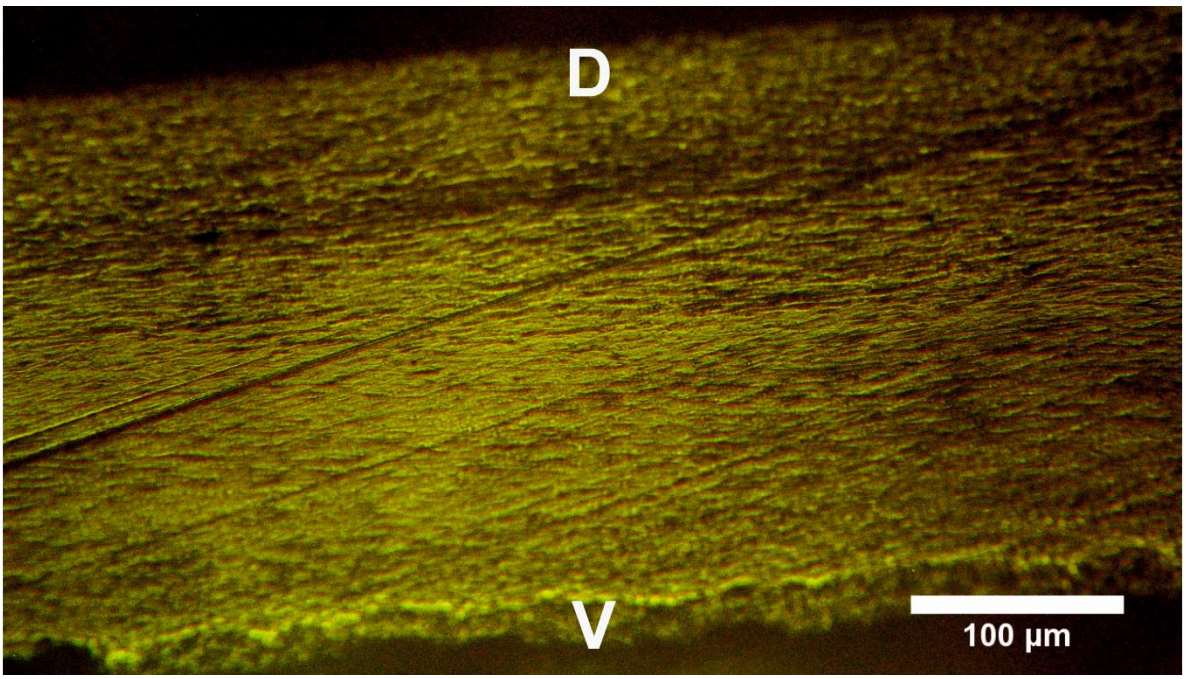

Figure 4.3: Optical image of a cross sectional view through the nail plate (y-z plane). Both contrast and brightness have been drastically altered to better illustrate the layered structure. Dorsal and ventral surfaces marked with D and V respectively. Note the microtome cuts are at approximately 30^{o} to the plate across the sample to prevent confusion with the layered structure.

4.3 Scanning Electron Microscopy of the Nail Plate

Preparation of samples for SEM was identical as for optical, with an added final stage, in which the sample was sputter coated with a 3-5 nm thick layer of gold. This prevented charging of the specimen, meanwhile increasing the signal to noise ratio. The plate surfaces were re-examined; Figure 4.4a) shows a micrograph of the dorsal surface of a plate, b) shows a micrograph of the ventral surface of the plate, both at the same magnification. The macroscopically 'smooth' surface displays a tile-like arrangement, with many of the cells well bound, and few edges showing. However, some cells have been disturbed from the surface and gaps are seen beneath these. This is contrasted by the ventral surface, it is much rougher with more cell edges free. The roughness is in large part due to the previous attachment to the bed, the underlying epidermis contributes to the ventral layer [106] and so some of these loosely bound cells may be epidermal in nature.

From Figure 4.4 it is apparent that the surface of onychocytes is relatively rough. To further investigate this micrographs were taken at a magnification of 10,000x, and are displayed in Figure 4.5. In Figure 4.5a), thin strands, approximately 200 nm in thickness, are observed across the surface of the cells; these are likely fibrils, bundles of keratin filaments. They are generally orientated in a similar direction on each cell, top to bottom in this pane. The fine structure of the ventral surface can be seen in Figure 4.5b) to be slightly different with more rounded features, and little sign of the fibrils.

Figure 4.6 displays cells that were tape stripped and then sputter coated with gold. Onychocytes that were tape stripped from the dorsal surface are displayed in a), there are several cells that overlap each other in this micrograph. As they appeared on the surface, the cells are tightly packed, with minimal edges showing between cells. This helps illustrate the difficulty of drug permeation across the plate, when 100 cells are laid atop each other an extremely tortuous path would have to be taken to cross the barrier intercellular. Of interest is the cell at the top right, which appears to have been ripped open during tape stripping, revealing the interior. The keratin fibrils are observed here as long thin cylinders, nestled together and aligned in the same general direction. Due to the roughness and the concave nature of the ventral surface tape stripping ventral cells was more challenging; far fewer cells were removed on each tape compared with the dorsal

surface. Several ventral stripped cells are seen in Figure 4.6b), the dark ‘shadows’ under cell edges suggest larger gaps than seen for the dorsal cells. Fibrillar structure is observed on some cells.

a)

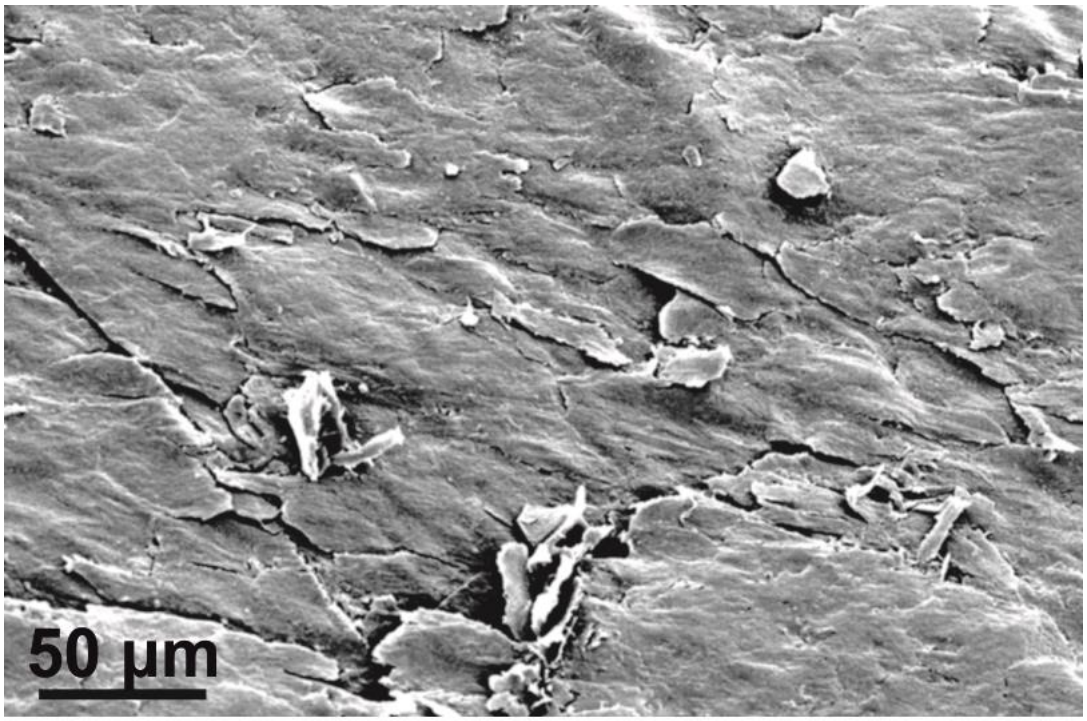

b)

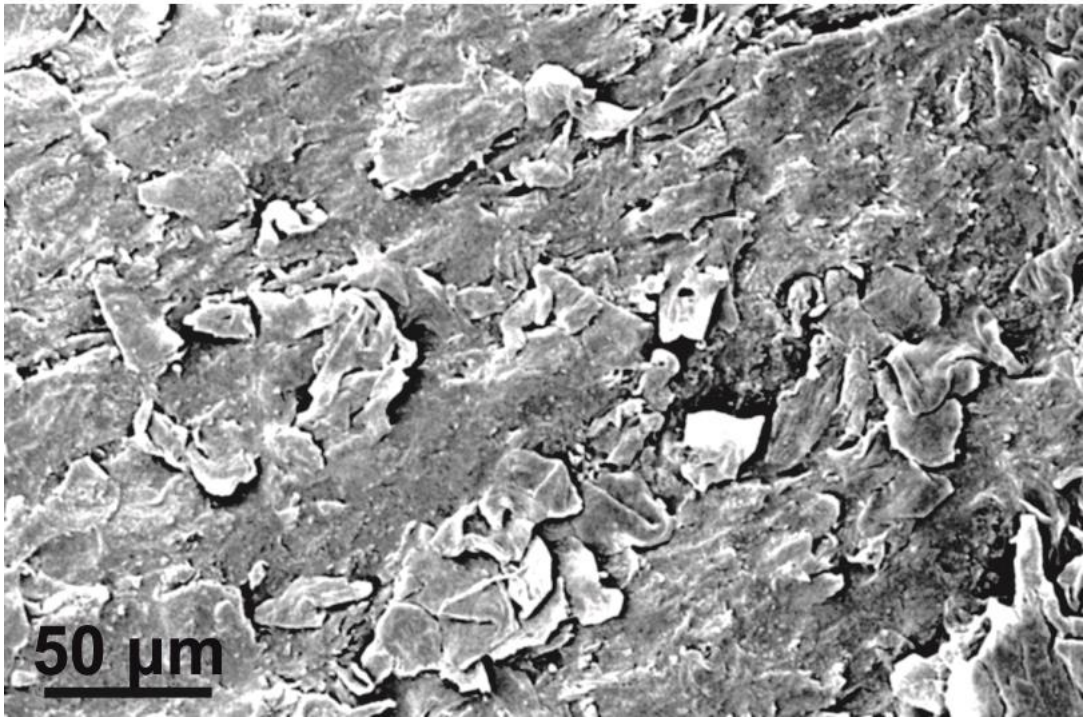

Figure 4.4: Scanning Electron Micrographs of a nail plate: a) Dorsal surface, b) Ventral surface.

a)

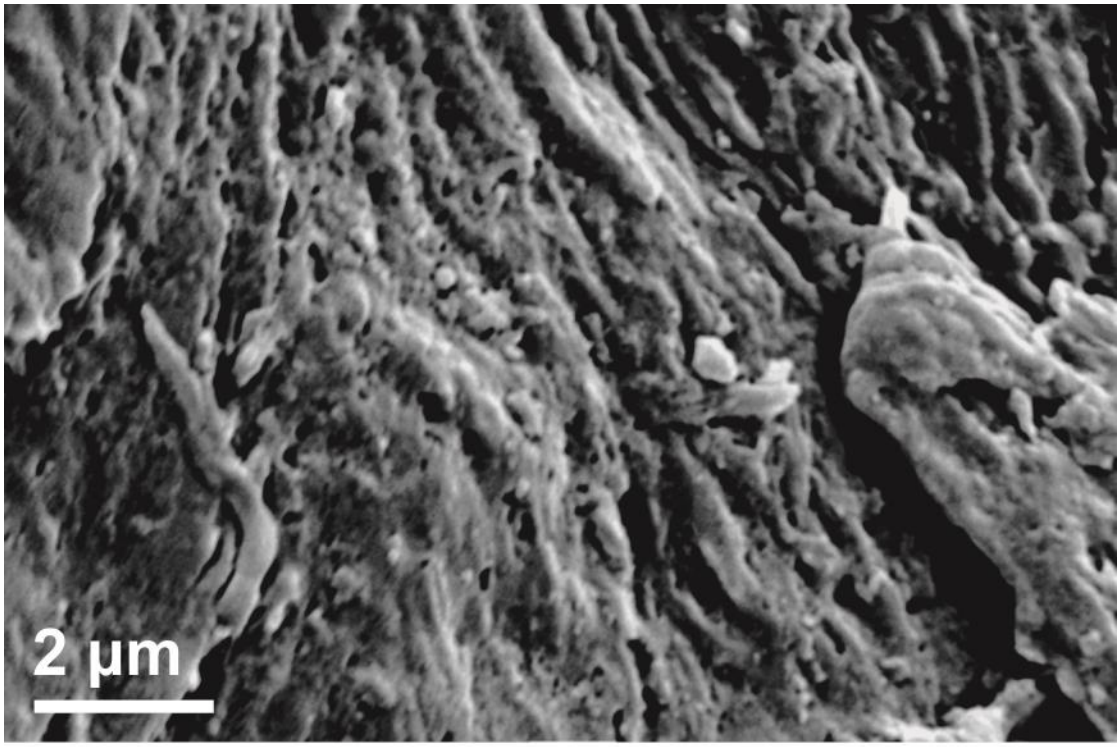

b)

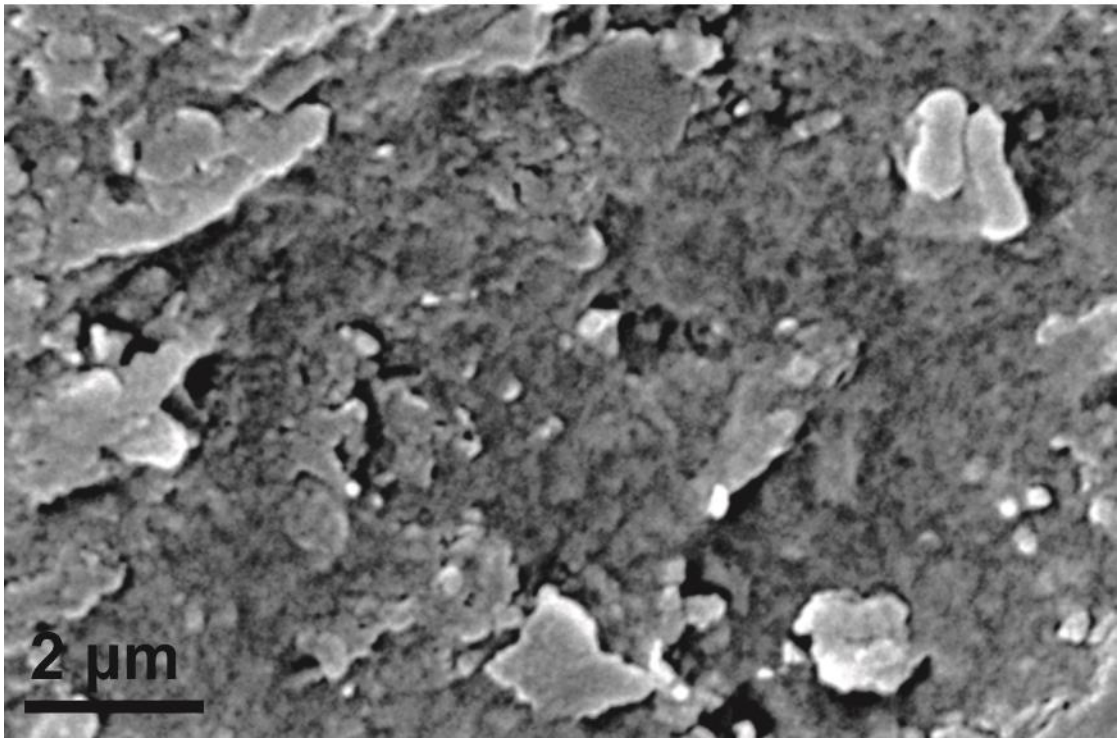

Figure 4.5: Scanning Electron Micrographs of nail plates displaying sub-cellular filamentous structure: a) Dorsal surface, b) Ventral surface.

a)

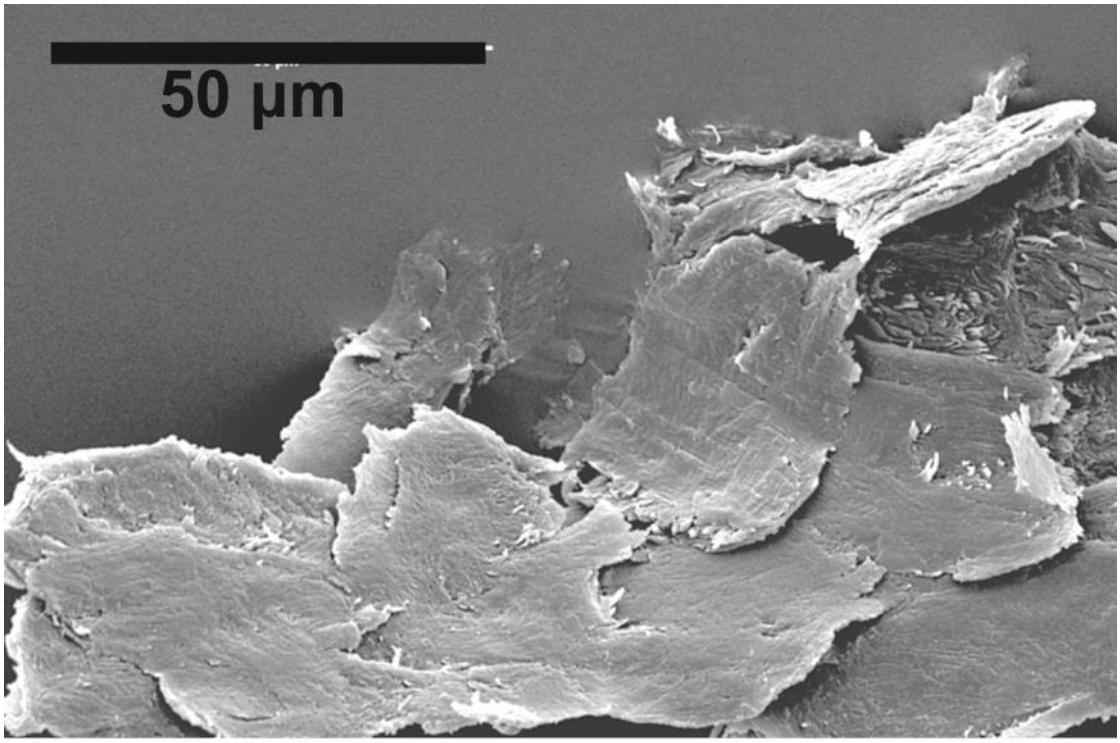

b)

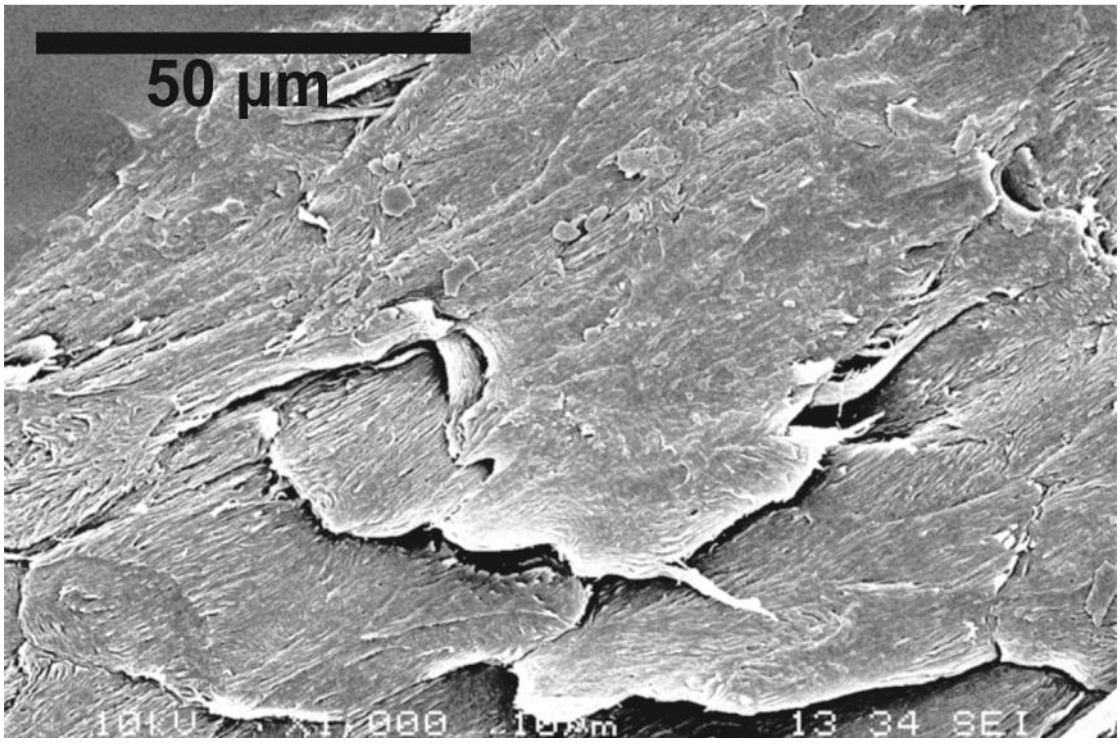

Figure 4.6: Scanning Electron Micrographs of nail plate cells removed from the plate by tape stripping: a) Cells from the dorsal surface, b) Cells from the ventral surface.

Next, cross sections of the plate were investigated; as with the raw optical images it was difficult to observe the layered structure in unedited micrographs. The brightness and contrast were drastically adjusted to aid detection of the layered structure. Figure 4.7a) displays an example in which just the cross-section has been adjusted whilst the rest of the image has been left unaltered, the dorsal and ventral surface are marked D & V respectively. The ripples observed in the optical images are again apparent, but are clearest in a band through the top 60% of the plate, with the layers unobserved in the ventral region. Figure 7b) displays a micrograph (taken at 8000x magnification) from the ventral region, identifying intercellular space is challenging, with a near solid wall present. Small holes, with diameters on the order of 100 nm, can be observed throughout the structure.

To better differentiate the cellular boundaries, nail plates were treated with urea to deliberately separate the cells. Samples were microtomed and then agitated for 30 minutes in 2.5 ml of a 20% Urea solution. Figure 4.8a) displays a micrograph in which the contrast and brightness have been heavily adjusted for the plate. Cellular outlines are clearer across the entire plate, with structure in the ventral region that was unobserved in Figure 4.7. Panel b) shows the border region between the cross section, and then the bottom of the plate curving away out of focus beneath the dashed line. On the cross-section the cell edges are more apparent, with neighbouring cells stacked atop and beneath in an irregular fashion. The cells on the ventral surface have lifted away with larger edges shown between overlapping cells. In panel c) the cell edges are clearly resolved, the distance between the cells is 2-3 μm.

a)

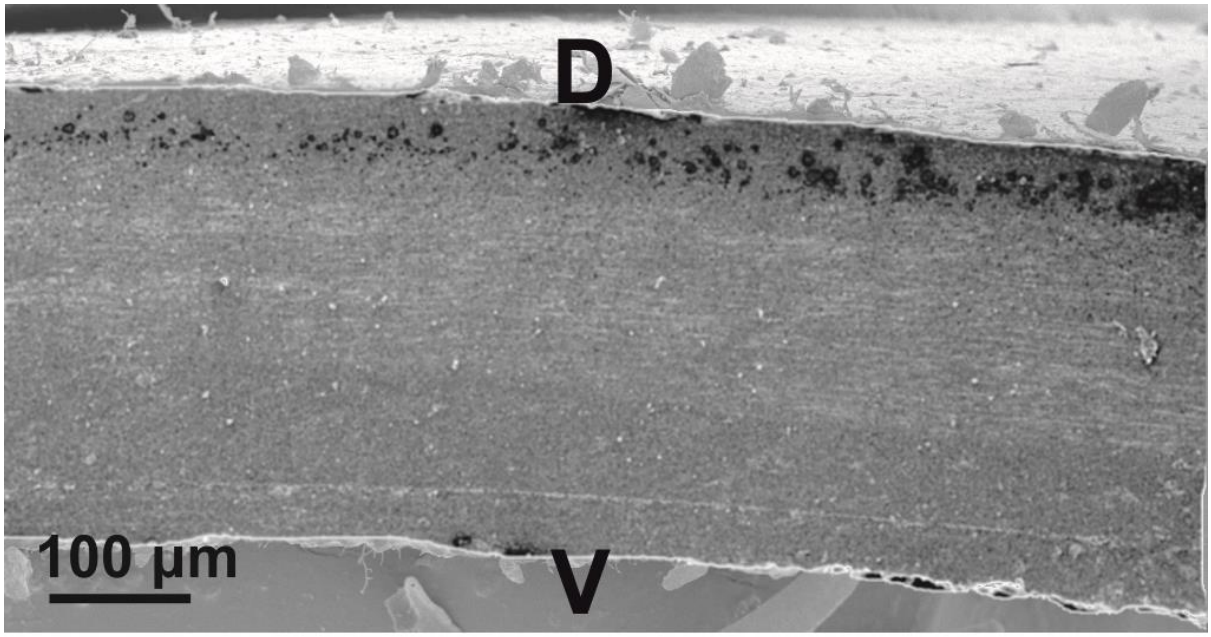

b)

Figure 4.7: Scanning Electron Micrographs of nail plate cross sections; a) the contrast and brightness for the y-z plane of the plate has been drastically altered. The black circles are believed to be an artefact from the sputtering process as they were not observed in any optical images, b) cross section taken from the middle of the plate.

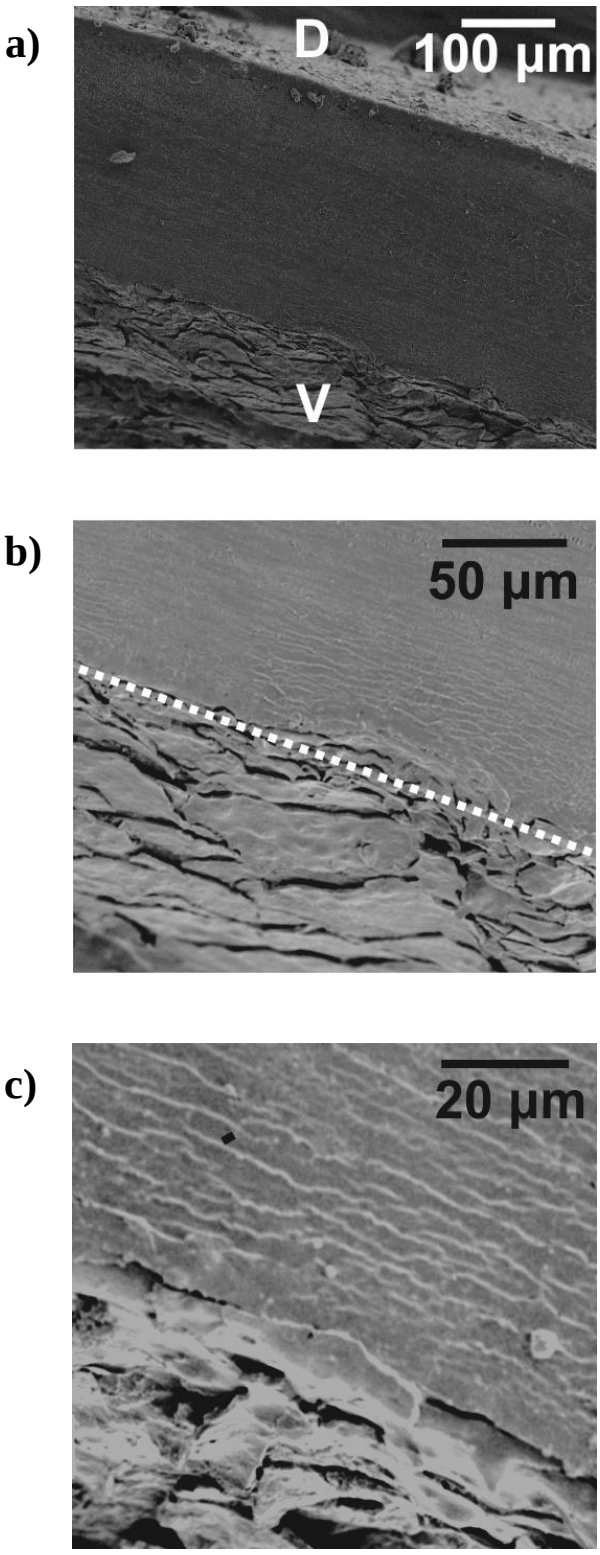

Figure 4.8: Scanning Electron Micrographs of nail plate cross sections treated with urea then gold coated; a) displays entire thickness of plate; b) Displays the ventral edge of the plate, the dashed line marks the 'edge' of the cross section, with the region below the ventral surface curving away; c) Displays the ventral region that has been adjusted to emphasize cell outlines.

4.4 Atomic Force Microscopy of the Nail Plate

Preparation of samples for AFM required more attention due to the small operating space inside the scanner. Care had to be taken that none of the samples protruded into the approach path of the cantilever, which would cause it to crash and potentially be damaged. Nail was cut into approximately 2x2 mm^2 pieces and inspected to ensure that, macroscopically, the variation in height across the surface was minimal.

Figure 4.9 shows topographical data recorded from the dorsal surface of a nail plate. Panel a) is a two-dimensional AFM image of a 60 x 60 μm^2 area, the variations in height are indicated by the colour scale. This area is large enough to contain several cells, but at first, it is difficult to ascertain boundaries. Using the Nanoscope software it is possible to take a line slice across a sample to measure the height variation, this was done along the line marked in a), with panel c) displaying the height versus position data. The steps in height marked by the two arrows, likely displays two cells that are partially overlapping, with one laying in an east-west orientation and the lower cell in a northeast – south-west orientation sat on top of the surface. The fact these cells are higher from the bulk surface is confirmed by the 'shadows' seen in the amplitude micrograph in panel b).

The concave, rough ventral surface is more challenging to scan than the dorsal surface. The 5.5 μm z range of the AFM was exceeded when areas comparable to Figure 4.9a), were scanned on the ventral surface. The roughness meant the tip often falsely engaged with a surface, the protruding flakes causing the AFM to reach its set point without the majority of the surrounding region being in plane. Figure 4.10 displays data taken from the largest ventral area that was imaged, 15 x 15 μm^2, of a nail sample. A two-dimensional AFM image of the region is shown in a), where several cells converge into the dark region marked by the arrow. b) displays the amplitude data for this region, with the rounded structures seen in the SEM easily identifiable. The corresponding line slice for a) is given in panel c), as seen in the SEM images, two cells are aligned with one buried beneath the other.

Figure 4.11 displays pseudo-three-dimensional images of a) the dorsal scan from Figure 4.9 and b) the ventral scan from Figure 4.10. Manipulation of an artificial lighting source in the Nanoscope software makes identifying steps in height easier. Towards the backside

of the surface in a) there are 'blurred' regions, this is an artefact that results from the tip struggling to track a large variation in height over a short distance on the surface.

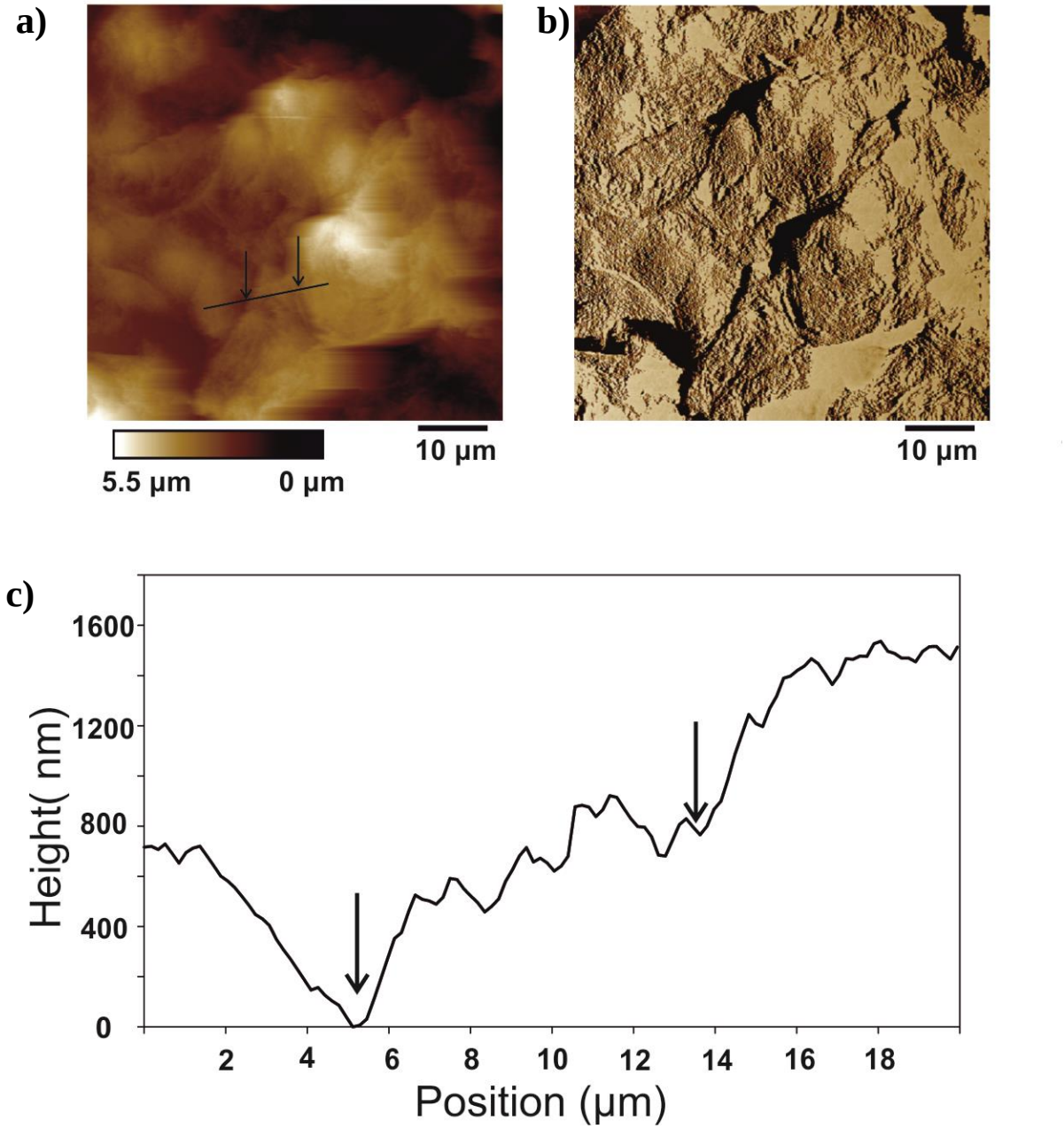

Figure 4.9: a) Two-dimensional AFM image captured taken on the dorsal surface of the nail plate, area = 60 x60 µm^2; b) amplitude data recorded in the same scan as the sample height data; c) plot of height against position along the line marked in a), the arrows mark steps likely resulting from the jumps between cells.

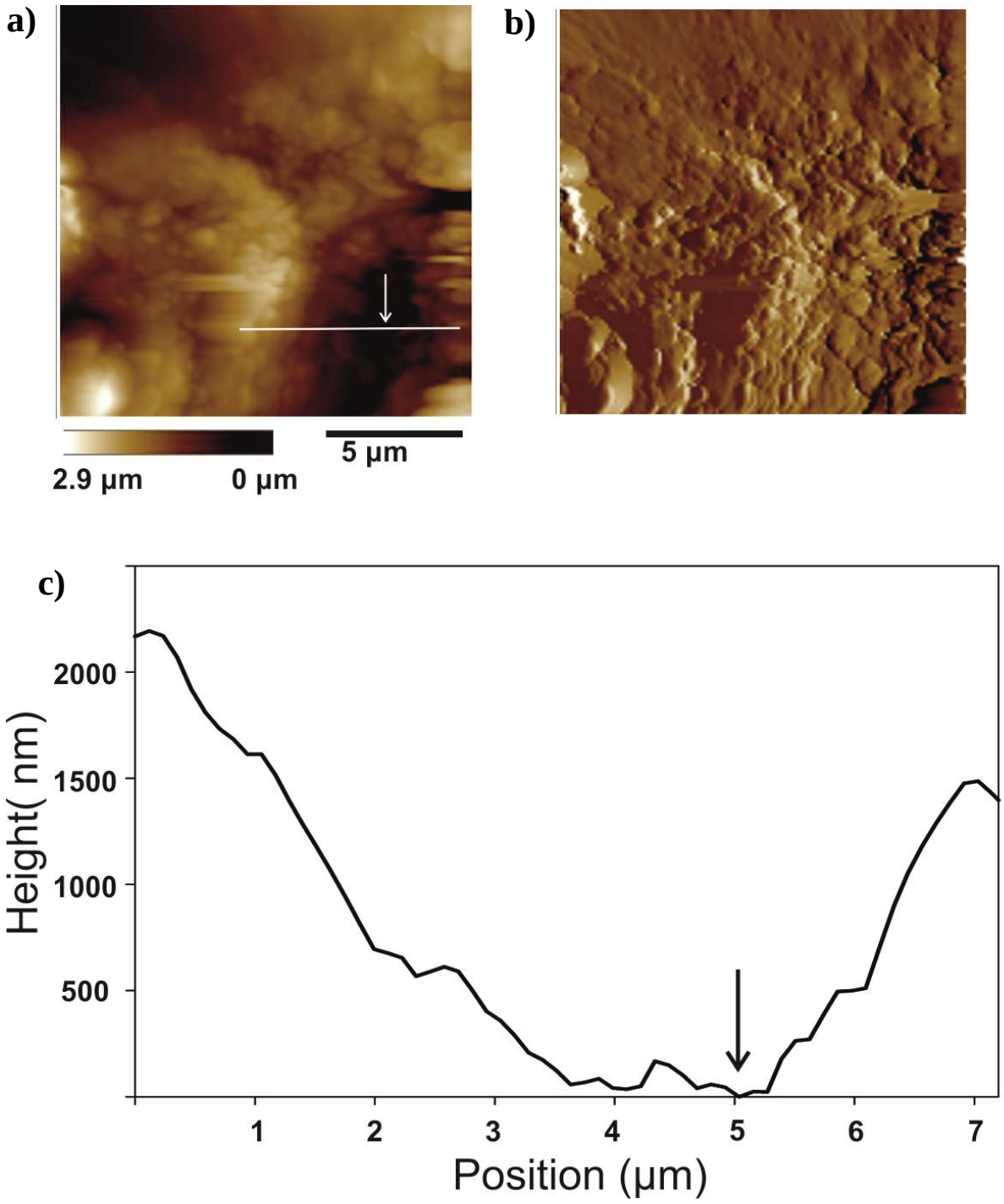

Figure 4.10: a) two-dimensional AFM image captured on the ventral surface of the nail plate, area = 15 x 15 µm^2; b) amplitude data recorded in the same scan as the sample height data; c) plot of height against position along the line marked in a), the arrow marks a point where two cells overlap

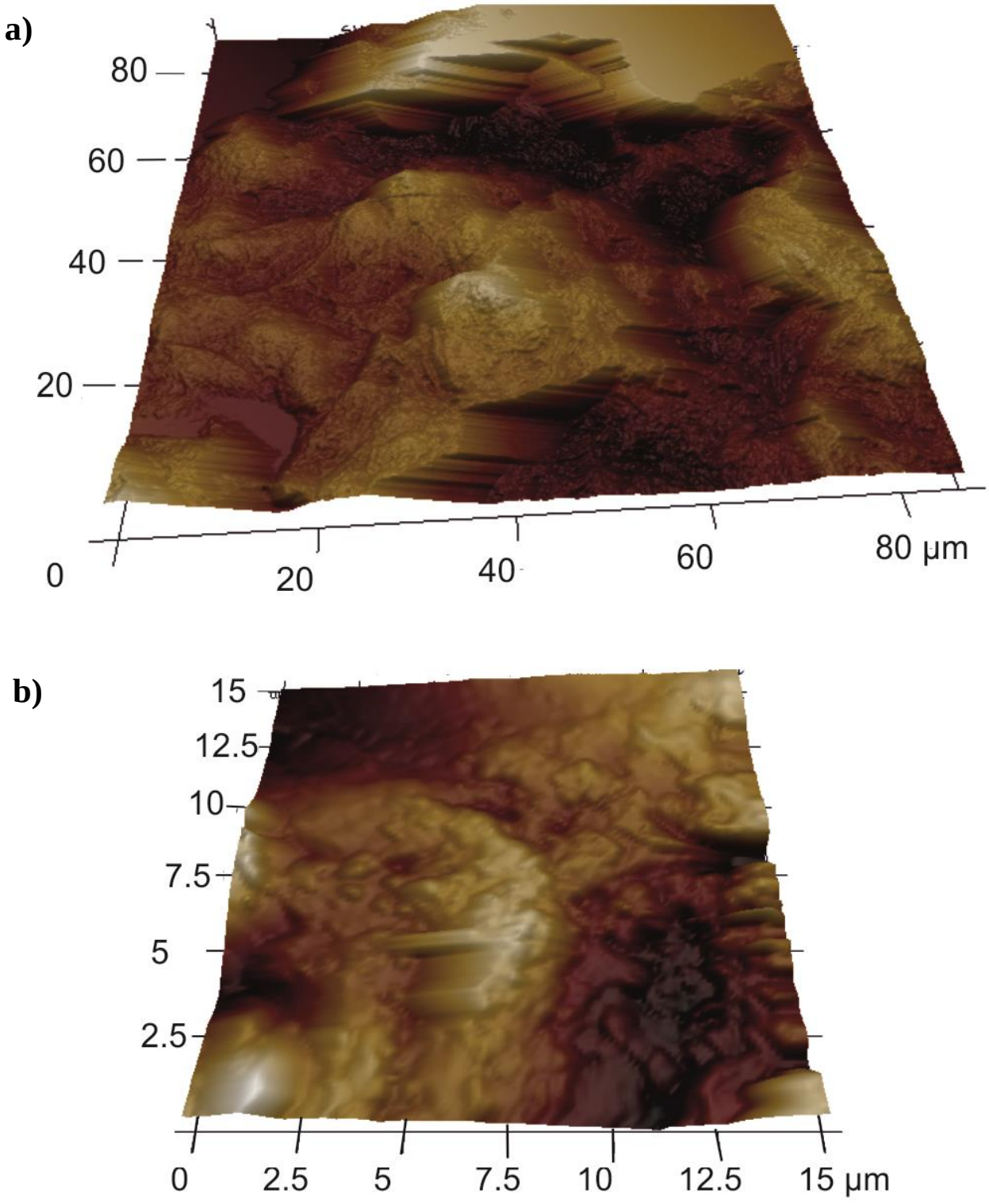

Figure 4.11: Pseudo three-dimensional AFM images a) displays the area from Figure 8a); b) displays the area from Figure 9 a).

Cross-sections were prepared by microtoming and studied. The AFM provides high resolution detail of the height across sections. Figure 4.12a) and the line scan c) are from the intermediate region of a nail plate, from the same depth that the ripples in Figure 4.7a) were observed. Bands pass across the scan from left to right, in the same orientation as the SEM. The largest feature in the line scan is marked between the two arrows, a 2 μm wide protrusion that is can be identified as a cell thickness. The other smaller structures look like fibrils exposed from partially cut cells, similar to those seen in the SEM images.

An image from the ventral region, where limited features were observed in the SEM, of the cross section is given in Figure 4.12b). Compared to the intermediate region, the height variation across this is less, with a 200 nm variation. A slice taken across this sample is given in d), the feature marked by arrows is the thickness expected for the thicker cells in the ventral region, ~5 μm [102]. The interior roughness matches the fibrillar structure seen in the SEM images in Section 4.3.

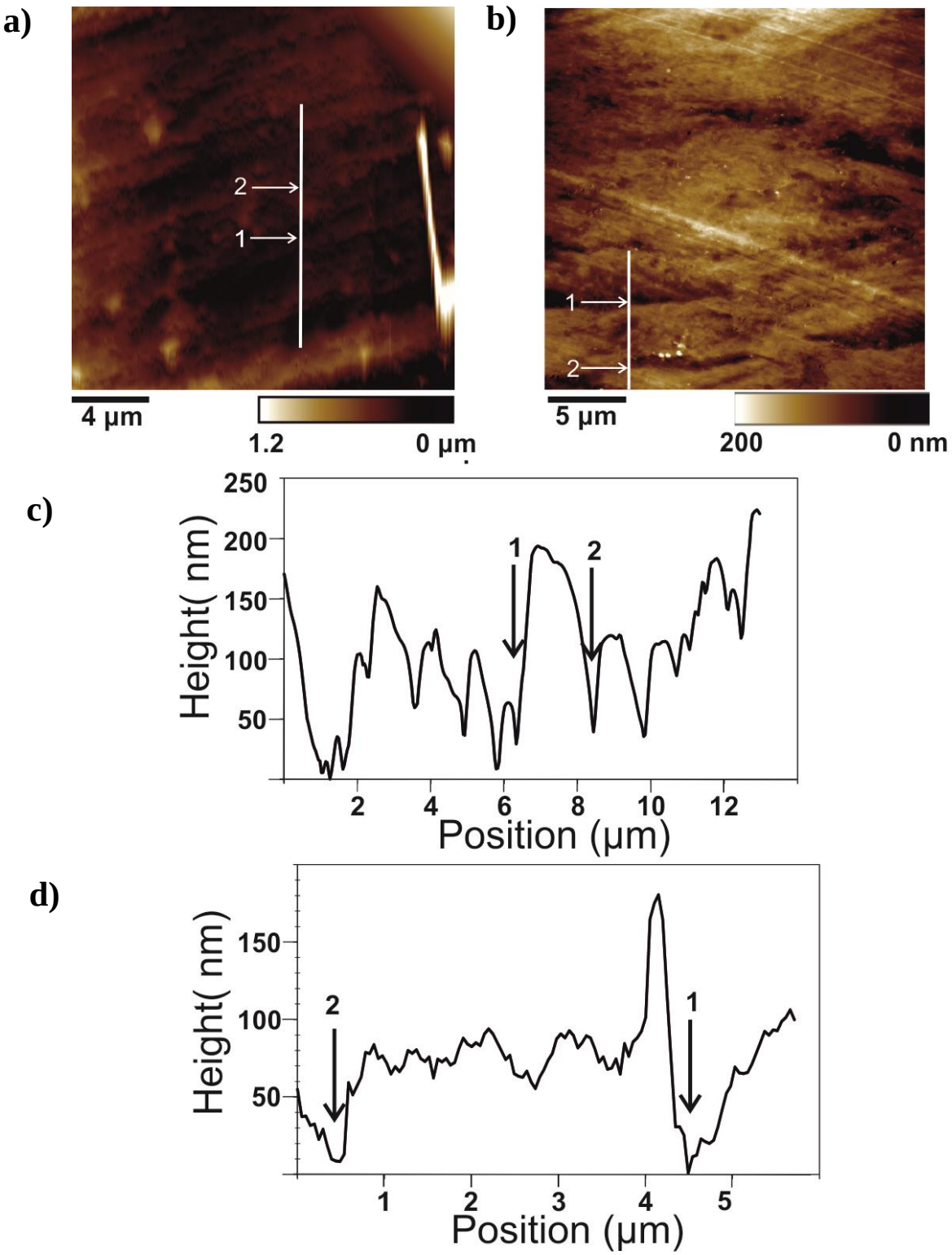

Figure 4.12: a) Two-dimensional AFM image captured in the intermediate region of a cross-section area = 20 x 20 µm^{2,}, b) two-dimensional AFM image captured in the ventral region of a cross-section area = 25 x 25 µm^2, c) height variation over the surface for the line scan taken in a), with the arrows marking a cell; d) height variation over the surface for the line scan in b), with the arrows marking a structure of expected thickness of a cell.

4.5 Infrared Spectroscopy of the Nail Plate

Spectroscopic study of the plate was initially performed with Fourier Transform Infrared Spectroscopy (FTIR). Measurements were taken on nail samples collected from three donors. To record spectra for the intermediate region, the thickness of a nail sample was measured with a micrometer and then the plate was filed to 50% of the original thickness, using a file from a commercial lacquer pack. Spectra for the dorsal and ventral were recorded from their respective surfaces. The FTIR records the percentage transmission of light, which subsequently, was converted into absorbance using:

$$Absorbance = 2 - log_{10}(\%transmission) \tag{4.1}$$

Figure 4.13 displays the absorbance spectra recorded from a single nail sample on the dorsal, intermediate and ventral surfaces. For all measurements taken the intermediate signal was the weakest in transmission. This is likely due to be the larger amount of light scattered from the rough filed surface.

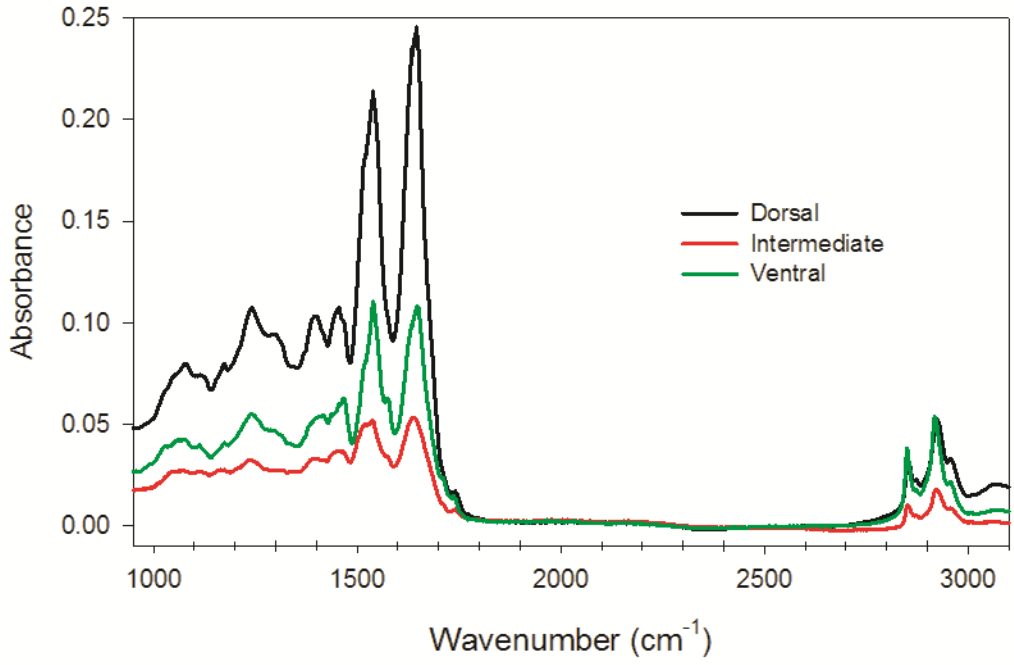

Figure 4.13: Infrared absorbance spectra obtained from a single donor, with the dorsal, intermediate and ventral regions of the plate plotted.

Table 4.1: Infrared peak assignments [105]

Wavenumber (cm^{-1})	**Peak Assignment**
2924	CH_2 stretching (symmetric)
2853	CH_2 stretching (anti-symmetric)
1745	Lipid ester carbonyl peak
1647	Amide I
1540	Amide II
1515	Tyrosine
1469	CH_2 bending band
1250	Amide III

To make comparison easier, the absorbance spectra were normalised by setting the Amide I peak equal to 1 allowing the ratio between this and other peaks to be analysed (see Table 4.1 for peak data). The spectra are displayed for each of the three donors for the three regions of the nail in Figure 4.14. In the 1200-1800 cm^{-1} there are several key features detailing structure of the plate: the Amide I peak is shifted from 1647 cm^{-1} to 1635 cm^{-1} in the intermediate signal for all three of the donors. This peak is a combination of two peaks, where a peak at 1650 cm^{-1} represents α-helical structure and a peak at 1639 cm^{-1} β-sheet structure. From this we can conclude that the intermediate layer has a larger proportion of β-sheet structure. The Amide II peak (1540cm^{-1}) is prominent in each of the regions, with a shoulder present at 1515 cm^{-1} corresponding to the tyrosine group. However, for the intermediate signal, the tyrosine peak has a similar absorbance as the 1540cm^{-1} peak, resulting in a wider peak. This is indicative of the lack of ordered protein

secondary structure in the intermediate layer. Apart from this, the peaks below 1500cm^{-1} are greater in intensity for the intermediate region, but the overall is very similar. There are no clear trends seen in the 2800-3000 cm^{-1} region of the spectra. These results show there is chemical variations in the different layers, and that the protein secondary structure varies across the plate.

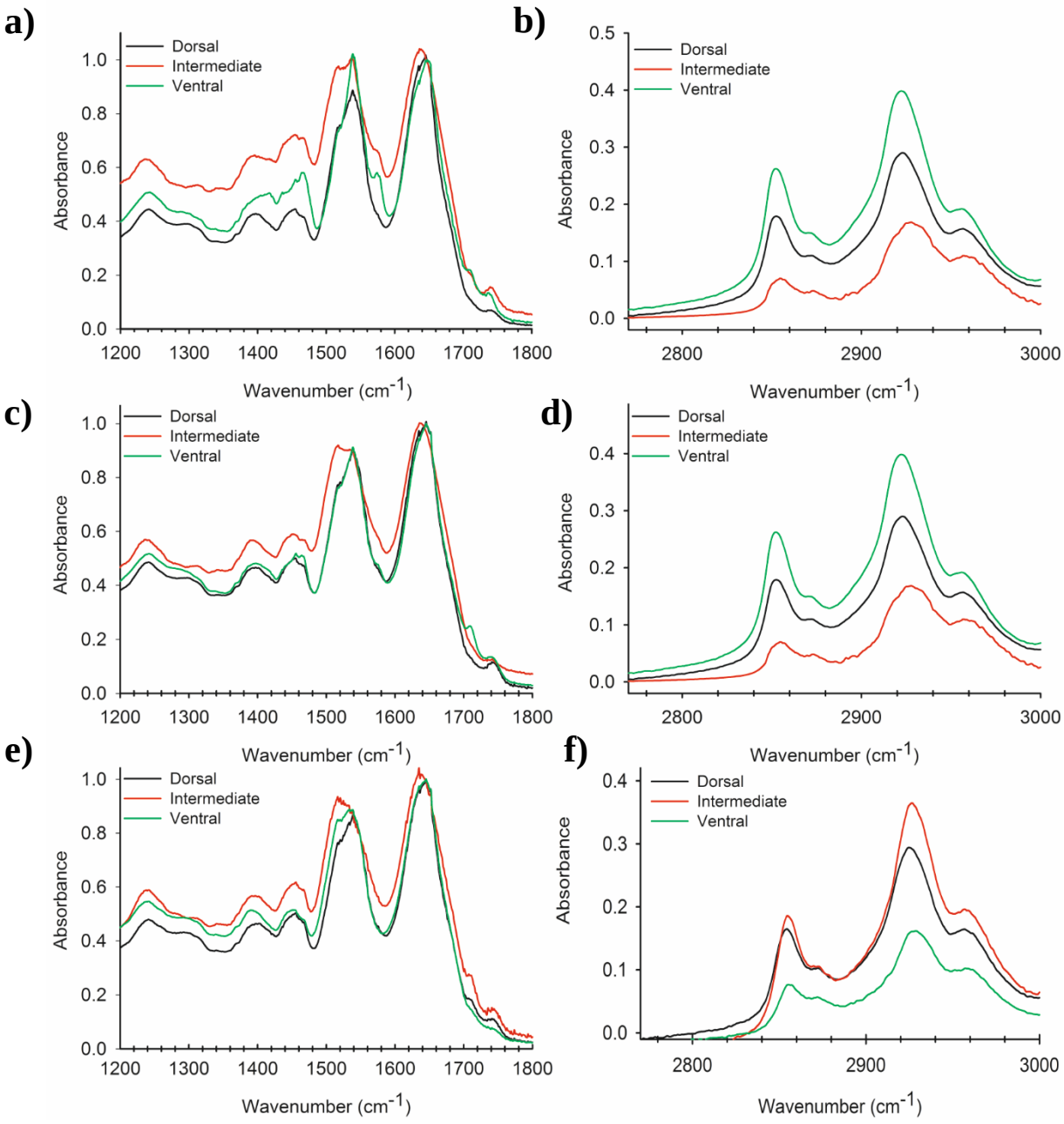

Figure 4.14: Absorbance spectra recorded on nail plates from three donors showing key features in the 1350-1800 and 2800-3000cm^{-1} regions; donor 1 a) and b), donor 2 c) and d), donor 3 e) and f).

4.6 Raman Spectroscopy of the Nail Plate

Nail plates from three donors were cross-sectioned with two nails per volunteer prepared. Raman spectra were recorded using the line scan feature across the plate using 0.01% of the maximum laser power available (approximately 80 mW), with an average taken from 10, 0.5 s acquisitions.

From the raw spectra shown in Figure 4.15a), it was clear there was variation in the background intensities across the nail plate. To measure this we define the Characteristic Raman Intensity (CRI), a measurement of the total intensity recorded over a broad range of the spectra (700-1700cm^{-1}). CRI for the donor's nails is plotted in Figure 4.15b), to account for the variation in donors nail plates the thicknesses were normalised to equal 1, in such a way that '0' was the ventral surface and 1 the dorsal surface. It is immediately clear the signal is stronger in the outer regions of the plate, especially in the ventral region. This could be related to variation in the protein secondary structure of these regions, as seen by FTIR. It has also recently been shown that morphology of the sample can impact the signal [90,91] and it may well be that the differences in the physical structuring of the cells in these regions results in a stronger signal.

Raman spectra were recorded on two nails from each of the three donors and processing performed as described in Section 3.5. Figure 4.16 displays spectra recorded from across the thickness of these nails : a) Displays spectra recorded in the first 20 % corresponding to the dorsal section, b) displays spectra recorded in the intermediate region of the plate, between 50-70% thickness, and c) displays spectra from the bottom 20%, corresponding to the ventral region.

To begin, intra and inter-donor variability are low for the spectra recorded in each of the regions, no peaks are apparent in one donor that are absent in another. Comparing the spectra recorded from different regions to each other it is clear that the spectra recorded in the ventral, and to a lesser extent the dorsal, are noisier than those recorded in the intermediate region. The primary reason for this is the high level of background signal recorded in these regions.

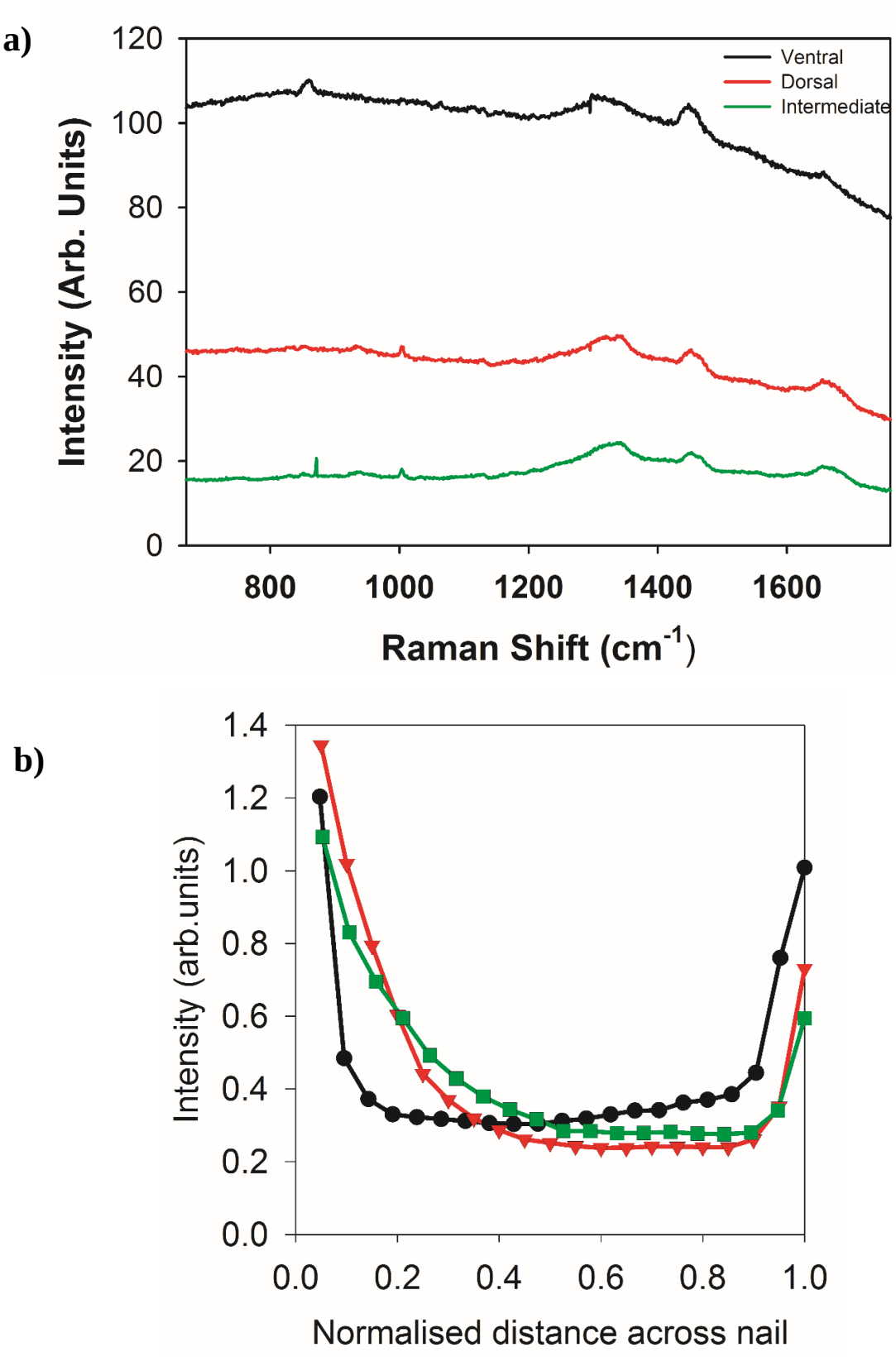

Figure 4.15:a) Spectra record from the Dorsal, Intermediate and Ventral regions of a nail plate. b) Characteristic Raman intensity measured across the cross sections of three nails. The ventral surface is at 0, the dorsal is at 1. Recorded with 785 nm laser

Table 4.2: Raman peak assignments [81]

Raman Shift (cm^{-1})	**Peak Assignment**
2933	CH_3 symmetric
2875	CH_2 symmetric
1670 **1649**	β sheet Amide I α helix
1616	Tyrosine
1447	CH_2 scissoring in lipids and $\delta(CH_2)$, $\delta(CH_3)$ in proteins
1315	CH_2 deformation
1273	Amide III (NH) and (C-N)
1127 1030	Acyl backbone chain conformation in lipids

Comparison of the Raman spectra with the FTIR from the previous section shows peaks appearing in Raman spectra, which are absent in the FTIR spectra and *vice versa*. The first difference to note is the amide II peak that features so strongly in the FTIR spectra at 1540 cm^{-1} is almost non-existent in Raman spectra: in the FTIR spectra the amide II peak is 80-90% magnitude of the amide I peak (1647 cm^{-1}), in the Raman spectra it is a small broad bump barely visible over the background signal.

In contrast, the peak at 1450 cm^{-1}, CH_2 scissoring in lipids, has the highest intensity in the Raman spectra greater than the Amide I peak, yet is wholly lacking in the FTIR spectra. The 1465 cm^{-1} shoulder seen on this peak in the Raman signal, is the strongest peak in this region on the FTIR spectra but is still far smaller in comparison with the Amide I peak.

According to the data for the amide III peak it should be found at different locations with FTIR and Raman, 1245 and 1273 cm^{-1} respectively. The peak is part of a broader feature in the Raman spectra, yet is clearly recognizable in the FTIR spectra in Figure 4.14. The peaks seen at 1000 cm^{-1} (CC aromatic), 1318 cm^{-1} (CH_2 deformation) and 1345 cm^{-1} (CH_2 deformation) in the Raman spectra are also lacking in the FTIR. The rule of mutual exclusion states no normal modes can be both Infrared and Raman active in a molecule or bond that possesses a centre of symmetry [107].

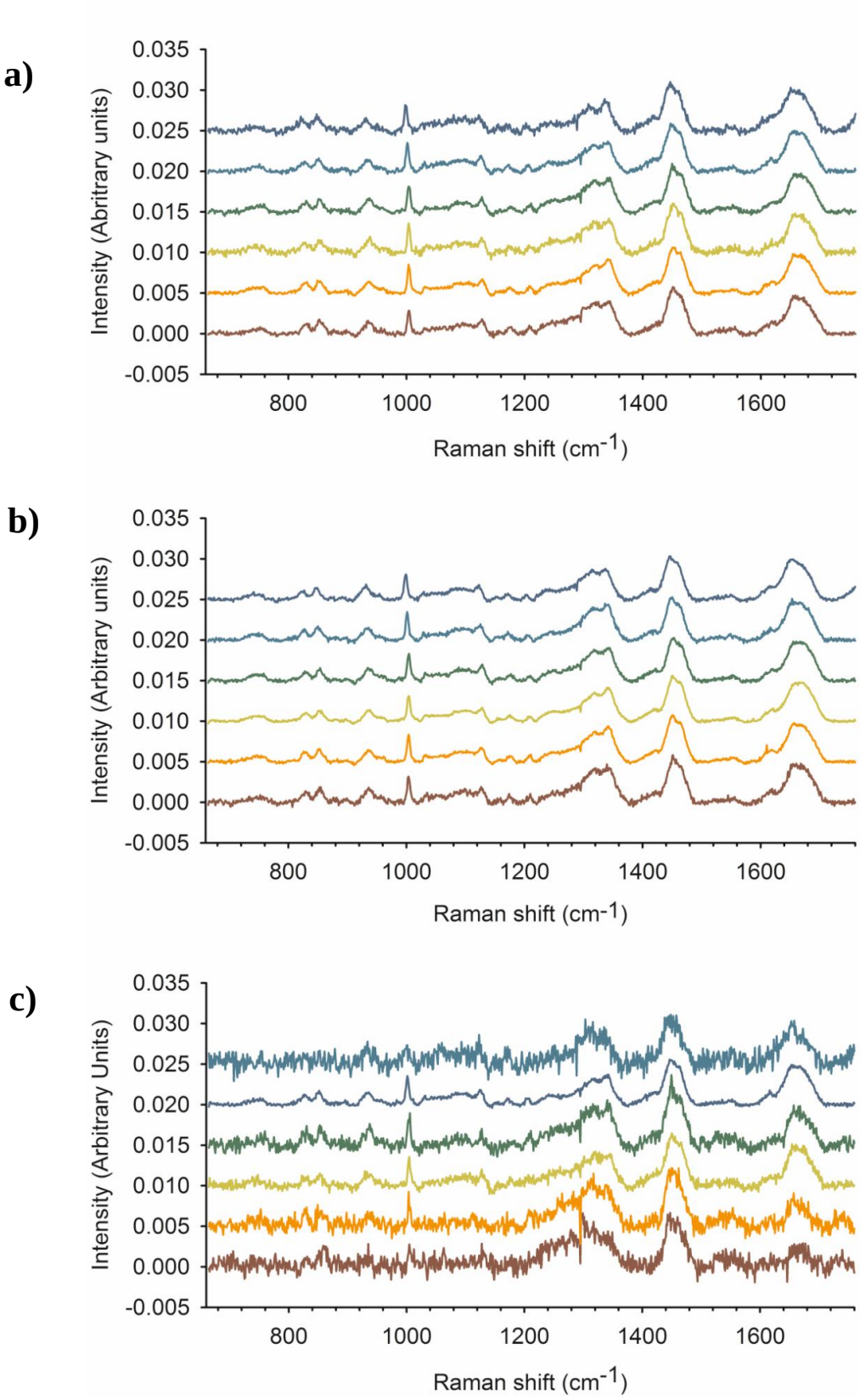

Figure 4.16: Raman spectra acquired from nail plates; a) dorsal region b) intermediate region c) ventral Region. Each graph shows six plots, with spectra recorded for two nails from each of the three donors. Recorded with 785 nm laser

4.6.1 Nail Treatment with a Chloroform-Methanol Solution

The next investigation saw the removal of lipids from the plate and subsquent detection with Raman. Variation in the lipid across the plate would result in an uneven decrease in spectra recorded from the nail for peaks that were lipid dependent. A chloroform-methanol solution (2:1 ratio) was prepared to remove the lipids from the nail plate. Nail samples were cut into two pieces and microtomed separately, the first piece from each donor was submerged in the chloroform-methanol solution for 30 minutes, and was then washed to remove any solution. The second piece was used as a control sample.

Spectra were taken across the samples covering the three regions of the nail. Two spectra were recorded for each point of the scan: the first covered the range of 950-1800 cm^{-1}; the second, in the range of 2800-3100 cm^{-1}. The CRI values were greater for the treated samples across the entire ventral and intermediate region, suggesting the treatment had affected the nail plate structure.

The spectral processing performed on the normal nail samples was repeated; in addition, the treated spectra were normalised to the Amide I peak at 1660 cm^{-1} of the control spectra as the solution should not affect the protein content. Figure 4.17 displays averaged spectra taken from several donors, with the chloroform treated samples displayed in red compared to the untreated sample shown in black. The peak at 1130 cm^{-1}, representing the acyl backbone chain conformation in lipids, is greatly reduced across all three regions: dorsal, ventral and intermediate. In addition. 1030 cm^{-1}, another skeletal lipid peak, is reduced especially in the ventral region, where the highest proportion of lipids is reported [12]. Figure 4.18 displays plots recorded in the 2800-3100 cm^{-1} region. The peaks at both 2933 cm^{-1} and 2875 cm^{-1} are reduced for all three samples with treatment; as seen in Table 4.2, these peaks correspond to CH_2 and CH_3, found in both lipids and proteins. It is likely that this reduction results from the decrease in lipid from the plate. The decrease at 2933 cm^{-1} is greatest in the ventral region,

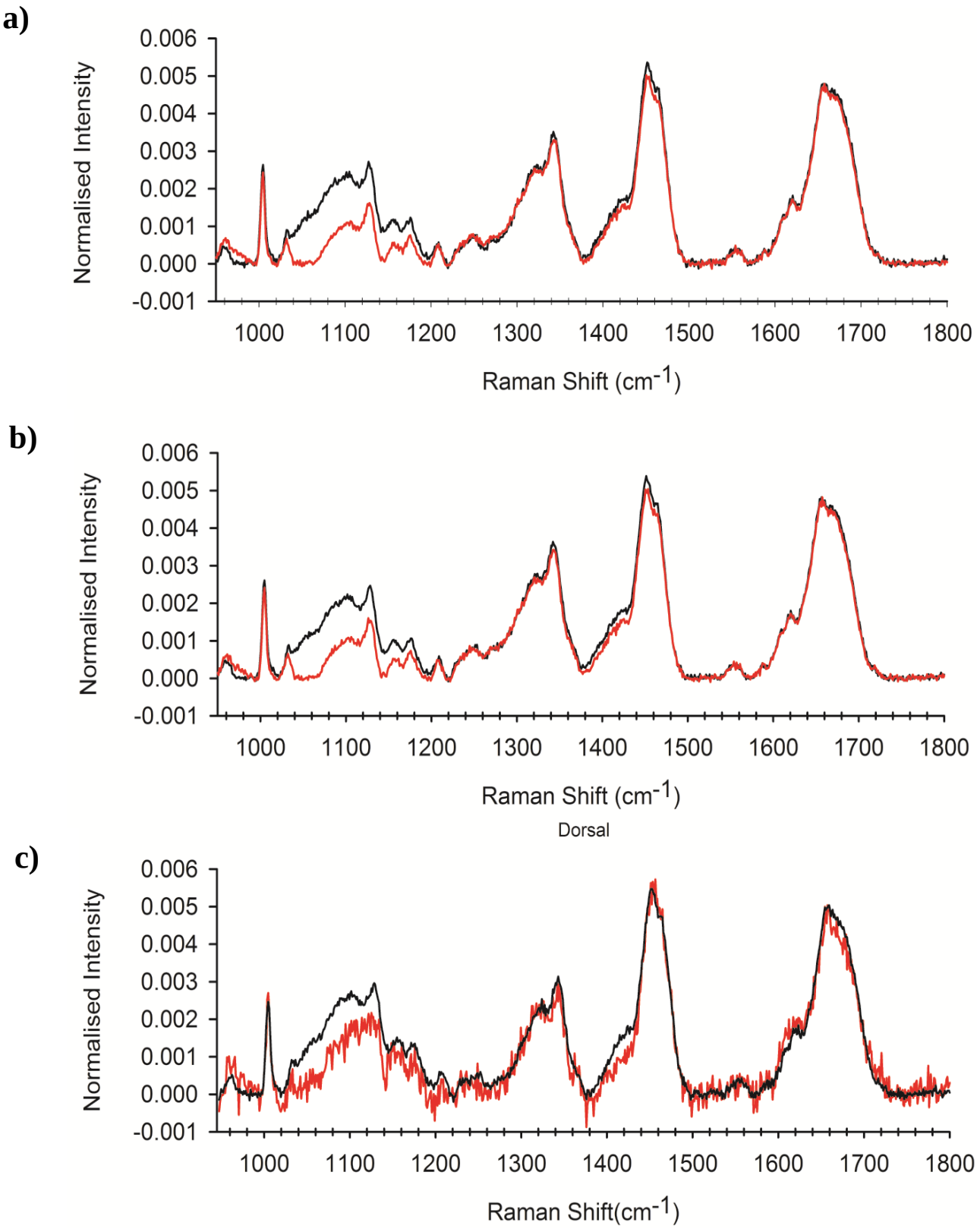

Figure 4.17: Raman spectra covering 950-1800 cm^{-1} recorded for nails treated with chloroform/methanol solution shown in red, and control nails in black; a) spectra recorded in the dorsal region, b) spectra recorded in the intermediate region, c) spectra recorded in the ventral region. Recorded with 785 nm laser.

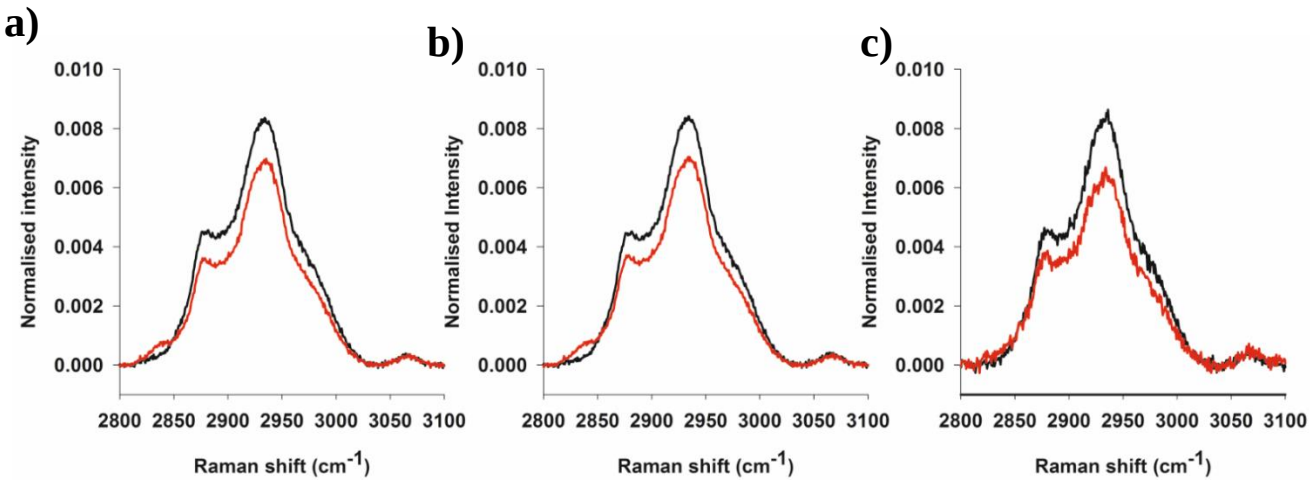

Figure 4.18: Raman spectra covering 2800-3100 cm^{-1} recorded for nails treated with chloroform/methanol solution shown in red, and control nails in black; a) spectra recorded in dorsal region, b) spectra recorded in intermediate region, c) spectra recorded in ventral region. Recorded with 785 nm laser

4.7 Summary

The nail plate has been studied with several microscopic and spectroscopic techniques to gain understanding of the structure. Macroscopically the nail is a hard, semi-transparent concave structure. Under low magnification optical microscopy the plate appears a dense wall of cells, in which it is challenging to identify individual cells due to poor contrast. SEM and AFM provide clearer detail of individual cells, and help display the tightly bound, irregularly stacked cellular structure of the plate.

FTIR spectra for all samples displayed variation in the secondary structure of proteins across the plate thickness, with a higher concentration in the β-sheet form in the intermediate region, along with variation in the tyrosine content present. The Raman background signal is much stronger in the dorsal and ventral regions of the plate in comparison with the intermediate. This could possibly result from the variation seen in the cell stacking in these regions.

A three layer model is often referred to in the literature, but defining clear dorsal, intermediate and ventral regions is challenging. Even with the topographical capability of the AFM it was difficult to identify any clear boundary across the plate. There is in reality a more gradual change across the nail thickness of the cell geometry, chemical composition and structure.

For subsequent chapters, the normal nail studied with these microscopic and spectroscopic techniques is well known, allowing observation of changes caused by optical drilling, and discussion of the laser-tissue interaction.

Chapter 5

Development of an Optical Drilling Technique

5.1 Introduction

The treatment of nail infections by topical therapy is hindered by the low diffusion of drug across the nail. Laser poration has already been demonstrated as a versatile technique to overcome the outermost layer of the skin, a barrier sharing many similarities with the nail. The process of skin poration is well understood, having been investigated over the last 3 decades [71,108-110]. In comparison, research into nail poration is far sparser. The first paper in which the nail was porated, published in 1997, presented a comparative study for 4 different pulsed laser systems; the pores with the least damage to the surrounding tissue were created with nanosecond pulses, the shortest of those tested [75]. However, no further research was undertaken until 2014, when two separate groups used commercial medical systems, commonly used for skin resurfacing, to porate the nail. These CO_2 lasers utilise millisecond infrared pulses. The first group porated the nail, and imaged the pores using optical coherence tomography [76]. Meanwhile, the paper published by the second group performed a clinical investigation in which patient's nails were porated, followed by the daily application of a topical cream; 92 % of the patients showed a clinical response to the treatment [77]. Unfortunately, no information on the number of holes per nail, or their geometry was given.

Greater understanding of the radiation-tissue interaction is needed to exploit the potential of laser poration in the treatment of nail disease. The development of hollow core photonic crystal fibres provides the capacity to guide ultrashort pulsed (10 s of femtoseconds) visible light [111]. Fibres have been shown advantageous for the poration of skin, the smaller beam spread eases delivery of a sufficient energy density for poration of tissue [74]. Staining biological tissue with an ink before poration is an effective technique that lowers the poration threshold and provides a kick-start to the process [112].

This section details the development of a technique in which a fibre delivered, femtosecond pulsed laser (λ=532 nm) was used to porate the nail plate. As the absorption of light by the nail at this wavelength is very weak, it was necessary to alter the surface to increase absorption. A permanent marker provided a simple solution but, to optimise the process, a dye with strong absorption at the wavelength of the laser was sought. Ruthenium Red, Iodine, Carbon Cement and Nile Red (NR) were all tested; their coverage of the plate surface and the quality of pores created on the nail was assessed. In addition, the Raman spectra of the dyes were assessed. Taking these into account, Ruthenium Red was selected as the best stain.

Following this, the effect of the laser parameters on the geometry of the pores and the damage to the surrounding tissue was studied. To reduce the thermal damage surrounding pores it was necessary to vary the grouping of pulses. Unfortunately, both of the lasers used had a fixed repetition rate (20 and 80 MHz). It was found that the installation of an optical chopper, which provides alternating open and closed periods, drastically reduces the damage surrounding pores. A chopper disk with 10% exposure was also tested. With this thermal damage was reduced, but it required a longer time to drill the plate. Finally, through familiarity with the laser system and its ability to penetrate the nail barrier, a series of regimens were shown to be suitable for the creation of arrays for permeation experiments.

5.2 Selection of a Nail Dye

Absorption of visible light by the nail is very weak, and so the first stage of the investigation required selection of an ink to aid poration. Figure 5.1a) provides an

example of an unaltered nail plate exposed to laser A (rep rate 20 MHz, pulse length 300 fs), a 140 mW average power used for a 10 s exposure. The energy absorbed by the nail was insufficient for ablation but enough for thermal heating to leave a mark. Similar results were seen when the nail was exposed to the beam when it wasn't frequency doubled (λ=1064 nm), but with even larger regions of damage. The drilling of pores through the plate was facilitated by the application of a permanent marker to the surface. Figure 5.1b) demonstrates a pore drilled with 70 mW of power and 1 s exposure, which completely penetrated the nail plate.

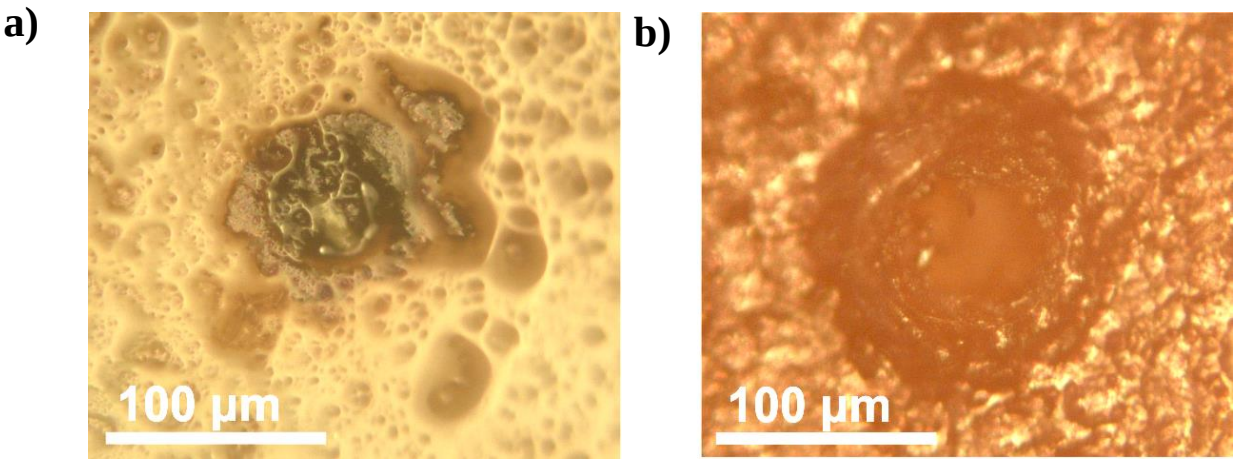

Figure 5.1: Optical microscope images taken of sites exposed to the laser beam: (a) shows a site exposed on unaltered nail, with a 140 mW power and 10 s exposure time; (b) is a site on a nail stained with the black permanent marker; the power was 70 mW and the exposure time was 1 s.

The use of the permanent marker showed one major limitation: when trying to aquire Raman spectra the signal was swamped with a background signal several times stronger than the characteristic signal, which hid the nail peaks discussed in Chapter 4.

The unsuitability of studying permanent marker stained nails with Raman provided the motivation to study other dyes/stains. To judge the suitability of a stain several criteria were used. Firstly, the dye should strongly absorb light at the lasers wavelength (λ = 532 nm). Secondly, the consistency of coverage was assessed. Thirdly, the pores drilled and the damage caused to the tissue surrounding the edge was analysed optically. Finally, the

Raman spectra were considered to ensure the dyes did not affect the spectra of the nail. Four staining solutions were chosen; Ruthenium Red, Iodine, NR and a Carbon Cement.

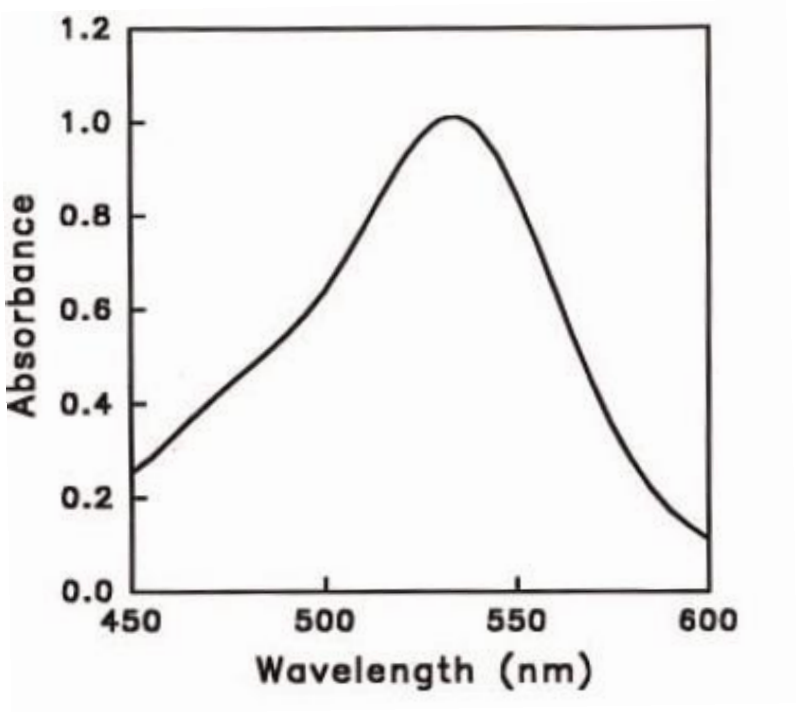

Figure 5.2: Absorption spectrum of Ruthenium Red in distilled water (0.004% w/v) in the visible region. The maximum absorption peak is close to λ=532 nm, and so it strongly absorbs the radiation produced by the laser used. Reproduced with permission [113]

The four dyes were applied to nail samples from the same donor. Solutions were prepared at a concentration of 1 mg/ml for Iodine (solvent: methanol), RR (solvent: methanol), and NR (solvent: propylene glycol). Nail samples were submerged in the solution for 15 minutes and then removed to dry for 5 minutes. Carbon Cement required no preparation and was applied with the brush supplied by the manufacturer. The absorbance spectrum for RR is given in Figure 5.2.

Figure 5.3 displays optical images, taken with the digital USB microscope, of nails that were porated with powers of 225 mW and 150 mW for 1 s. The nail samples were stained with a) Iodine, b) RR, c) NR and d) Carbon Cement. With regard to the coverage of the dyes, both Iodine and RR consistently stain the nail plate, with no bare patches or clumps. In contrast, NR does not stain well as there are bare patches where the dye has not

adhered. Carbon Cement covered the nail surface even more poorly, its particulate nature resulting in large clumps in certain areas whilst others are bare.

Next, the appearance of the pores was studied. Qualitatively, it was observed that the surface damage surrounding the pores drilled in the sample stained with Carbon Cement was worst, Figure 5.3d). Due to its uneven coverage some sites on the NR stained nail that were exposed to the laser were unporated, these are indicated with green arrows in the optical image in Figure 5.3c). Due to this reason, both NR and Carbon Cement were ruled out.

Higher magnification images of the pores on Iodine and RR soaked nails are shown in Figure 5.4, a) and b) respectively. These pores were drilled with 1 s exposure and 150 mW of power. The pores on the Iodine sample have a greater level of damage surrounding them, whilst the pores on the RR sample have a clear hole through the plate.

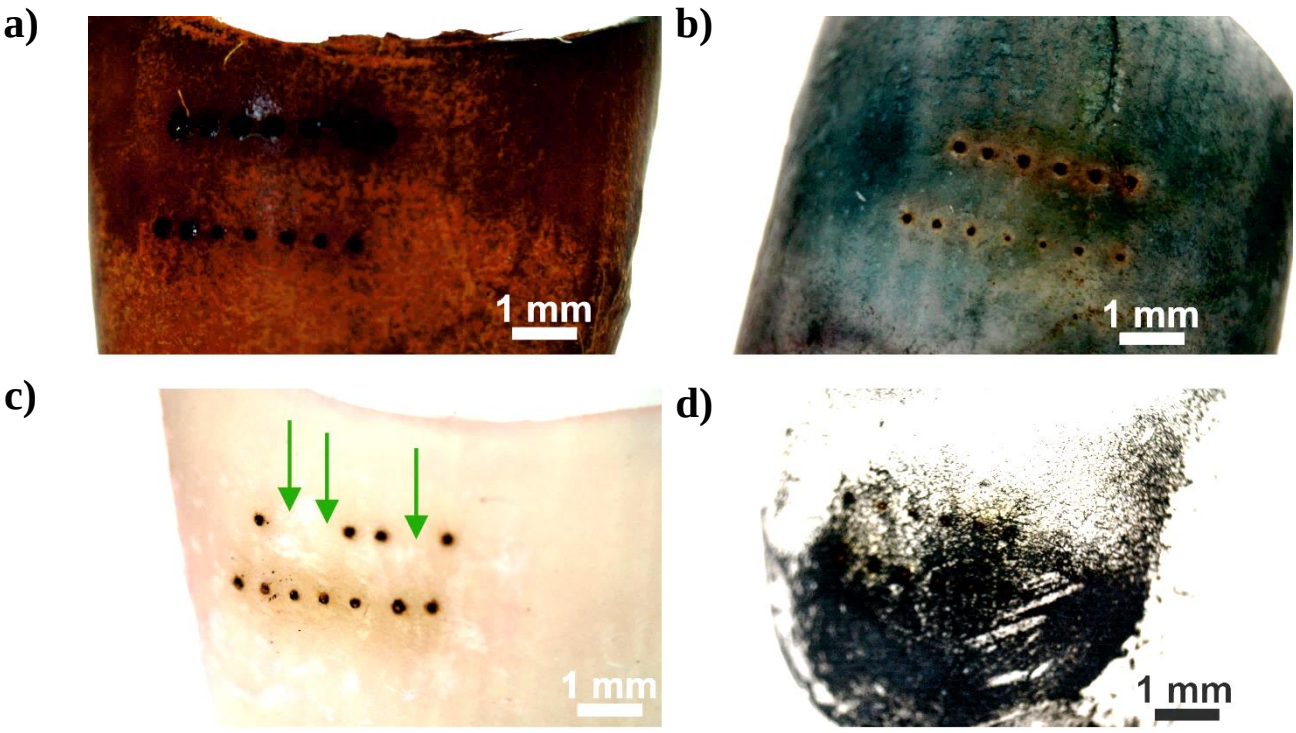

Figure 5.3: Optical images of nail plates that were stained and exposed to a beam (laser A) with average powers of 225 mW (top rows) and 150 mW (bottom rows), for 1 s: a) Iodine b) RR c) NR d) Carbon Cement. Note the green arrows in c) showing sites which were exposed to the beam but with no pores present.

a)

b)

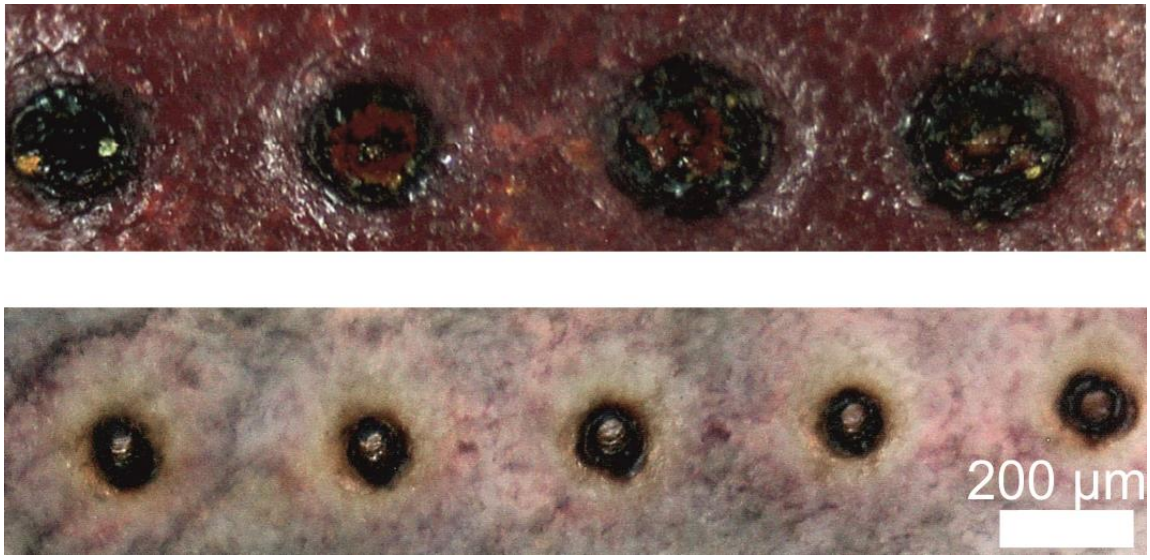

Figure 5.4: Higher magnification optical images of pores in nail plates that were stained and exposed to a 225 mW average power and 1 s exposure: a) Iodine b) RR

Raman spectra were captured for Iodine and RR with a 785 nm excitation source and ten, 1 s acquisitions. Figure 5.5a) displays raw spectra before any processing, the first observation was the large background signal produced by the Iodine solution, and similar to the permanent marker ink, it would obstruct any signal from the nail. Figure 5.5b) displays the Raman spectra after background removal. For the Iodine solution, several broad peaks sit across the 1000-2000 cm^{-1} portion of the spectra, where many of the key peaks in the nail lay. In contrast, seen in Figure 5.5c), the peaks in the RR spectra lay outside of this region. Considering all of these factors, it was decided that RR should be used for further experiments.

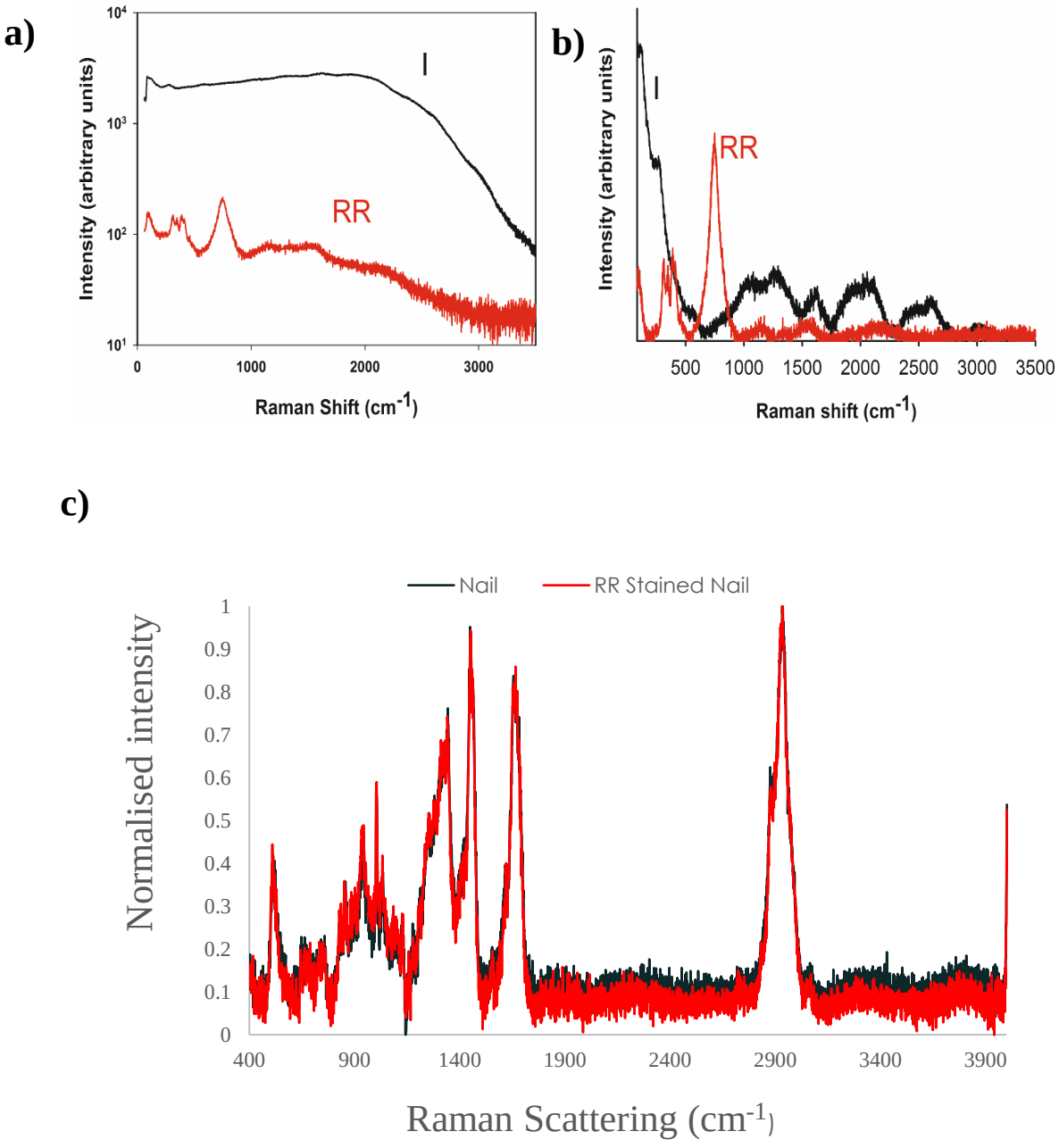

Figure 5.5: Raman spectra acquired of Iodine solution (I) and Ruthenium Red (RR). a) Raw spectra with no processing. b) Spectra processed with background removal and noise cancelling. c) Raman spectra for a control nail, and one which has been stained with Ruthenium Red

5.3 Pore Geometry

5.3.1 Pore Diameter

With the selection of Ruthenium Red to stain the nail and facilitate poration, the effect of laser parameters on the geometry of pores was then investigated. There were three exposure parameters in the setup that could be adjusted (Figure 3.4). Firstly, the polarising beam splitter allowed variation of the average power before the beam entered the frequency doubling crystal. Secondly, the shutter was used to provide discrete exposure times. Thirdly, was to use an optical chopper, which allowed variation in the grouping of pulses irradiating the sample. The 'sample exposure time' was half the exposure time chosen for the shutter, due to the 1:1 ratio of open: closed for the chopper, in total there were 10 open and 10 closed windows on the disk. The three chopper frequencies used were 20, 200 and 1000 Hz corresponding to windows of $\frac{1}{400}$, $\frac{1}{4000}$ and $\frac{1}{20000}$ s.

The grid displayed in Figure 5.6 presents optical images of pores drilled with a 0.5 s sample exposure time, the scale bar is 50 μm, and all of the pores were drilled on the same nail. The most immediate observation is the reduction in the damage surrounding the pores for those drilled with the chopper. However, there is no clear advantage to increasing the chopper frequency beyond the lowest setting of 20 Hz. With regards to the pore centres, those drilled without the chopper are messy, and the edges are challenging to define. Subsequently, samples drilled with exposure times of 0.125, 0.25 and 1 s were investigated and the same trends were observed. No trend was observed for the diameter of the pore when exposure time was varied. However, it is clear from the optical images that pore diameter is dependent on the power. Diameters were measured using ImageJ for the pores drilled with different times and different donors, with the results displayed in Figure 5.7. Generally, as the power is increased the pore diameter increases. In addition, this plot provides quantitative proof that drilling with the chopper produces smaller pores.

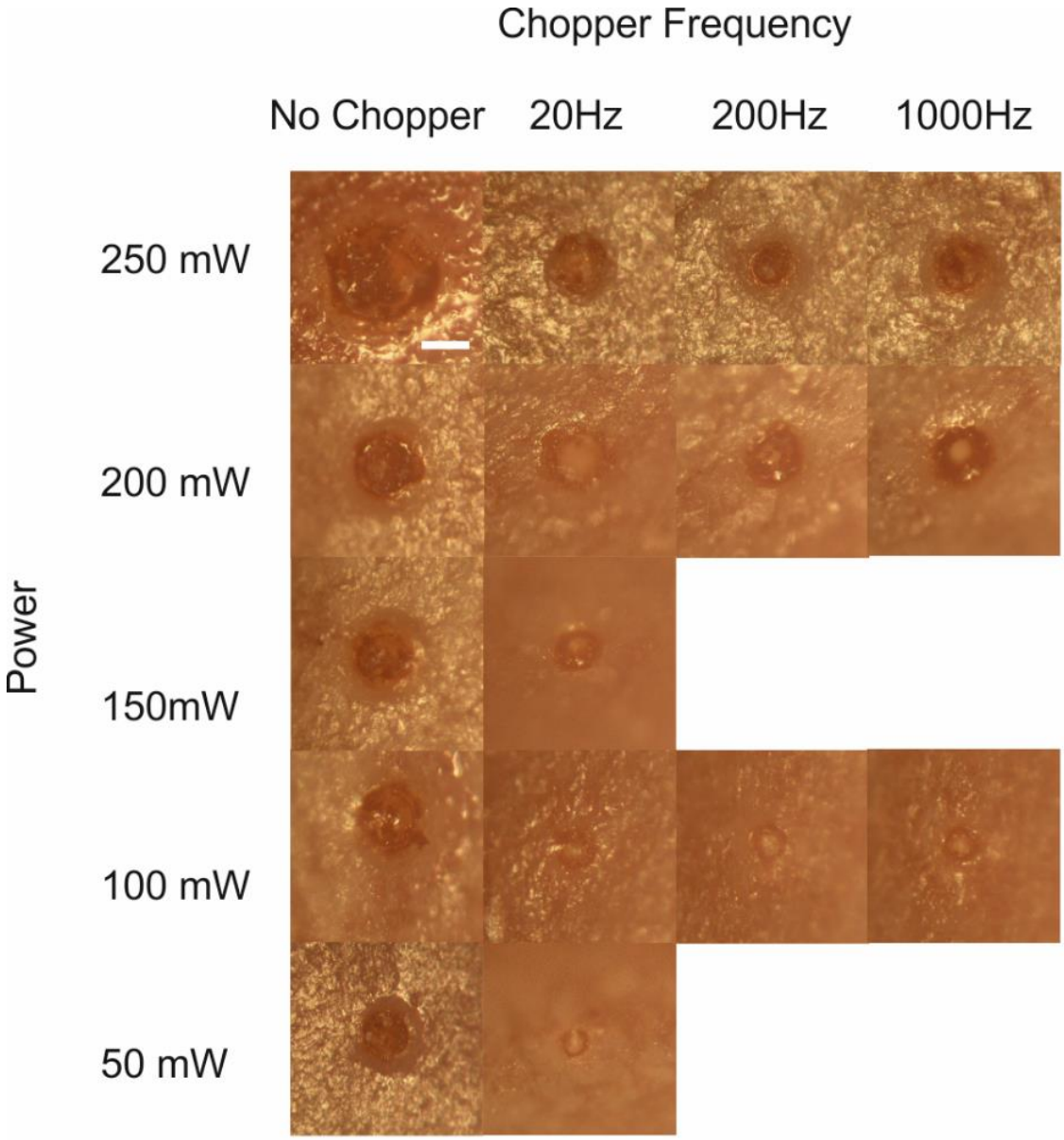

Figure 5.6: Optical images of pores created on a Ruthenium Red stained nail with a 0.5 s sample exposure time. The scale bar is 50 μm. Laser A used (repletion rate = 20 MHz, pulse length = 300 fs).

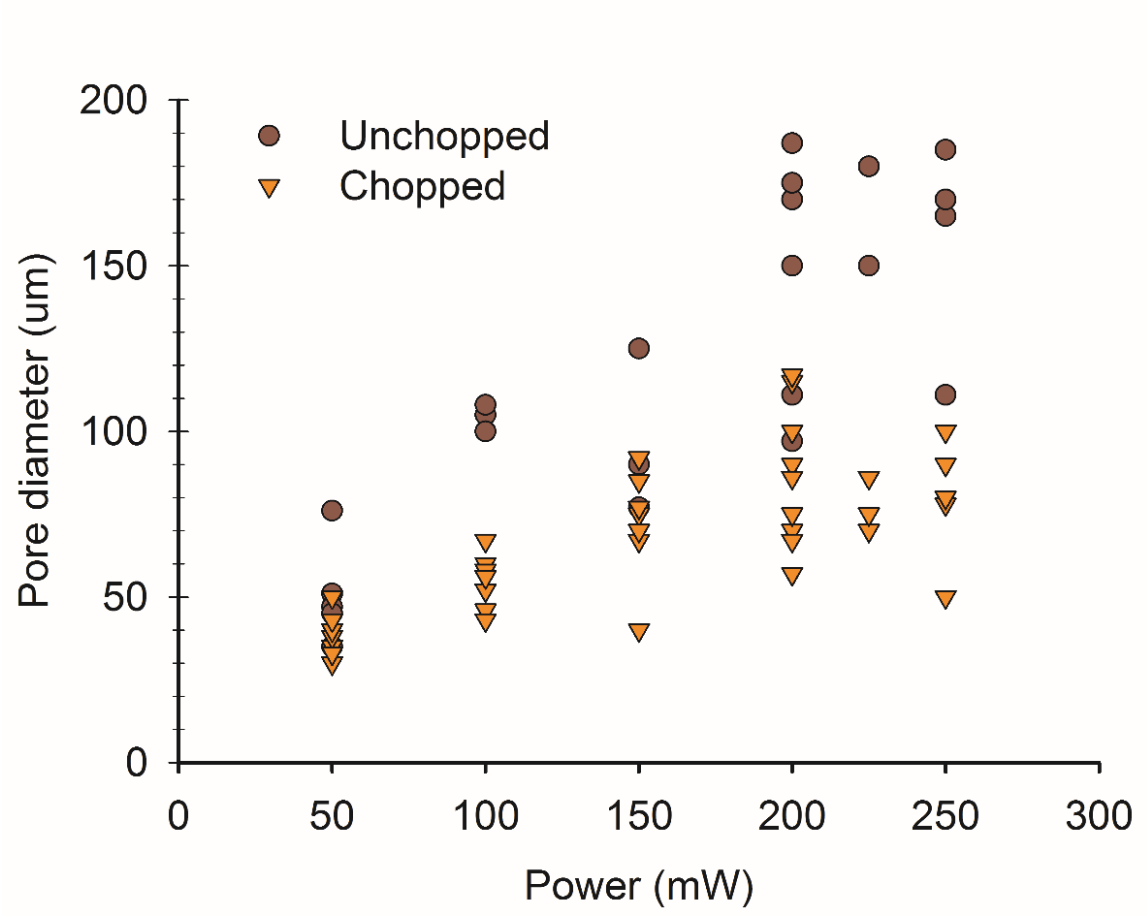

Figure 5.7: Pore diameters as a function of power for nails porated with both chopped and unchopped beam. Data showed no trend for diameter with time, therefore for each power several different shutter times are included. Pores created with a chopper were generally smaller in diameter due to better dissipation of excess thermal energy.

The dependence of diameter on power is explained by the energy density distribution in the beam. For plasma mediated ablation, the energy density in a specific volume, must be great enough to liberate sufficient free electrons to cause optical breakdown in the tissue (see Chapter 2.5.1). The beam launched by the fibre has a Gaussian intensity profile.

The schematic in Figure 5.8 illustrates the profile of the beam for two powers (where $P_1 > P_2$).The ablation threshold is marked by the dashed line, a larger region of the profile is above the threshold in P_1, and so this beam would produce pores with a greater diameter, d_1.

Therefore, it is easy to understand the trends seen in Figure 5.7: as the power is increased, the intensity across the beam is also increased, resulting in a larger width of the beam above the ablation threshold. However, as the diameter seemed to reach a maximum at 150 mW, it is possible that this provides sufficient energy density across a width of 80 to 100 μm. The variability in pore diameter partly results from the definition of pore 'edges'. The widest region of the pore in the focal plane beneath the surface of the plate was used for analysis. However many pores were non-symmetrical, with the interior of pores containing coagulated material. The angle and distance between the fibre tip and the surface, may also be responsible for irregularities in the pores. Due to the curvature of the nail, it was challenging to maintain a constant distance and normal angle with the micrometre stage used. With regards to the difference in pores created with and without the chopper, radiation was absorbed into the tissue in the 'tails', with regions at the edge of the beam profile below the ablation threshold. It is probable that the chopper interrupts the beam providing windows in which no radiation is absorbed, allowing the energy in the tissue to diffuse. For samples produced without a chopper, a cumulative thermal effect builds up, causing a widening of the pores. Attention will be given to this in Chapter 6.

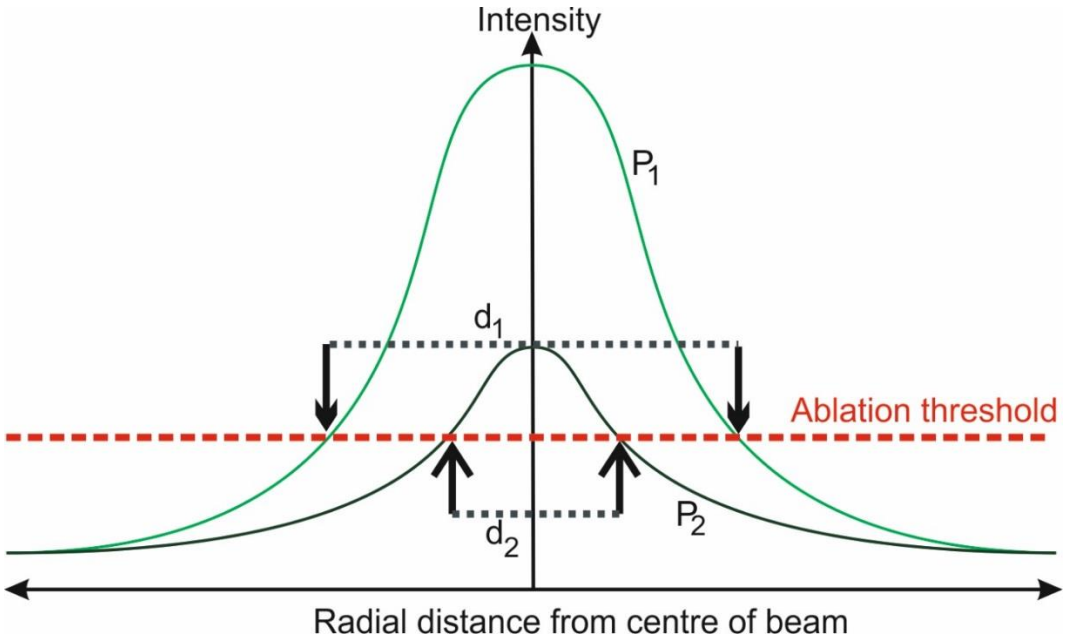

Figure 5.8: Illustration of light intensity as a function of distance from the beam centre. The ablation threshold indicates the intensity required for plasma mediated ablation to occur.

Pores with a large variation in appearance were created. Pores with a clear interior and minimal damage in their surrounding were classified as 'optimal pores'. Figure 5.9a) displays a schematic of a pore with two measurements: the diameter of the total damage region (d_{damage}) and the diameter of the pore (d_{pore}), for an optimal pore $d_{damage} \approx d_{pore}$. Optical images of ideal pores drilled on nail samples, at various powers and exposure times, are displayed in Figure 5.9b). From the pores in this image it is clear, as the exposure time was reduced, increasingly higher powers could be used whilst still minimising d_{damage}. This thermal damage is investigated quantitatively in Chapter 6.

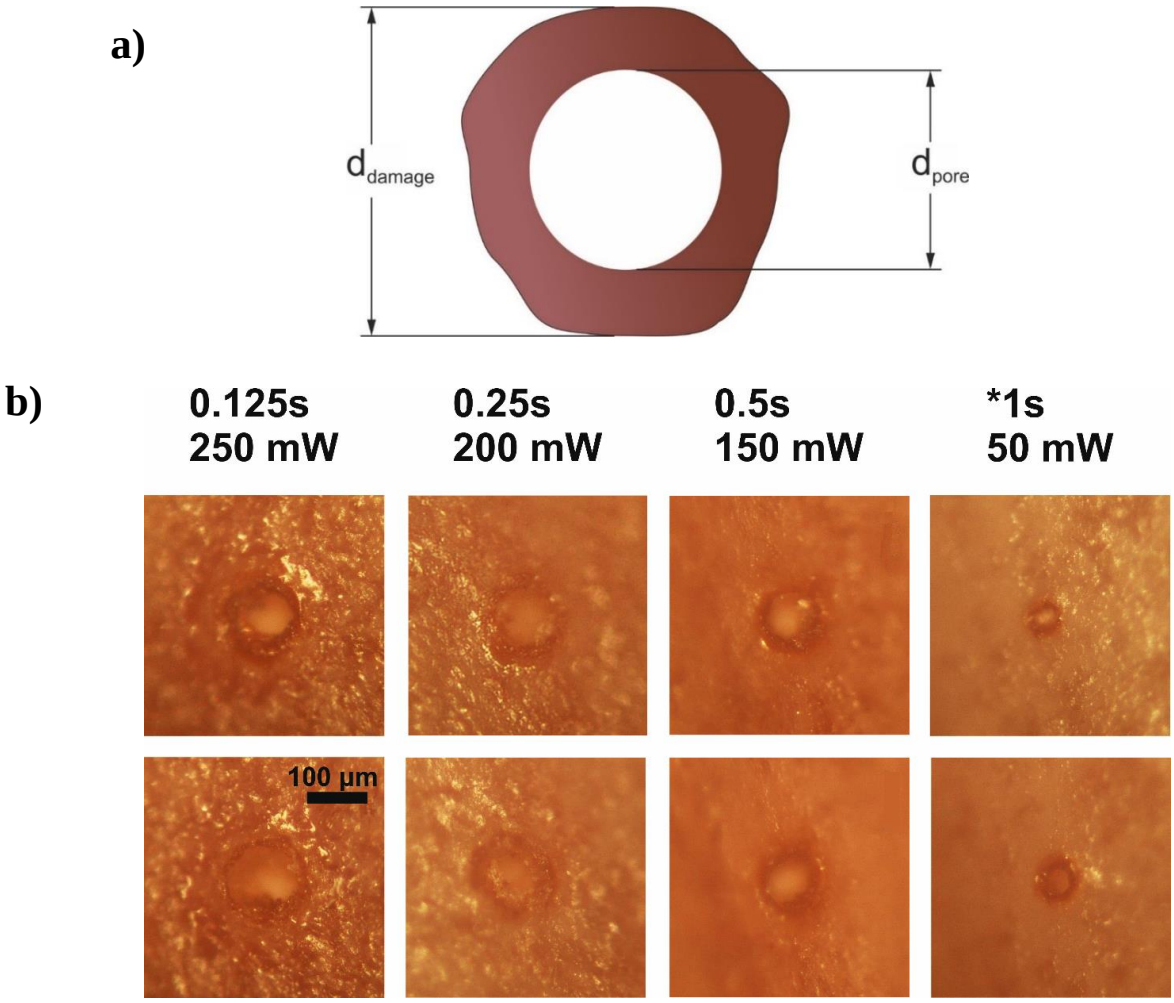

*Figure 5.9: a) Schematic detailing the pore diameter, d_{pore}, and damage diameter, d_{damage}. For an optimal pore $d_{damage} \approx d_{pore}$. b) Optical images of optimal pores drilled into the nail surface, with the sample exposure time and average power given.*No chopper was used for these pores. Laser A used (repletion rate = 20 MHz, pulse length = 300 fs).*

5.3.2 Pore Depths

It was easy to observe when pores had completely penetrated the plate when using this setup with *in vitro* nails, as the pattern appeared on the wall behind the plate. However, measuring the depth of pores which partially penetrate the plate is more challenging Investigation of the effect the different parameters had on pore depth was required, in order to better understand the drilling process. Initially, the interior of the pores was studied by cutting a cross section in the plate with a microtome. The biggest challenge microtoming the plate for the study of partially porated samples, was attempting to cut to the axial mid-point. It was extremely difficult to cut a pair of neighbouring pores exactly along the symmetry axis, due to the geometry of the nail and the blade used. As a result, some pores drilled with the same parameters appeared shallower than others.

Figure 5.10 displays optical images of pores drilled with laser A using an average power of 250 mW into two samples, with the total exposure time being varied through the shutter and chopper. The pores in a) were drilled with 1 s sample exposure that fully penetrates the plate. The interior was drastically darkened, with a concentrated band of white visible in the bordering region. The pores in b) were drilled with 20 Hz chopper frequency and 0.5 s sample exposure time. With these settings the distance penetrated is reduced by more than half, the pore reached 100 μm into the plate, which was ~30% of the nail's thickness. The pores shown in c) were drilled with a 0.5 s exposure, yet no chopper. The pores are broader than b), with damage extending to a greater distance from the pore edge. The two pores in d) were drilled with a 0.25 s sample exposure and 20 / 200 Hz frequency, and penetrate to the same depth within the error of microtoming.

As seen on the surface, the chopper reduces the diameter of damage surrounding the pore, which is clear when comparing a) with b) and b) with c). From these optical images it is clear the depth of penetration is reduced when the exposure time is reduced. Using the microtome to cut the nail to measure the depth of penetration was time consuming overall, and so an alternative technique was sought.

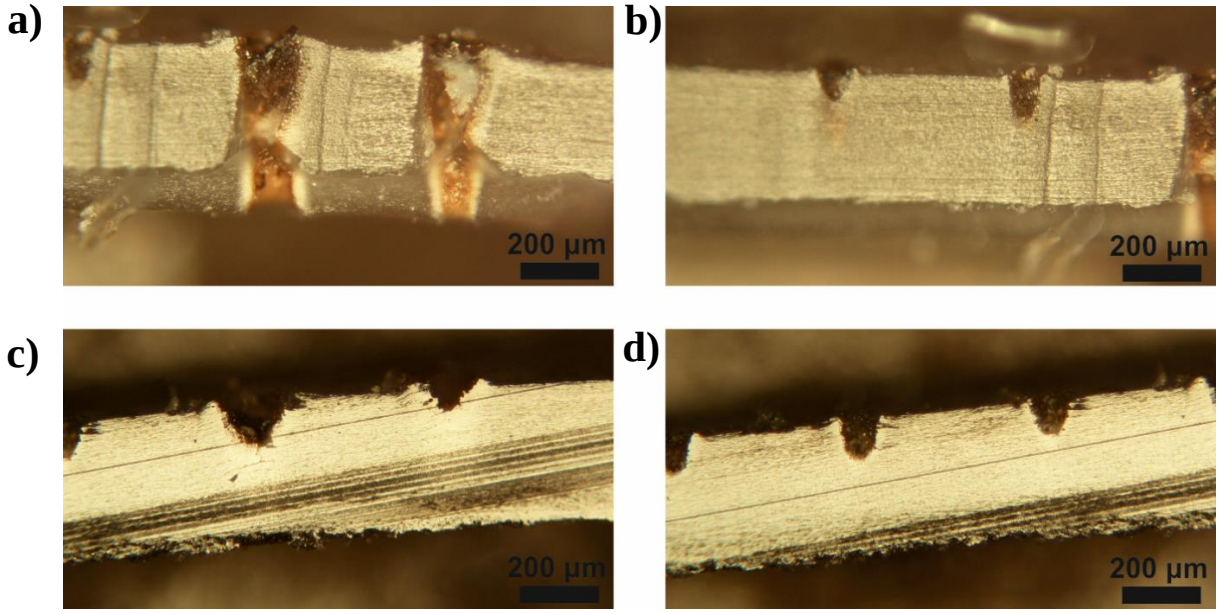

Figure 5.10: Optical images of cross-sectioned full a) and partial pores b-d) in nail plates for different radiation powers and exposure times. a) 250 mW, 1 s; b) 250 mW, 0.5 s, 20 Hz; c) 250mW, 0.5 s; d) 250 mW, 0.25 s, 20 Hz (left hand pore), 200 Hz(right hand pore). Laser A used (repletion rate = 20 MHz, pulse length = 300 fs).

Laser Scanning Confocal Microscopy (LSCM) was an alternative technique used to image the internal region of pores. With this technique, it was easy to resolve the interior of pores due to intact and burnt nail tissues fluorescing at different wavelengths. Images were acquired in two channels using two different lasers for excitation and were later overlapped. Figure 5.11 displays two pores imaged using LSCM: intact nail fluoresced, after excitation at 405 nm, visualised in blue, and nail physically damaged by poration is visualised in purple after excitation at 488 nm. The four panels for each pore were taken from a reconstructed x-z stack created in ImageJ, which were rotated through an 180^{o} angle.

For measurement of depth, the *z* value at the surface of the nail was obtained with LSCM. The interior of the pore was traced until the base was reached, and the z value again recorded. The total height was then calculated from the difference between the two values. Samples that were studied with LSCM were porated with a second laser system (Laser B). This laser had a 5 W output, in comparison to the 1 W of the first laser (laser A), and so powers upto 1.3 W were achieved at the fibre tip.

Utilizing LSCM, a wider range of powers and exposure times were tested to drill nail samples. In Figure 5.12, the depth of penetration is plotted against the exposure time for four powers. The points above the dashed line indicate those pores that fully penetrate the nail plate. For pores that fully penetrate the plate, the thickness of the nail is used for the depth. In fact, this is the lower limit of penetration, and it is possible these parameters would drill a greater depth of tissue. The cut-off for full poration of the plate is shifted to lower exposures as the power of the beam was increased. It is clear that the depth of penetration heavily depends on the exposure time, whilst higher powers also allow greater penetration for the same exposure time.

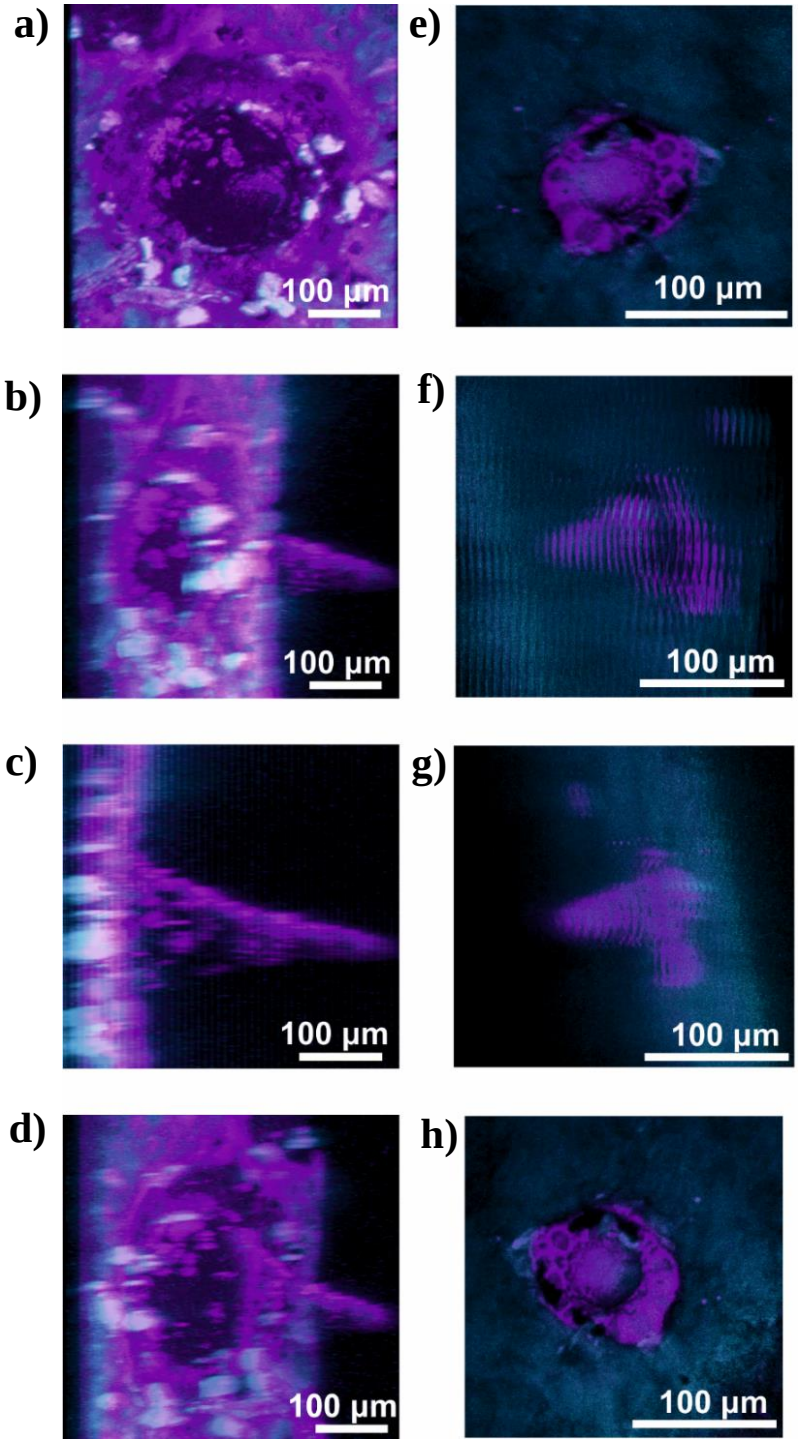

Figure 5.11: LSCM images of two pores that partially penetrate the plate. The purple regions are those that fluoresced after excitation at 488 nm, whilst those in blue are intact that fluoresced after excitation at 405 nm. A stack of images was acquired in the Z plane and stitched together using FIJI software to create a 3-dimensional model of the pore [101]. *Captures were acquired as the models were rotated through 180^{o} angle with a) & e) acquired on the dorsal surface. a-d) 500 mW, 0.125 s 20 Hz; e-h) 1000 mW, 0.003 s 20 Hz. Laser B used (repletion rate = 80 MHz, pulse length = 200 fs).*

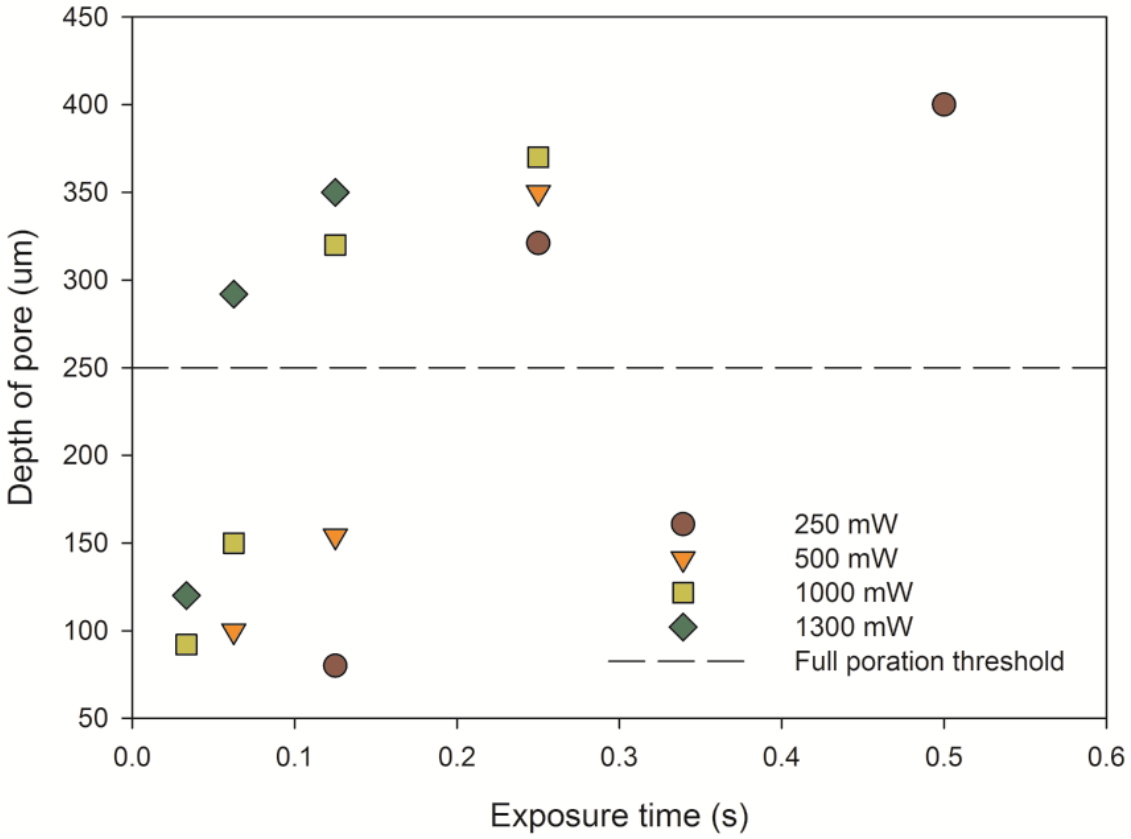

Figure 5.12: Depth of pore plotted against the exposure time for four average powers. All pores above the dashed line fully porated the p plates drilled, corresponding to the minimum plate that would be drilled with these parameters. Laser B used (repletion rate = 80 MHz, pulse length = 200 fs).

5.4 Single Slit Chopper

The incorporation of a chopper not only provided a reduction in the pore size, but also reduced the thermal damage surrounding the tissue. This concept was taken a step further by decreasing the window of exposure of the chopper. A custom blade was built for the chopper with a single window, $1/10^{th}$ of the circumference. With the chopper frequency set to 20 Hz, each period of exposure lasted 0.005 s, followed by a 0.045 s closed period.

Laser A was used for this work. The maximum achievable power of 360 mW was used for the drilling of every pore. The shutter was opened manually and exposure times measured with a stopwatch. Exposure times of 20, 15, 10, 5 and 3 s were used, resulting in sample exposures of 2, 1.5, 1, 0.5, 0.3 s respectively.

The optical images presented in Figure 5.13 display five pores created with the single slit chopper setup: it is clear that the pores are ‘optimal’ with a minimal ring of visible damage. The diameters are 70, 50, 45, 35 and 40 μm, smaller than those created in the previous section under the same exposure times.

Figure 5.14 displays the cross sections of 4 pores. The pore shown in a) was drilled with a 10 s shutter exposure (1 s total sample exposure), very little damage has occurred in the area surrounding the pore, and 40% of the nail has been penetrated. In comparison, the equivalent 1 s exposure with no chopper would penetrate the entire plate. The pore in b) was drilled with a 5 s shutter exposure (0.5 s total sample exposure) and penetrates 40 % of the plate barrier. The two pores in c) were both drilled for 0.3 s, in comparison to the 0.25 s pores shown in in Figure 5.10d) they are much narrower, despite penetrating the same depth. These results help reaffirm that the chopper is interrupting a cumulative effect.

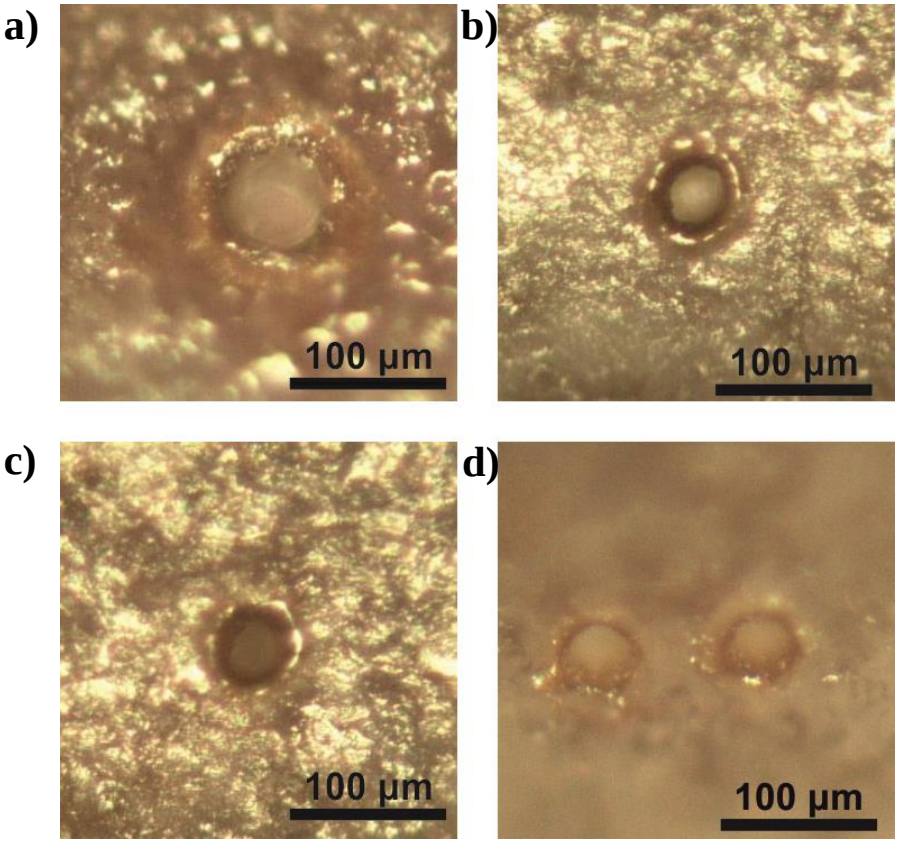

Figure 5.13: Optical images of pores created with a single slit chopper, using an average power of 360 mW with a 20 Hz chopper frequency. Exposure times of 2,1,1 and 0.3 s were used in a) to d) respectively. Laser A used (repletion rate = 20 MHz, pulse length = 300 fs).

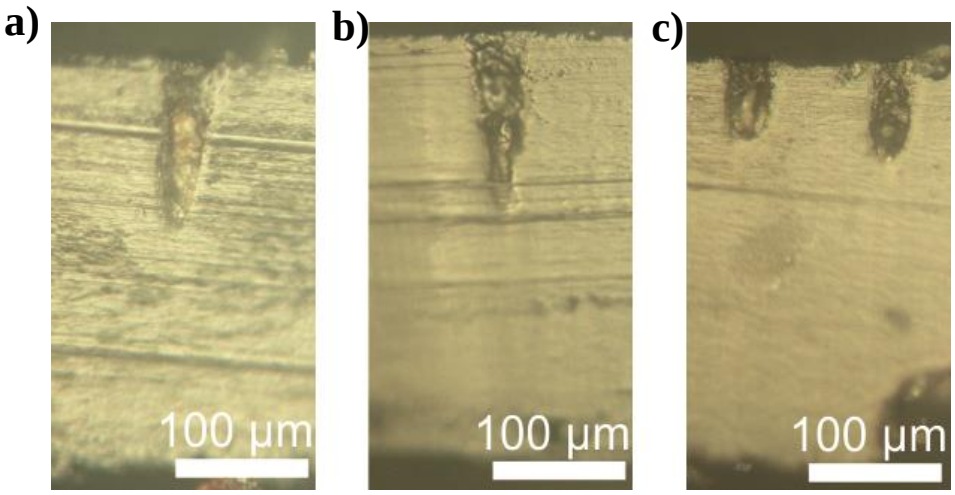

Figure 5.14: Optical images of cross-sections showing pores drilled into a nail plate with 360 mW power with a 20 Hz chopper frequency. Exposure times of 1, 0.5 and 0.3 s were used in a) to c) respectively. Laser A used (repletion rate = 20 MHz, pulse length = 300 fs).

5.5 Summary

The suitability of fibre delivered femtosecond pulsed visible laser radiation for poration of the human nail plate has been demonstrated. When unstained nail samples were exposed to the beam the surface was burnt, and no tissue was removed. The use of a dye to stain the nail before optical drilling was required, as visible light is poorly absorbed by the nail. Staining the nail provided a 'kick-start' to the ablation process, since energy was confined into a small focal volume. Four dyes were tested and Ruthenium Red was selected as the best due to its high absorption at 532 nm, the low level of interference with the normal nail Raman signal, ease of application and the relative tidiness of pores that were created in samples stained with it.

Pores were drilled with a variety of exposure times and average laser powers, in order to obtain the parameters that produced 'optimal pores', with minimal burning in their surroundings. An optical chopper provided breaks to the pulse train in which excess thermal energy could dissipate. Increasing the frequency of rotation did not seem to affect the level of thermal damage. For a specific power, increasing the exposure time, and hence the number of pulses, meant the removal of more material. A custom chopper blade was used with a $1/10^{th}$ window, and this showed a further reduction in the surrounding damage. However, it took nearly 20 seconds to porate mid-way through the plate, with powers larger than those that fully porated the plate with the standard chopper. Hence it was concluded that the chopper interrupted a cumulative effect during poration, which will be further addressed in Chapter 6.

There is variability in the geometry of the pores created when parameters are kept fixed, which is expected given the inhomogeneous nature of the nail plate, as revealed in Chapter 4. Also, an additional problem arose from maintaining fibre tip-surface distance. Even though the fibre was fixed on a micrometer-stage, which could be positioned along three axes, the curvature of the nail meant the tip would often be non-perpendicular to the surface, resulting in pores with an oval shape.

Seeing the results obtained in this chapter, a series of regimens to be used for the poration of nail samples were established for the permeation experiments in Chapter 7. These regimens are given in Table 5.1 and were decided upon from study of the quality of the pores, and their potential to drill to different thicknesses of the plate. The 1:1 ratio chopper at a frequency of 20 Hz was used for every regimen except #1. It was decided that the drilling of an array of pores with the 1/10th chopper would require an unacceptable length of time and so this was not used.

Table 5.1: Parameters for laser regimens to be used for permeation experiments

Regimen #	**#1 ***	**#2**	**#3**	**#4**	**#5**	**#6**	**#7**
Power (W)	1	1.3	0.5	1.3	1	0.5	0.25
Exposure time (s)	0.25	0.063	0.125	0.033	0.033	0.063	0.125
Energy per pore (J)	0.25	0.082	0.063	0.043	0.033	0.031	0.031

*Regimen 1 is the only unchopped regimen, all others use a chopper at 20 Hz

Chapter 6

Raman Mapping of Thermal Damage

6.1 Introduction

Laser ablation of the nail could be used (in conjunction with pharmaceutical products) to improve treatment of fungal nail infection. However, there is no current quantitative technique to evaluate thermal damage caused to the nail, either by poration or other heat treatments. It is important to assess burning of the nail during poration because coagulation of tissue around the pore may reduce subsequent drug diffusion. Although optical microscopy can be used to assess the thermal damage, the information obtained by this method is usually incomplete (e.g mild thermal damage that may cause no visible change in the nail). In some instances visually detecting burnt tissue has been challenging where the tissue was stained [114]. Thus development of a quantitative technique to measure thermal damage is highly desirable. Such a method would also facilitate comparison of the performances of different laser-poration systems.

Raman spectroscopy is one technique that could be employed for this purpose. As described in Chapter 4 biological materials exhibit a broad, featureless, background signal over the entire spectral range of most spectrophotometers (400 - 4000 cm^{-1}). This is usually attributed to fluorescence [87-89], although sample morphology can also be a contributing factor [90,91]. Physical changes to biological tissue, such as those caused by heating, change this background signal appreciably; for example, the signal intensity of skin heated above 100°C increases significantly [74], an observation attributed to denaturation of cellular proteins and collagen [115,116].

This chapter presents the development of a technique to measure the extent of thermal damage to the nail caused by laser ablation. Initially, nails were heat treated by placing them on a hot metal plate maintained at a specific temperature. Raman spectroscopy of the heat-treated nails shows a strong background scattering, the intensity of which increases with the heat-treatment temperature. Hence this signal can be used for quantifying the degree of thermal damage caused to the nail during poration. All poration in this chapter was performed using laser B. The Raman microscope is capable of acquiring a two-dimensional map of a sample, recording the spectrum corresponding to each pixel. Using this mapping technique and the empirical relationship between the intensity of the background signal and the temperature allows the production of high-resolution two- and three-dimensional "thermal" maps for the areas surrounding the pore. From these maps a better understanding of the mechanism of ablation was gained; it was shown that although the majority of the pore is drilled by plasma-driven ablation, photothermal processes are responsible for removing material at the pore edges.

6.2 Raman Spectroscopy of Heated Nails

Nail samples for these studies were heated on the hot brass block located inside a furnace (See Section 3.1.3). The temperature of the block surface was monitored with two thermocouples, with eight different temperatures and five contact times used for heat treatment of the nail samples.

After exposure, Raman spectra were acquired from four different locations on each sample. Figure 6.1a) shows the Raman spectra of nail samples from a single donor, after a 4-minute heat treatment, as a function of the heat-treatment temperature. The intensity of the detected signal rapidly increases with temperature over the whole spectral range. As is typical for a strong background signal, no distinct spectral features are observed and this means that the Raman intensity data can be correlated with the temperature to which the nail was exposed. Instead, we averaged intensity over the range of 700-1700 cm^{-1} and used this value, referred to as the Characteristic Raman Intensity (CRI), to quantify the response at each temperature (T). Figure 6.1b) shows that CRI values are essentially independent of the time of heat treatment, the initial rise between 1 and 2 minutes being most probably associated with the nail thermally equilibrating with the furnace temperature.

Figure 6.1c) is a plot of the logarithm of the normalised CRI dependence on heat treatment temperature. The normalised data were obtained as follows. First, using nail samples from each of the three donors, Raman spectra were acquired as a function of temperature. The CRI of each sample, at each temperature, was then determined (in the range 700-1700 cm^{-1}). The CRI was then normalised, for each sample, by the corresponding value at room temperature ($I(T_0)$). The averages (± SD) were determined and the results plotted. The results indicate that heat treatment at temperatures below 90˚C did not have any significant effect on the normalised CRI. However, above 120˚C, CRI increased rapidly, reaching values that were 1000-fold higher at 210˚C than those at room temperature.

The sharp increment between 120 and 160˚C can be attributable to the melting of crystalline α-keratin (reportedly at 142˚C), the structural and chemical disruption of which results in a strong uplift of the background signal [117,118]. Samples heated to 160˚C and above showed visible darkening and their surfaces were roughened.

The experimental data in Figure 6.1c) were modelled with the following empirical relation:

$$\log\left[\frac{I(T)}{I(T_0)}\right] = \alpha \cdot \exp[\beta \cdot T], \qquad (6.1)$$

where $\alpha = 0.031$ and $ß = 0.0217\ ^{o}C^{-1}$ are fitting constants, $I(T)$ is the temperature dependent intensity of Raman response (CRI) at the nail surface and $I(T_0)$ is the corresponding value at room temperature ($T_0 = 20^{o}C$). It follows that this equation can be used to estimate, from the Raman-assessed CRI post-treatment, the temperature achieved in a nail sample when exposed to laser irradiation, and to quantify any thermal damage to the surrounding tissue following a poration event.

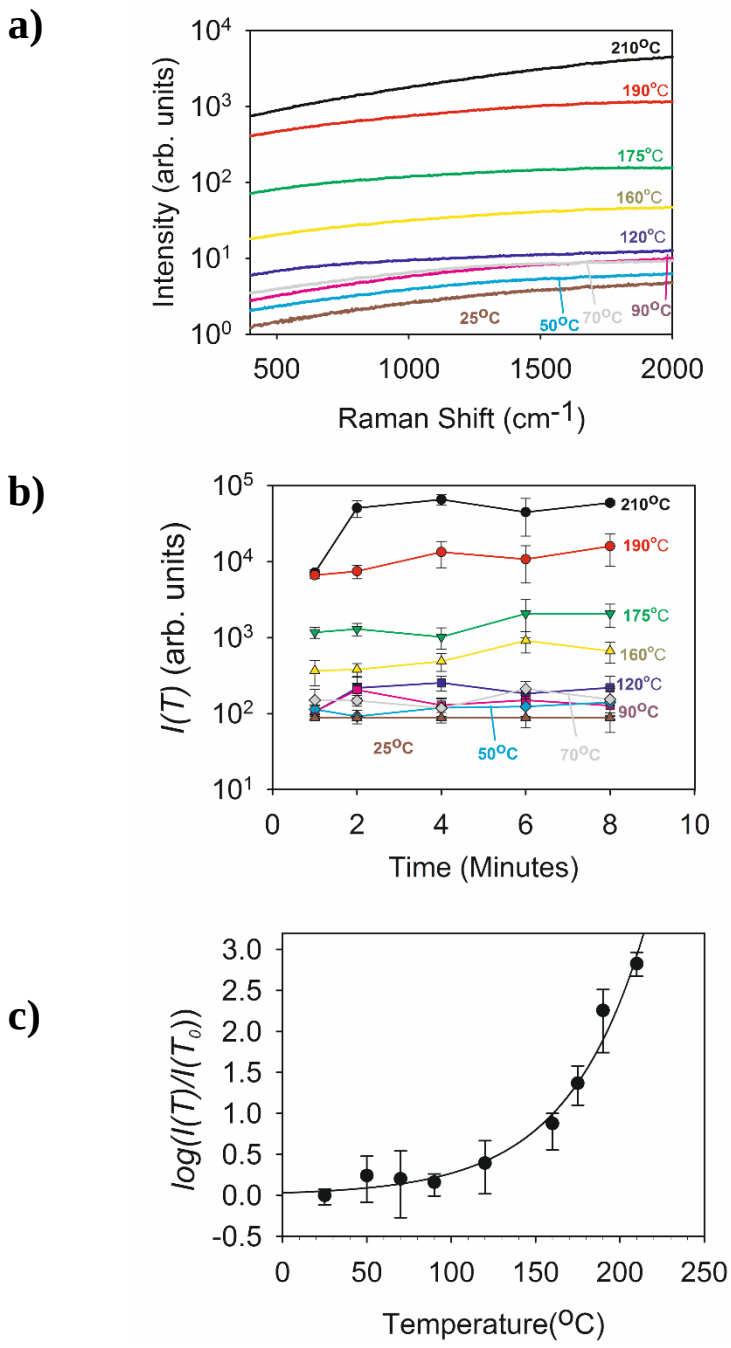

Figure 6.1: *a) Representative Raman spectra recorded from a nail sample after heating for 4 minutes as a function of temperature (recorded with 532 nm laser). b) Integrated Raman intensity measured from nail samples after heat treatment as functions of temperature and time. Data points represent the mean ± SD values of 4 spectra from each of three nail samples from different donors. c) Normalised integrated Raman intensity as a function of temperature. Data points again represent the mean ± SD values of 4 spectra from each of three nail samples from different donors. The empirical curve fitted to the data is given by Eq. 1.*

6.3 Quantification of Thermal Damage Surrounding Laser Drilled Pores

The establishment of the empirical relation between the intensity of Raman response and the temperature to which nails were exposed, made it possible to measure local CRI values from any region surrounding a pore and deduce the corresponding local temperatures. Figure 6.2a) shows an example of a pore created with regimen #2 (see Table 5.1) on a nail sample from volunteer B. Figure 6.2b) shows deduced temperature profiles (from the measured CRI values and Equation 1) in the vicinity of four pores created with regimens #1 and #2. In each case, Raman spectra were taken at increments of 10 μm from the pore edge. To find a 'room temperature' vale (i.e an undamaged region), measurements were recorded several millimetres away from any pore. Regimen 1 caused noticeably more thermal damage than regimen 2. In the former, the temperature reached 170°C at the pore edge, decreasing to below 80°C at a distance of 120-130 μm; in contrast, for the latter, the temperature at the pore edge was 135-155°C, falling to below 80°C at 30-50 μm.

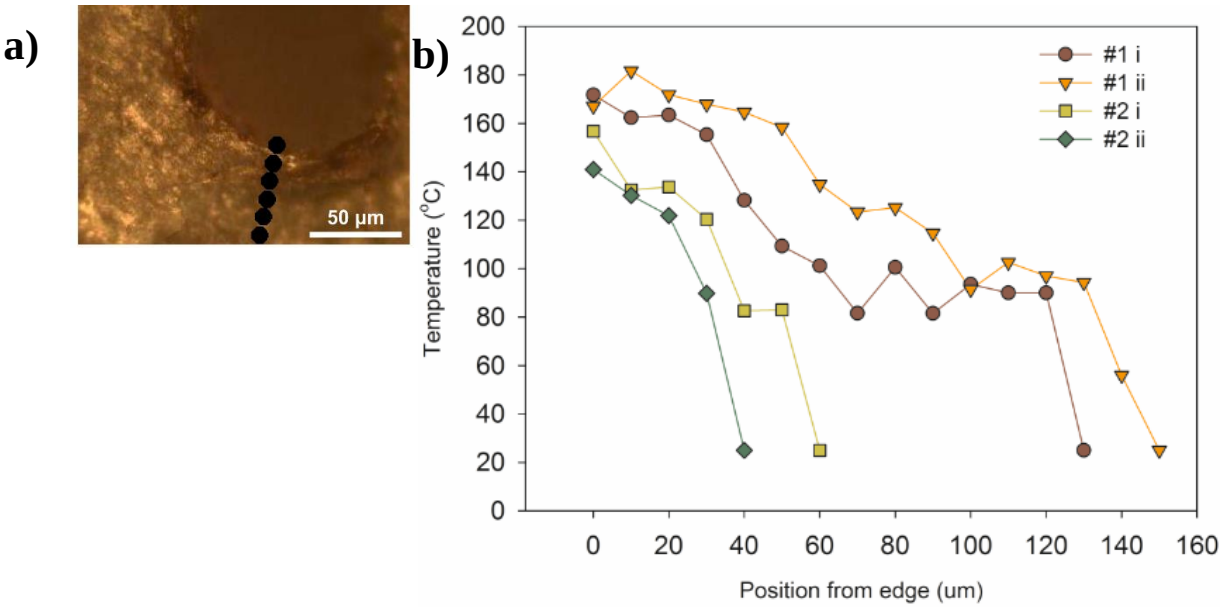

Figure 6.2: a) Optical image of a pore created with regimen #2, and markers showing where Raman measurements were taken. Note the first point on any sample was discarded if inside the edge as it was out of focus, and a far lower Raman signal would be collected b) Deduced temperature profiles (from the measured CRI values and Equation 1) in the vicinity of 4 pores created with regimens #1 and #2. The pore labelled #2 ii corresponds to the image in panel a). The room temperature point on each graph is the first point that reached a CRI value equal to the values recorded on the same nail in a region at least 2 mm away from a pore.

6.3.1 Dealing with Cross-sectional Variance in the Nail Plate

Deducing the temperature surrounding pores in cross-sections was key to provide more information for determination of the poration mechanism. Figure 6.3a) displays an optical cross-sectional image of a pore that was produced with regimen #5. Raman spectra were then recorded for an array of over the pore cross-section (85 x 24 points). For each point the corresponding CRI value was calculated to create the CRI map, which is shown Figure 6.3b) overlaying the optical image from Figure 6.3a). Here the CRI response is colour coded with the greatest CRI values represented by the darkest colours.

It is not a trivial problem to convert the measured CRI values into temperature, because as demonstrated in Chapter 4, the CRI background signal varies across the nail thickness, reaching maximal values at the nail surfaces (see Figure 4.15b)). This intrinsic variation

in the CRI values across the nail thickness should be taken into account before calculating the temperature. Therefore, Equation 1 has to be altered.

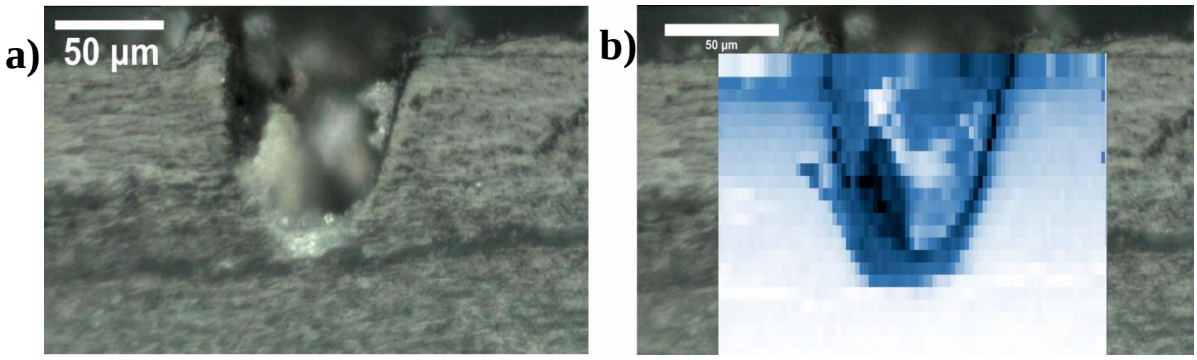

Figure 6.3: a) Optical cross-sectional image of a partially porated nail sample drilled with regimen 5. b) The image in panel a) with a superimposed Raman map where deeper shades of blue reflect higher CRI values.

To understand how Equation 1 has to be modified, it is necessary to establish whether the two sources of variation in the Raman background intensity, i.e. depth- and temperature-dependent, are correlated. Figure 6.4 displays the maximum Characteristic Raman Intensity, $I_{max}(T, Z)$, that corresponds to the pore's right edge, as a function of depth Z for each row of the map in Figure 6.3b) and the CRI for the background signal, $I(T_0, Z)$, calculated from an average of four points at the furthest edges from the pore. From this it is clear that there is no correlation between temperature-induced and depth-related effects.

It is also useful to analyse the behaviour of the Raman background signal, $I(T, Z)$, across the porated sample at different depths. Figure 6.5a), shows three examples, corresponding to the depth of 5, 25 and 150 µm into the nail for the Raman map presented in Figure 6.3b). The maximum intensities corresponding to the pore edges are the same at both 5 and 25 µm into the nail; in contrast, the intensity from undamaged nail deeper into the sample, $I(T_0, Z)$, is significantly lower. However, when the three profiles at different depths are corrected for the corresponding intensities from undamaged regions of the nail (i.e. $I(T, Z)-I(T_0, Z)$), a consistent pattern of behaviour is observed (Figure 6.5b).

It follows that the Raman intensities measured in a porated nail can be represented as

$$I(T, Z) = I_T(T) + I_Z(Z) \tag{6.2}$$

where the first term of the sum, $I_T(T) = I(T, 0)$, depends only on temperature, while the second, $I_Z(Z) = I(T_0, Z)$, only on depth.

To generalise Eq. 6.1 for the case of cross-sectional maps, where the Raman response depends not only on temperature but on depth also, Eq. 6.2 should be taken into account. As all measurements for establishing Eq. 6.1 were performed on the top surface of nails (Z=0), the parameters introduced for Eq. 6.1 can be expressed as

$$I(T) = I(T,0) = I_T(T) + I_z(o) \tag{6.3a}$$

$$I(T_0) = I(T_0,0) = I_T(T_0) + I_z(0) = I_z(0) \tag{6.3b}$$

In Equation 6.3b, $I_T(T_0)$= 0, because no thermally induced effect are expected at room temperature and the measured signal can be attributed to $I_Z(0)$. Therefore the ratio $I(T)/I(T_0)$ can be written as

$$\frac{I(T,0)}{I(T_0,0)} = \frac{I(T,Z) - I_z(Z) + I_z(0)}{I_z(0)} \tag{6.4}$$

Thus, Eq. 1 can be generalised as

$$Log\left[\frac{I(T,Z)-I_z(Z)}{I_Z(0)} + 1\right] = \alpha \cdot \exp[\beta \cdot T] \tag{6.5}$$

Here $I_Z(Z)$ is the intensity of Raman response (CRI) as a function of depth for thermally undamaged areas, with $I_Z(0)$ corresponding to the value of this function on the nail surface, and $I(T, Z)$ is CRI for the area that was exposed to thermal damage at temperature T.

Figure 6.5c) displays a temperature map that was obtained using Equation. 5 to convert CRI signal, $I(T, Z)$, from the Raman map presented in Figure 6.3b) into corresponding temperature. As can be seen, during laser poration the effective local temperature to which the nail was exposed drops quickly from the pore edge.

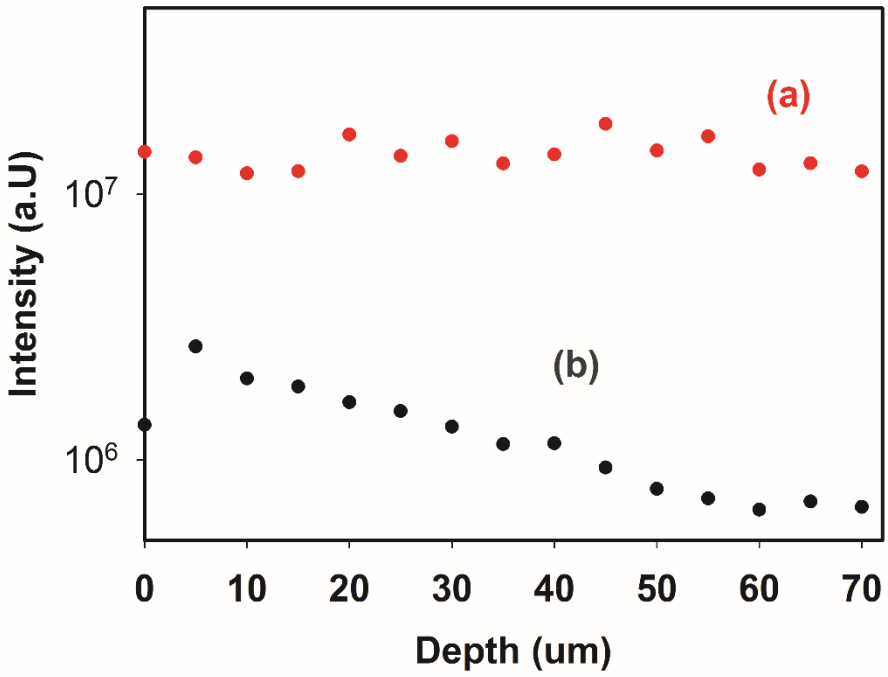

Figure 6.4: Raman integrated background intensities as a function of depth for the pore in Figure 6.3b); a) for the points of maximum thermal damage at the right edge of the pore, b) for undamaged areas in the far right part of the Raman map.

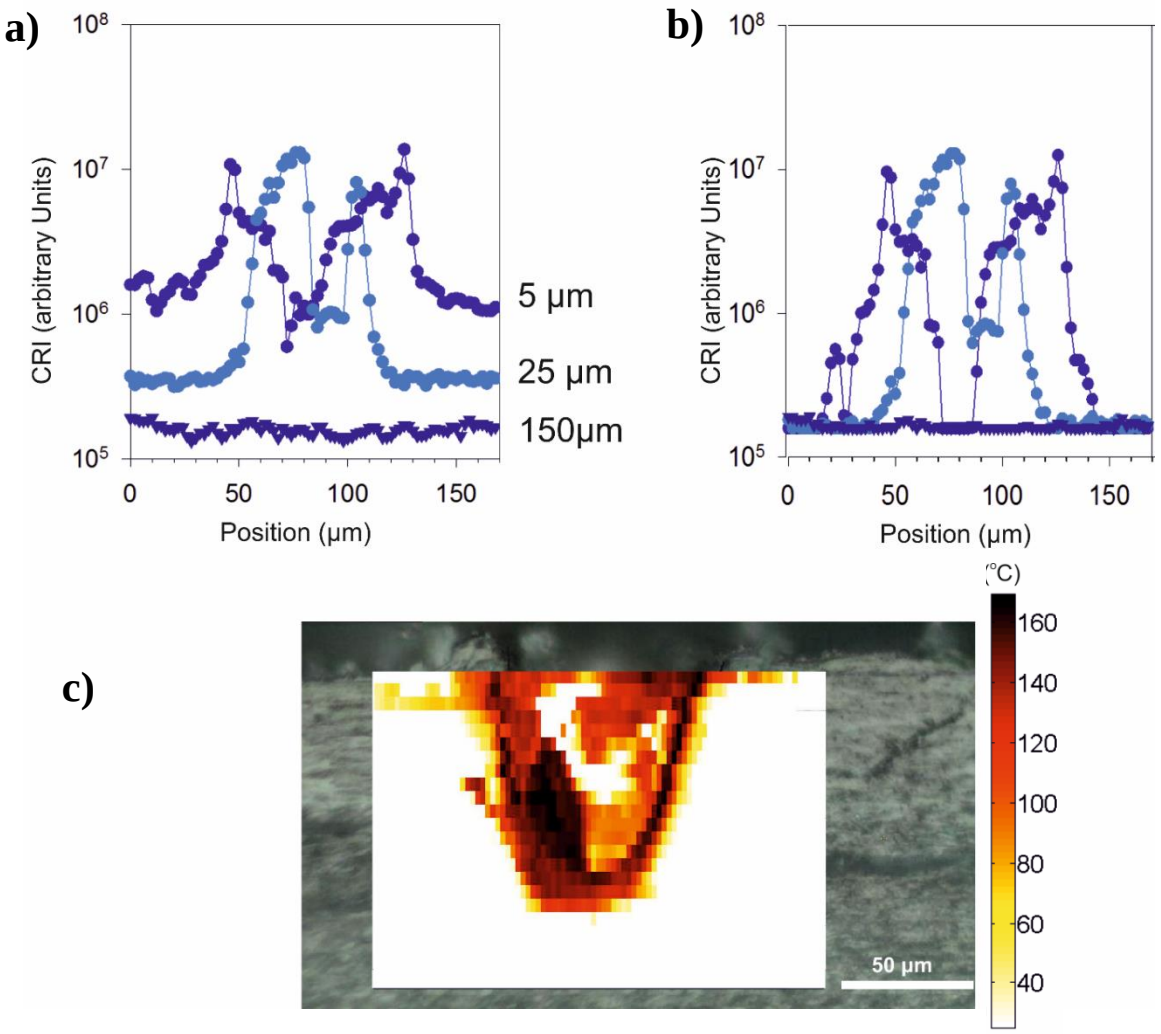

Figure 6.5: a) Measured CRI values across the porated sample shown in Figure 6.5 at depths of 5, 25 and 150 μm into the nail. b) The three profiles in panel a) corrected for the corresponding intensities from undamaged regions of the nail. c) Raman intensity data in Figure 6.5b) converted into a temperature map of thermal damage around the pore using Equation 6.5.

6.3.2 Temperature Maps and the Ablation Mechanism

Figure 6 shows cross-sectional optical images and temperature maps for three pores of different depth. For the fully porated sample in Figure 6.6d), the thermal damage extends approximately 250 μm across the nail. The maximum temperatures achieved in the nail reach about 160°C, with relatively small variability for different depths. For the partially porated samples, the thermal damage decreases with increasing depth into the pore, and

the maximum temperatures attained become smaller. For example, the data in Figure 6.6e), corresponding to the pore in Figure 6.6b), shows that thermal damage extends approximately 22 μm at the exterior surface of the nail falling to less than 10 μm at the base of the pore; the corresponding values, displayed in Figure 6.6f), for the shallower pore, in Figure 6c) are 20 μm and 6 μm, respectively. Raman spectra taken from the nail below the bottom of the partially-porated pores were indistinguishable from intact, untreated nails within distances of 6 and 2 μm, suggesting the rapid attenuation of energy penetration.

Using the surface plot in MATLAB, in combination with the contour plot function, three-dimensional temperature maps were generated as shown in Figure 6.7. Contours are located starting at 25^{o}C and placed every 25^{o}C after that. Raman data from the centre of the pore (i.e., between the edges) cannot be interpreted with confidence because here the microscope was out of focus. This would generally result in a lower CRI being collected, and when converted give a lower temperature. The three-dimensional maps display this as a dip in the central area of the pores.

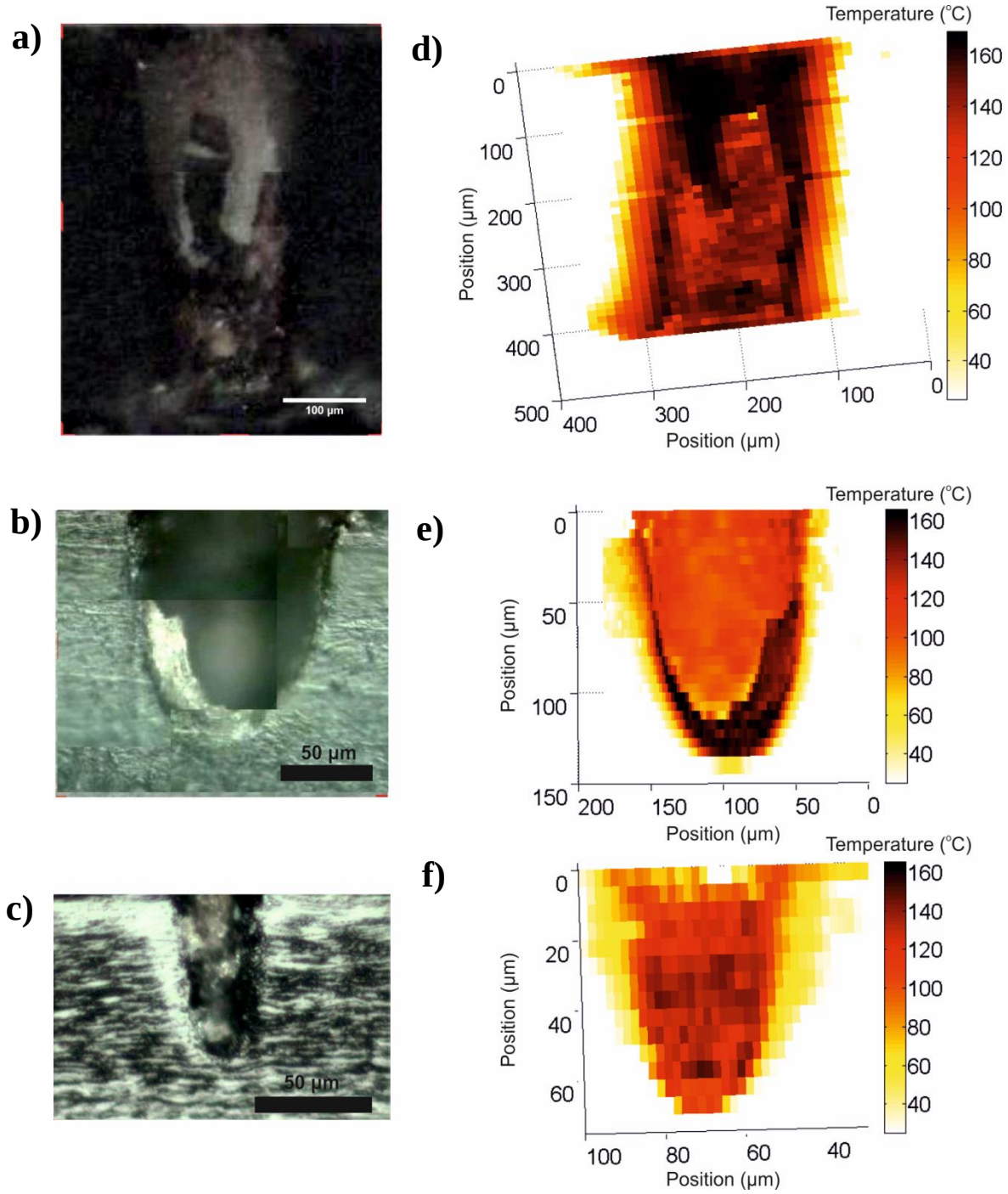

Figure 6.6: Panels a), b) and c) are optical images of pores created by regimens #1, #3 and #7, respectively. The corresponding temperature Raman maps are in panels d), e) and f) providing a quantitative description of the thermal damage surrounding the pores.

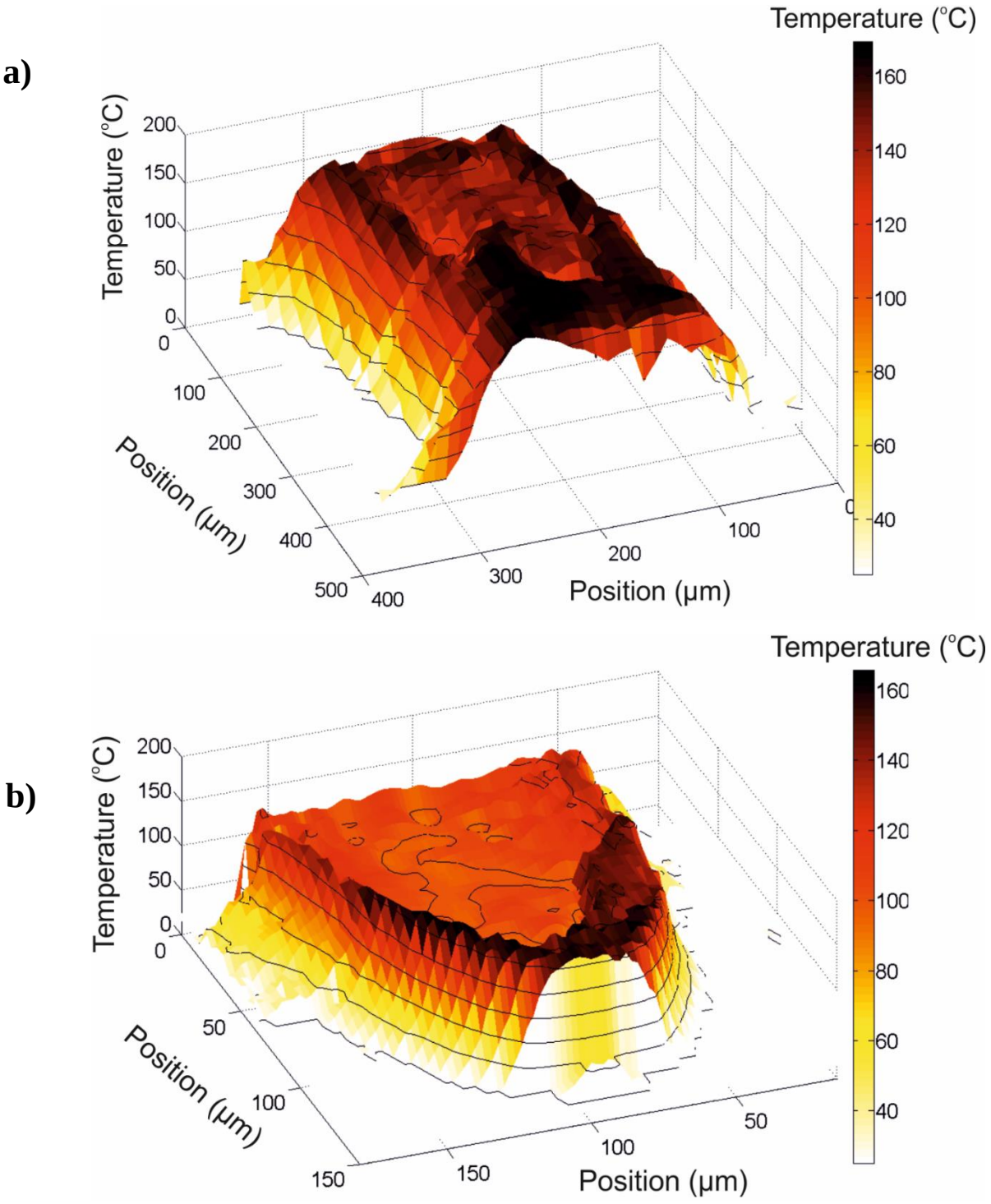

Figure 6.7: Three-dimensional maps showing the temperature variations across the pores shown in Figure 6.6. a),b) and c) were drilled with regimens #1, #3 and #7.

c)

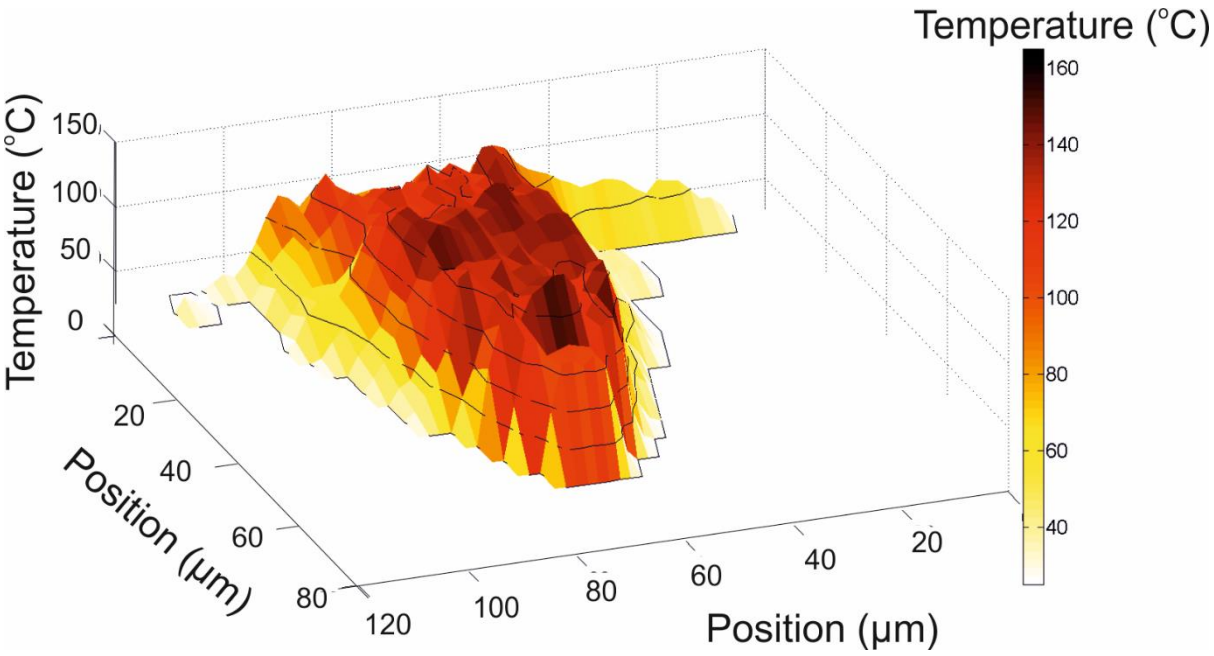

Figure 6.8: Three-dimensional maps showing the temperature variations across the pores shown in Figure 6.6. a),b) and c) were drilled with regimens #1, #3 and #7.

The laser poration process and the thermal damage provoked in the region surrounding the pores can be interpreted from the results in Figures 6.6 and 6.7. Laser radiation is initially absorbed by the dye on the surface of the nail, confining the energy to a small volume of tissue. When a critical electron density is reached, a plasma is created and material is ejected from the sample. As the poration continues, the central region of the base of the pore is always exposed to the highest intensity in the Gaussian-shaped beam, and material is continually removed by plasma ablation. However, the Raman maps suggest that a thermal process is causing, or at least contributing to, the removal of material at the pore edges. Laser energy also travels into the tissue adjacent to the pore edge causing an increase in the measured Raman spectral intensity (CRI). Around the pore drilled with regimen #7, the increased temperature in the tissue indicates that energy has been transferred, but has not been sufficient (in terms of power and exposure time) for tissue removal by a photothermal process. In contrast, the pore created with regimen #3 is noticeably wider and larger than expected given the diameter of the fibre.

Considering, in order, the three pores shown in Figures 6.6a), 6.6b), and 6.6c) as a time-lapse leading to the creation of a fully-porated nail, the low level of thermal heating seen

around the pore in Figure 6.6f) may be viewed as the starting point for photothermal ablation. Continued irradiation of this nail would have led to a further increase in temperature, causing ejection of material and widening the pore to its maximum width; the latter, of course, depends on the distance between the fibre and the nail surface and on the numerical aperture of the fibre.

Plasma-mediated ablation occurs at the base of the pore, with the energy confined to the volume of material that is ejected, and this explains the minimal thermal damage seen below the pores. Eventually, plasma ablation porates all the way through the nail barrier, and photothermal ablation may keep widening the pore. The increasing ratio of thermal damage to pore width, with increasing depth into the fully porated nail is caused by two physical processes: (a) the beam waist increases with axial distance, and (b) more light is scattered in the tissue as the beam travels deeper. Both processes contribute to a lower energy density, insufficient for ablation, but large enough to cause thermal damage to the remaining tissue.

As shown in Chapter 5 using a beam chopper reduces thermal damage to the region surrounding the pore. This effect clearly manifests itself on thermal maps and can be described quantitatively. Figure 6.8a) shows the thermal damage surrounding 4 pores, measured radially from the pore edge at a depth of 40 μm. In terms of the fully porated samples, regimen #1 has thermal damage out to 70 μm from the pore edge, and this was reduced to 44 μm for regimen #2 when the beam chopper was used. The two partially porated samples (regimens #3 and #7) have thermal damage extending to 28 and 18 μm, respectively. It follows that confining the energy in a small volume of material is key to efficient ablation. The schematic in Figure 6.8b) illustrates the effect of a long train of laser pulses causing an increase in temperature, and if the energy in the specific volume does not reach a critical density, then permanent thermal damage will result. The use of a chopper to modify the pulse frequency provides breaks in the train and allows the sample to cool down, preventing tissue coagulation and allowing better control over thermal damage around the pore.

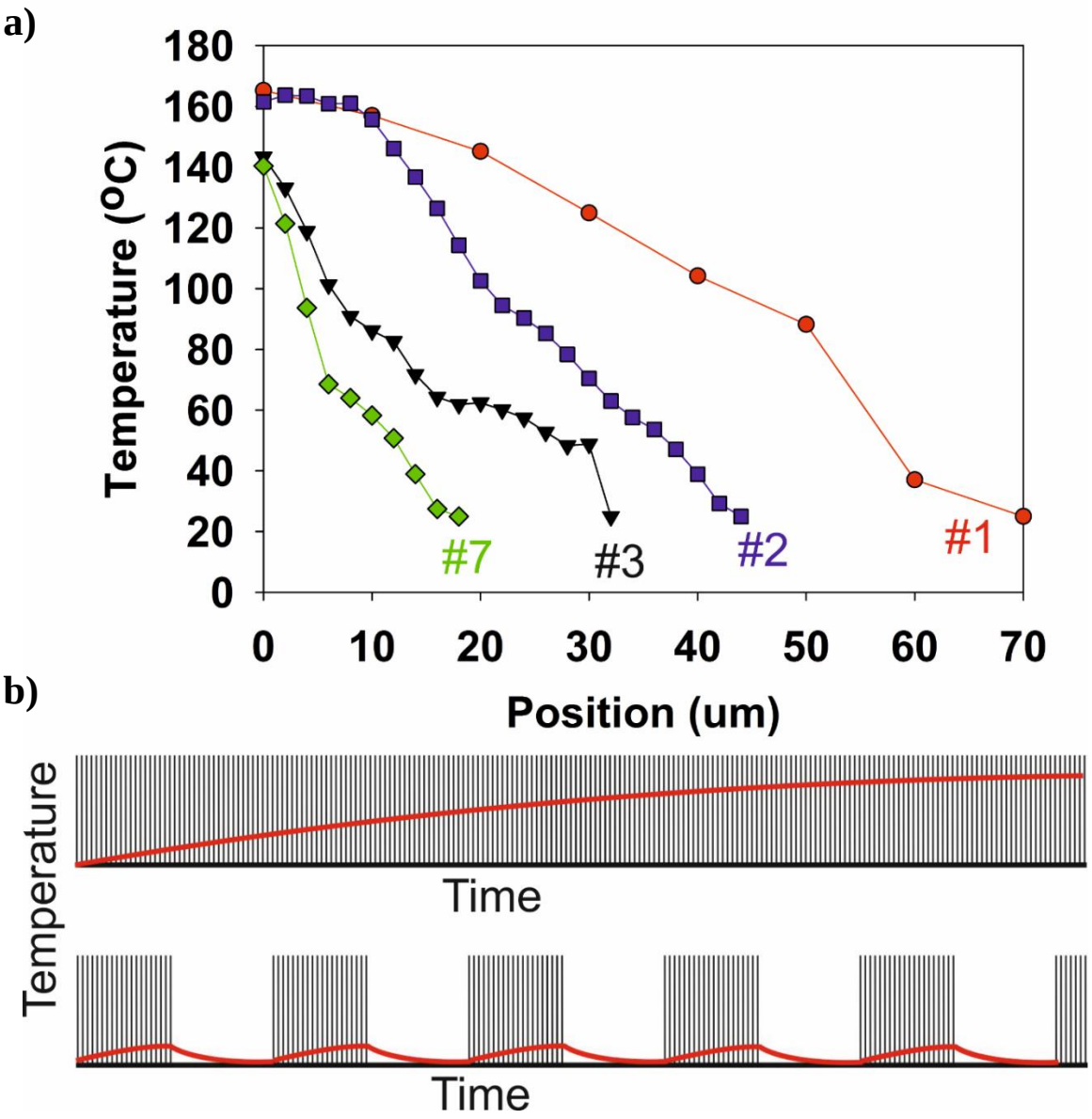

Figure 6.9: a) The region of damage surrounding 4 pores porated with regimens #1, #2,#3,#7 is displayed for a depth of 40 μm. b) Pulse train for unchopped (top) and chopped (bottom) beams, the red line illustrates a temperature rise in the surrounding tissue.

As shown in Chapter 5, it was necessary to stain the nail before optical drilling because unstained nail has poor absorption at the laser wavelength, resulting in insufficient energy to initiate tissue removal. However, an interesting problem comes about when it is considered that only the surface is stained, yet complete poration of the nail plate was achieved by fractional ablation. This is despite the fact that the tissue lying beneath the surface is effectively 'unstained'. It is possible some of the vaporized dye 'falls' back onto the surface of the bordering volume of nail, facilitating removal of the next layer. There is some support for this as the fibre tip was darkened by ejected material. However, as the dye is ejected evenly in all directions, its quantity in the pore will quickly be reduced after several expulsions. This would reduce light absorption, and stop drilling after a short distance.

This is clearly not the case for the drilling of pores with this technique, a factor other than the dye must aid complete poration of the plate. Figure 6.9 displays scanning electron micrographs of the interior of several pores ablated with regimen #7. Visually, the tissue has been severely altered on the immediate interior of the pore; this corresponds to the area immediately bordering the pore edge, in which the highest temperatures were reached in Figures 6.6 & 6.7. Clearly, the data show that the optical properties of the nail tissue in the vicinity of the pore edges has been modified in the process of drilling.

The formation of plasma is confined to a small area, but, free electrons interact with the regions immediately bordering and collide with molecules, which results in heating [118]. In addition, mechanical stress can be exerted on the material surrounding the plasma formation, as a result of the conservation of momentum. Tensile stress waves may produce fracture of material even when a temperature rise is too small to exert thermal damage [119]. Thermal effects were minimal beneath the base of the pores, and so it is possible stress generation also contributed at the immediate centre of drilling. Regardless of the process modification of the base of the pore results in increased susceptibility to absorption, in comparison to intact nail. This self-seeding process allows drilling, via plasma-mediated ablation, through the entire nail, long after all of the ink from the ablation zone has been removed.

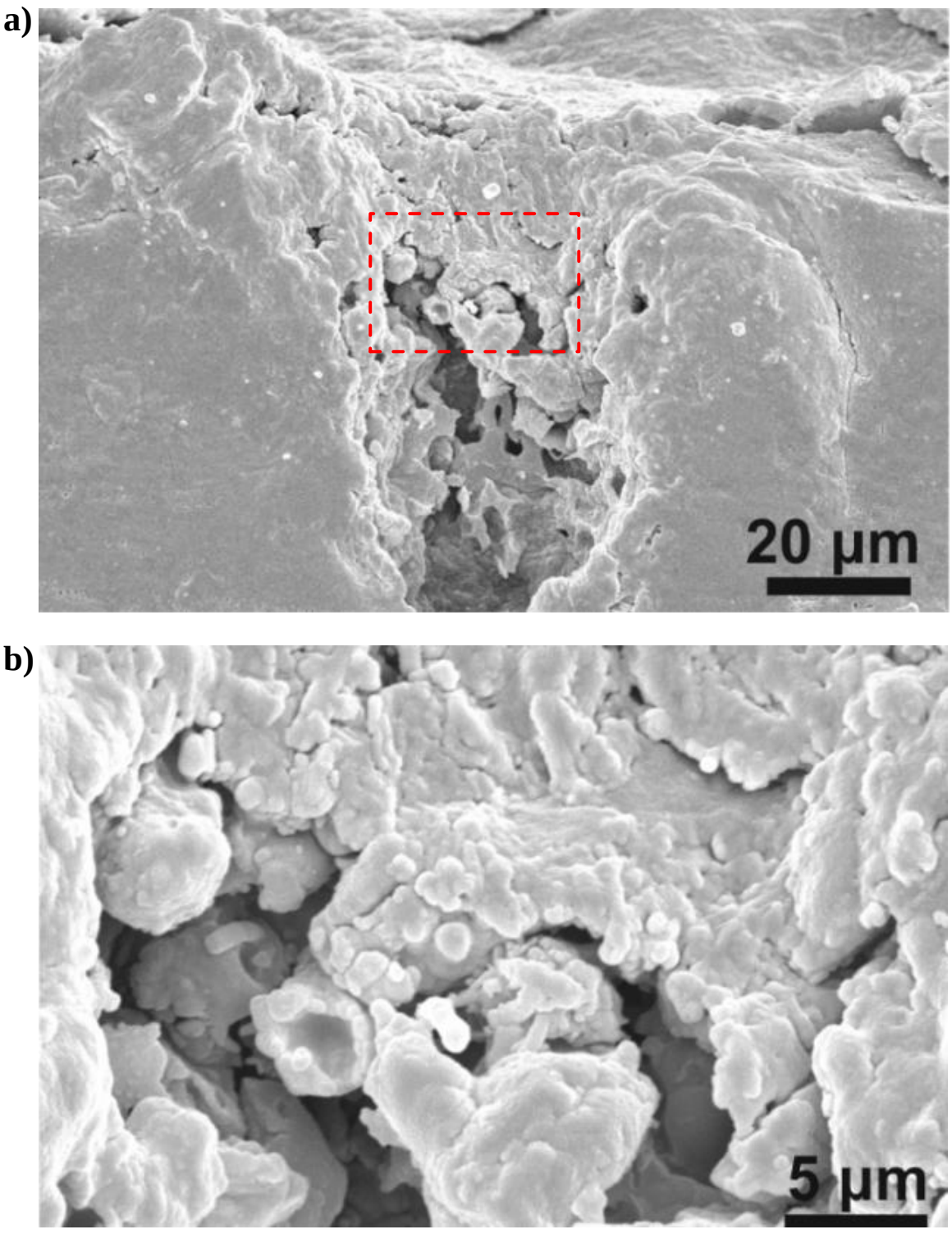

Figure 6.10: Scanning electron micrographs detailing pores created with regimen #7; a) overview of a cross section through a pore, the structure inside is drastically altered from the structure for the regions at the edge of the image where no change was detected in the Raman signal. b) Higher magnification capture from inside the red box in a), displaying the drastic alteration to the structure.

6.4 Conclusion

The manner in which light is absorbed or scattered within the sample hugely impacts ablation efficiency. Light's interaction with a sample is influenced by the composition and morphology of the tissue; the key determinant for poration is the ratio of optical absorption relative to optical scattering. If this can be maximised in favour of absorption, efficient ablation of tissue will occur, with minimal thermal damage caused to the area surrounding the pore.

Raman microspectroscopy was employed as a quantitative tool to assess thermal damage to the nail induced by laser poration. An empirical relation was established to correlate the integrated Raman intensity with the increased temperature produced in the nail by exposure to the laser radiation. The high resolution of the Raman microscope permitted detailed maps of thermal damage to be determined and facilitated understanding of the poration mechanism. Although nail does not absorb visible light strongly the use of ink provided a volume with high absorption in which to confine the radiation and initiate ablation. It was deduced that plasma-driven ablation occurred through the centre of the pore. In contrast, photothermal processes were responsible for removal of material (and the local damage) at the edges of the pore. Detected damage propagated only a few μm beneath the base of the pore, but it was proposed that in these few μm an alteration that facilitated absorption of radiation occurred to the tissue. The low transfer of energy into the region below the partial pores may eliminate experienced pain, previously reported in clinical setting by patients. The self-seeding process explains how the femtosecond pulsed, visible laser can porate the entire thickness of a nail plate.

Chapter 7

Permeation of a Model Drug Through Optically Drilled Nails

7.1 Introduction

Topical therapy of nail diseases suffers from very low (or even no) bioavailability primarily due to the extremely limited and very slow permeation of therapeutically useful compounds into and across the nail [120]. Furthermore, topical formulations often fail either to maintain the active agent in a molecularly diffusible form post-application (because of the rapid evaporative loss of solvent from the vehicle) and/or to ensure a decent period of substantivity on the nail surface to allow drug to partition efficiently into the nail [121].

No study has directly measured the permeation of drug in laser porated nail. However, a positive treatment effect was witnessed in nearly all patients in a study in which a topical cream was applied to porated nail [77]. Studies in which the transdermal delivery through porated skin has been measured have shown strong improvement in comparison to intact skin [74,109,110,122].

The work detailed in this chapter investigates the enhancement to permeation of caffeine through the nail plate following poration. The regimens established in Chapter 5 were used to create arrays of pores in the nail plate using laser B. It is shown that complete poration of the nail enhances permeation by 2 to 3 orders of magnitude relative to an untreated sample. Partial poration results in an increase in cumulative amount providing

a sufficient drilling depth is achieved. A discussion of the diffusion of caffeine through fully and partially porated nails is given, including possible lateral diffusion. Finally the potential of partial poration to provide modulation of barrier function that may prove useful as a minimally-invasive drug delivery strategy is discussed.

7.2 Preparation of Arrays for Permeation Experiments

Preparation of samples for permeation experiments required arrays to be drilled into the nail plates collected from three donors. Samples were stained by submersion in a Ruthenium Red solution for 15 minutes, then left to dry for 5 minutes before being placed into a PermeGear plastic adapter. Placement in the adapter ensured that the array was drilled entirely inside the 0.2cm^2 diffusion area of the adapter. Laser B (power 5 W, repetition rate 80 MHz) was used to drill the nail samples for permeation experiments. Each array drilled consisted of 100 pores, with a spacing of approximately 300 μm between pore edges. The fibre tip-surface distance could not be measured directly, as the adapter prevented the use of a top down microscope. Instead, the stage was adjusted so that the fibre was slowly brought into contact with the sample, shown by a small deflection of the fibre. Subsequently, the stage was retracted 200 μm. Creation of each array took approximately 1 hour, primarily due to the repositioning required between pores.

Each of the seven regimens selected in Chapter 5 was used to porate three nails, with one nail from each donor drilled. Optical images for six porated samples are shown in Figure 7.1. Regular removal of the sample was required to ensure all pores were drilled in the diffusion area, because of this it can be seen that the grids are not perfectly ordered. Variation in the diameter of pores is apparent from column to column in some arrays, especially where the nail curvature is greater, as for the nails in a) and e). As discussed in Chapters 5 & 6, maintaining a constant angle and distance between the tip and the surface was challenging.

Table 1 gives a full summary of the ablation regimens and pore characteristics. The pore diameters were measured with optical microscopy, whilst their depths were measured with LSCM as discussed in Chapter 5.3.2. Figure 7.2 displays a fully porated nail drilled with regimen #1 in a nail collected from donor b. The nail thicknesses were measured with a micrometer. The percentage of nail thickness removed and the percentage of the nail area at the surface, inside the 0.2 cm^2 region of the adapter are shown.

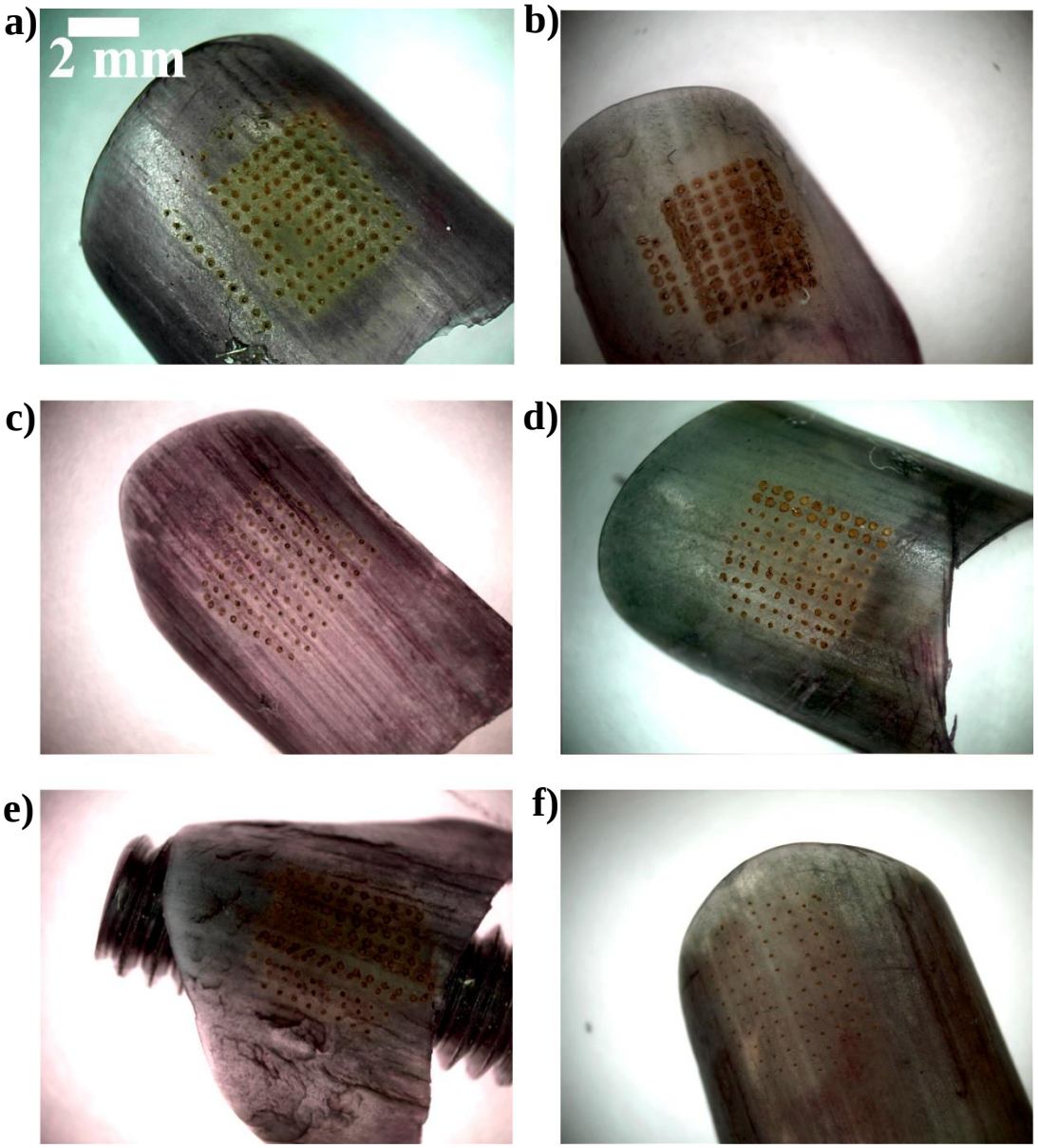

Figure 7.1: Arrays laser drilled in to the nail, with various parameters, consisting of 100 pores in a 0.2 cm^2 area. a) Regimen #1 donor b, b) Regimen #1 donor c, c)Regimen #2 donor a, d)Regimen #2 donor b, e)Regimen #5 donor b, f)Regimen #7 donor a.

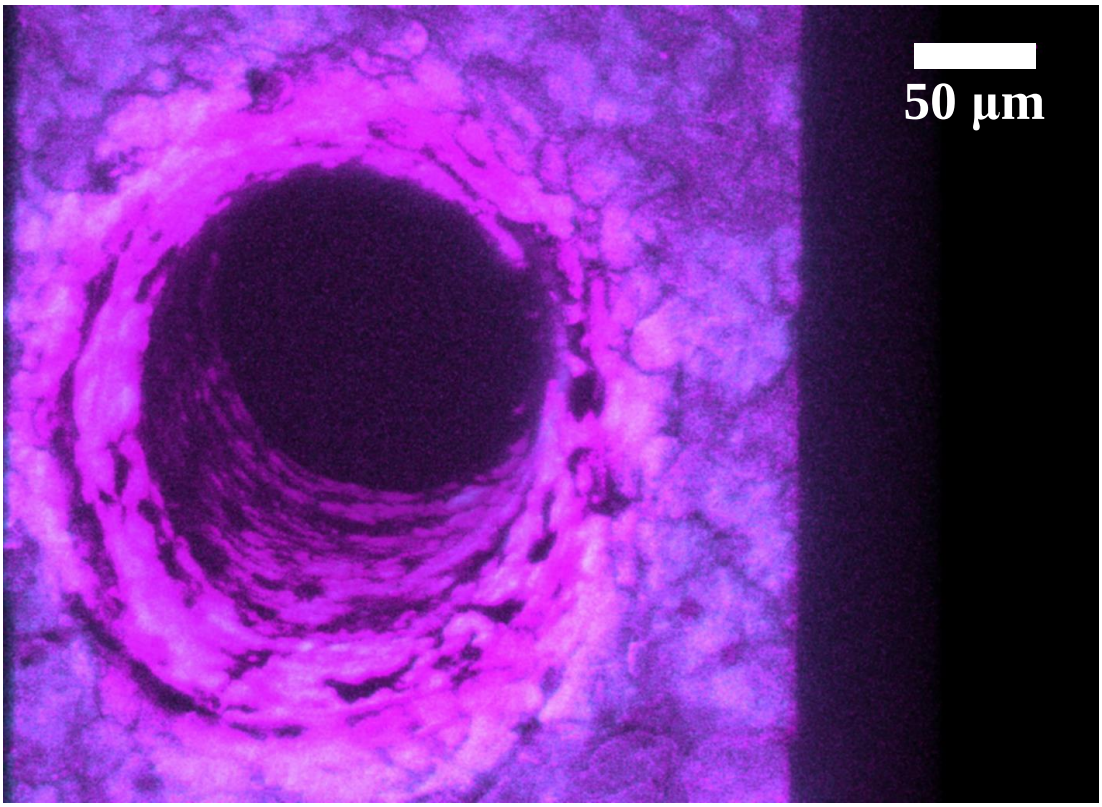

Figure 7.2: LSCM image of a pore drilled with regimen #1 that fully penetrates a nail plate collected from donor a.

Table 7.1: Ablation regimens and pore characteristics produced (mean ± S.D.; n=3).

Poration regimen	**#1**	**#2**	**#3**	**#4**	**#5**	**#6**	**#7**
Power (W)	1.0	1.3	0.5	1.3	1.0	0.5	0.25
Exposure time (s)	0.25	0.063	0.125	0.033	0.033	0.063	0.125
Energy per pore (J)	0.25	0.082	0.063	0.043	0.033	0.031	0.031
Pore diameter (µm)	146 ± 57	97 ± 20	80 ± 38	88 ± 28	70 ± 11	63 ± 27	45 ± 10
Pore depth (µm)	434 ± 52	320 ± 24	170 ± 63	118 ± 63	120 ± 48	115 ± 39	83 ± 20
Nail Thickness (µm)	315 ± 52	320 ± 24	340 ± 14	350 ± 5	365 ±42	335 ± 30	410 ± 65
% nail thickness porated	100	100	50 ± 16	33 ± 2	33 ± 4	34 ± 6	20 ± 4
% nail area at the surface porated inside 0.2 cm^2 adapter region	9.8 ± 7.1	3.8 ±0.5	2.7 ± 1.9	3.6 ± 1.2	2.0 ± 0.3	1.8 ± 1.0	0.8 ± 0.2

7.3 Caffeine Permeation

Caffeine permeation experiments were performed after arrays had been drilled in all 21 nail samples. To reduce the chance of the nail plate cracking, samples were rehydrated in deionised water for 30 minutes before being placed in the PermeGear diffusion adapter. Experiments were performed in side-by-side diffusion cells, with sampling performed at 0.25, 0.5, 0.75, 1, 2, 3, 6, 24, 48, 72 hours. A 1 ml sample was withdrawn from the receptor chamber and replaced with 1 ml of fresh phosphate buffered saline (PBS). The concentration of caffeine in these samples was measured with High Performance Liquid Chromatography (HPLC). Caffeine was separated from other components in the sample matrix through a HPLC column. Ultraviolet detection (λ=273 nm) gave a peak at 5.2 minutes. Drug concentration in the samples was calculated from peak area using, a calibration curve prepared from solutions of known drug concentration. The measured concentration values at these time points allowed the cumulative amount of caffeine permeated at each time point to be calculated (accounting for caffeine removed at each sampling time). The results for three of the samples were discounted due to leakage from the apparatus only apparent after ~1 hour.

Figure 7.3 displays cumulative caffeine permeated across the five fully porated nails (leakage occurred from one of the adapters). The second y-axis shows the percentage permeation of caffeine dose applied Comparison of the permeation of caffeine across intact and laser-porated nails revealed the dramatic potential impact of fully porating the nail plate. The cumulative penetration of caffeine across untreated nails amounts to less than 100 µg in 72 hours, consistent with that observed for similar small compounds reported in the literature [36]. In comparison, a very rapid permeation of caffeine is observed in fully porated samples with between 8-41 mg of caffeine permeating in 72 hours. In addition, the caffeine permeates very rapidly 32-56% of the final cumulative amount penetrated had already reached the receptor phase of the diffusion cell in 15 minutes. Self-evidently, this meant that substantial depletion of the donor solution had occurred and explains that subsequent measurements of further caffeine transport were considerably attenuated.

Figure 7.4 displays the cumulative amount for 6 nails from a single donor. Five are porated, with those drilled with regimen #1 and #2 fully porated. The data are shown on a double-logarithmic axis to emphasise the manner in which complete poration of the nail greatly enhances both the rate and extent of caffeine transport. The samples drilled with regimen #3 (~70% plate thickness drilled) and #7 (~40% plate thickness drilled) have caffeine permeation cumulative amounts reaching 210 and 650 μg respectively. Regimen #5 (~27% plate thickness drilled) reaches 45 μg, only 20 μg more than the control nail.

Figure 7.5 displays the average cumulative amount for all samples measured split into the four broad categories: (i) untreated controls (intact), (ii) porated between 15% and 40% of total thickness, (iii) porated between 40% and 70% of total thickness, and (iv) completely porated. When the nail was fully porated, the initial penetration rate of caffeine was on the order of 1000-fold faster than the control samples, and total delivery over 3 days was enhanced by more than 100 times. Partial poration to the extent of 40-70% of total nail thickness led to steady-state transport being achieved within 6 hours; the smallest level of poration (15-40% of total nail thickness) resulted in penetration profiles not dissimilar to those of the untreated controls, with constant fluxes attained approximately 24 hours after initiation of the experiment.

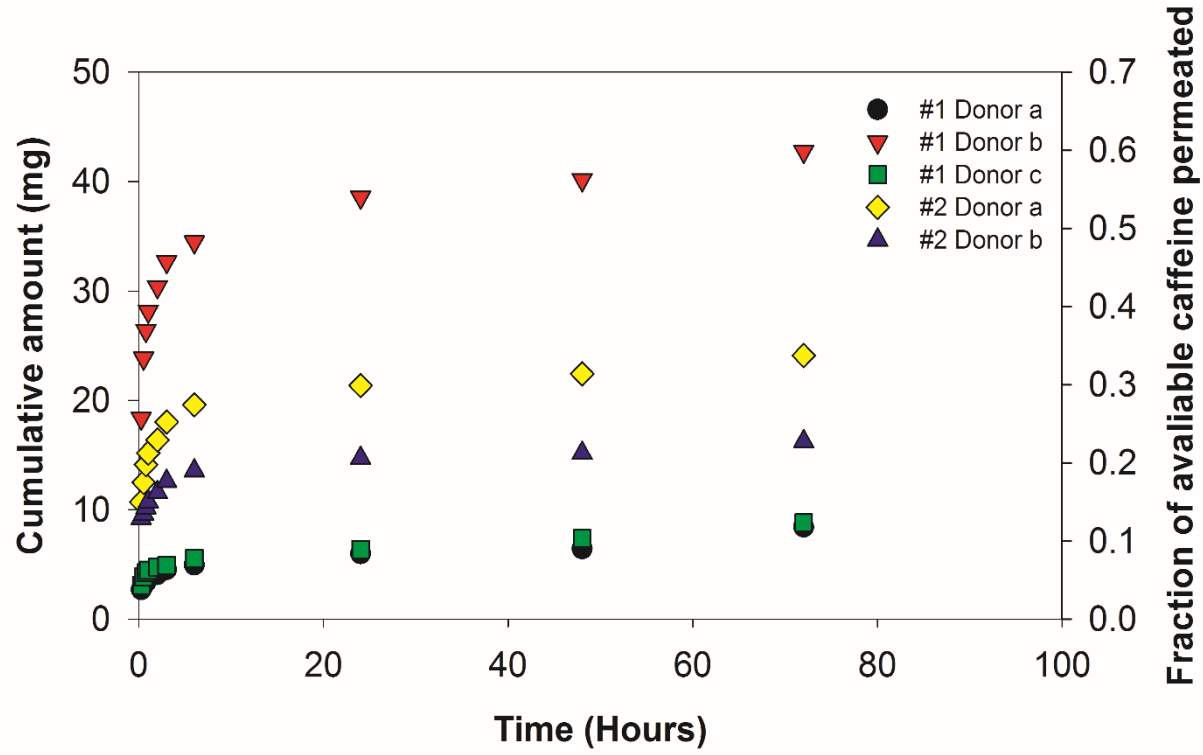

Figure 7.3: Double y-axis displaying cumulative amount and fraction of caffeine dose permeated applied over the first 6 hours.

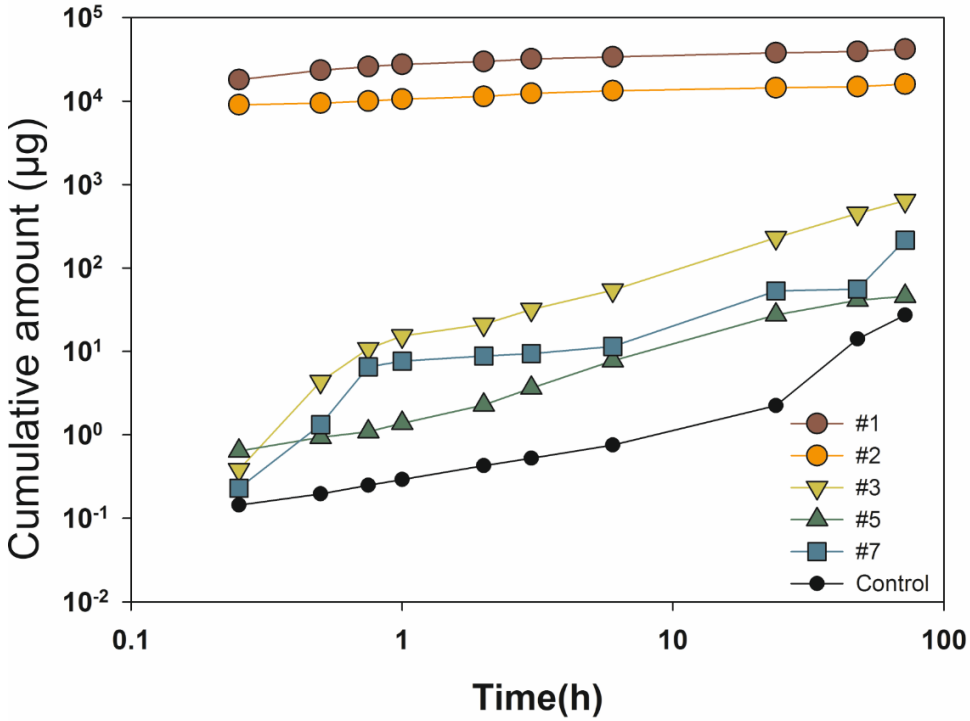

Figure 7.4: Cumulative amount of caffeine permeated for the nails from donor b. Five of the nails are porated: #1 and #2 fully; #3, #5, and #7 partially. A control (intact) nail is given for comparison.

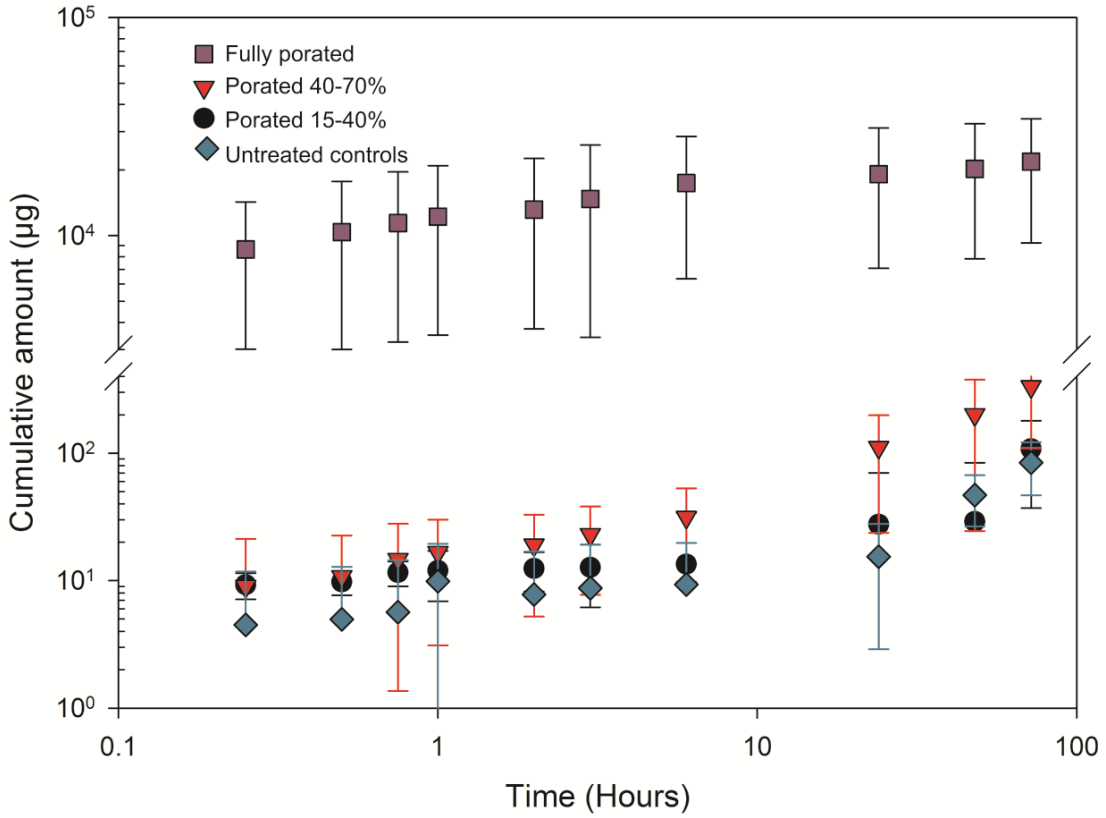

Figure 7.5: Cumulative caffeine penetration as a function of time across samples. The results have been grouped by the degree of laser ablation achieved, specifically, (i) fully porated (n = 5), (ii) porated to 40-70% of the total nail thickness (n = 3), (iii) porated to 15-40% of the total nail thickness (n = 10), and (iv) untreated controls (n = 4).

7.4 Discussion

From the results in the previous section it can be seen partial and complete poration of the nail plate impact caffeine permeation by two mechanisms. Complete poration effectively bypasses the nail barrier providing tunnels through which caffeine diffuses across a concentration gradient in the PBS. On the other hand, partial poration reduces the plate thickness for a certain area of the nail, hence, reducing the distance caffeine has to permeate in these regions. The diffusion character for these two processes, in addition to the use of partial poration for the development of a minimally-invasive drug delivery strategy are discussed in the following sections.

7.4.1 Full Poration

The relatively high variability in the amount of caffeine delivered in fully porated samples is attributed in part to the variation in thickness of the nail samples examined (Table 1). In addition, the total area porated also impacts the permeation. The rate of diffusion of a molecule is proportional to the concentration gradient and the area across which it diffuses. From this it is logical to normalise the cumulative amount by the porated nail area and the inverse thickness, these values are shown in Table 2.

To better illustrate the effect this normalisation has, the coefficent of variation is shown. This is calculated by dividing the standard deviation of a data point by the mean of that data point. The important contributions of nail thickness and porated area variability may be appreciated by the manner in which normalisation of caffeine by these factors reduces the variation by a factor between 3.5-10.

Table 7.2: Absolute and normalised permeation of caffeine(mean ± S.D.; n = 5), with their assoicated coefficients of variation, across fully porated nails as a function of time.

Time (h)	**0.25**	**0.50**	**0.75**	**1**	**2**	**3**	**6**	**24**	**48**	**72**
Cumulative caffeine permeation (mg)	8.6 ± 5.6	10 ± 7.4	11 ± 8.2	12 ± 8.7	13 ± 9.4	14 ± 10.2	15 ± 10.7	17 ± 11.9	18 ± 12.1	20 ± 12.5
Coefficient of variation	0.65	0.74	0.75	0.73	0.72	0.73	0.71	0.70	0.67	0.63
Caffeine permeation normalised by porated nail area and inverse thickness (µg µm^{-1})	2.4 ± 0.46	2.8± 0.42	3.1 ± 0.43	3.3 ± 0.42	3.6 ± 0.43	3.9 ± 0.44	4.2 ± 0.43	4.7 ± 0.41	5.0 ± 0.39	5.6 ± 0.35
Coefficient of variation	0.19	0.15	0.14	0.13	0.12	0.11	0.10	0.09	0.08	0.06

7.4.2 Diffusion Through Intact and Partially Porated Nails

The diffusion of a permeant across a membrane, such as the nail plate, can be described mathematically using Fick's laws. Fick's first law relates the flux, *J*, through a membrane to the concentration gradient within the membrane:

$$J = -D\frac{dC(z)}{dz} \tag{7.1}$$

where *C(z)* is the concentration, *z* is the position, and *D* the diffusion coefficient. In the case of the nail plate there is an associated lag time whilst the molecule diffuses across the membrane. This is because the concentration of a permeant inside the plate is initially zero (at the time $t = 0$). The concentration change during the lag time can be expressed mathematically. Setting up the boundary conditions, the concentration at the surfaces of the membrane $z = 0$ and $z = l$ are C_1 and C_2 respectively. Before steady state is achieved the concentration at a point in the membrane *z* is given by[123]:

$$C(z) = C_1 + (C_2 - C_1)\frac{z}{l} +$$

$$\frac{2}{\pi}\sum_{n=1}^{\infty}\frac{C_2\cos n\pi - C_1}{n}\sin\frac{n\pi z}{l}\exp\left(-\frac{n^2\pi^2 Dt}{l^2}\right) +$$

$$\frac{4C_0}{\pi}\sum_{n=0}^{\infty}\frac{1}{2m+1}\sin\frac{(2m+1)\pi z}{l}\exp\left\{-\frac{(2n+1)^2\pi^2 Dt}{l^2}\right\} \tag{7.2}$$

In steady state, this becomes a linear distribution, because as $t \rightarrow \infty$ the exponential containing sums vanish.

To obtain the rate of cumulative amount exiting a membrane, Equation 7.2 is initially differentiated with respect to *z* and multiplied by *–D*.

To obtain cumulative amount, integration is performed with respect to *t*. As the concentration in the receptor is initially equal to 0 ($C_2 = 0$) the following can be obtained:

$$\frac{Q_t}{lC_1} = \frac{Dt}{l^2} - \frac{1}{6} - \frac{2}{\pi^2}\sum_1^\infty \frac{(-1)^n}{n^2}\exp(-\frac{n^2\pi^2 Dt}{l^2}) \tag{7.3}$$

As t → ∞ , Equation 7.3 approaches steady state with a linear Q(t) dependence:

$$Q(t) = \frac{DC_1}{l}\left(t - \frac{l^2}{6D}\right) \tag{7.4}$$

As shown in Figure 7.6a), this line intercepts the time axis at the lag time τ:

$$\tau = \frac{l^2}{6D} \tag{7.5}$$

With regards to the permeation experiments this equation suitably describes the lag time for the intact control nails. However, partial drilling of the plate reduces the diffusion path length *l* in those regions beneath the pore, as shown schematically in Figure 7.6b).

This reduction in *l* should shift the lag time for partially porated samples. To investigate this, the cumulative amount is plotted for nails porated to various depths, along with two control samples in Figure 7.7a). A change in gradient is seen for the control samples, and those with minimal drilling, between 24-48 hours. In comparison, several of the samples drilled to larger depths (*i.e* smaller *l)* display a change in gradient around 6 hours.

According to Equation 7.3, the evolution of *Q* with time depends on the parameters Dt/l^2. Thus scaling *Q(t)* by the corresponding l^2 brings the curves closer together as shown in Figure 7.7b). Scaling the partially porated samples using their reduced thickness does not take into account that only a small percentage of each nail sample was drilled (1-5%),

with the majority of each nail still effectively 'intact'. However, given that none of the pores are cylindrical, tending to be conical, it simplifies calculations to just use the reduced thickness.

As the diffusion coefficient D is likely to vary for different donors, Figures 7.8a) and 7.8b) show the data just for donor b, the nails which had the greatest range of depths drilled. The contribution from porated regions in reducing the lag time is most apparent in the sample drilled to 110 μm (70% of the thickness of this nail).

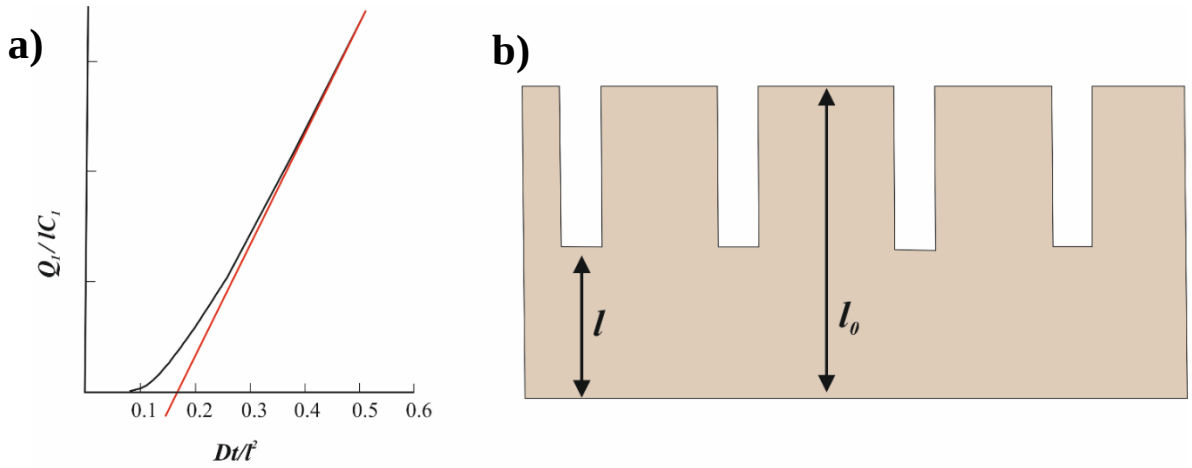

Figure 7.6: a) Plot of Equation 7.3 showing the cumulative amount of permeant exiting a membrane, the red line is the gradient as $t \rightarrow \infty$, intercepts the time axis at the lag time τ; b) Schematic illustrating the membrane thickness of a nail plate l_0, and the reduced thickness for those regions that are partially porated..

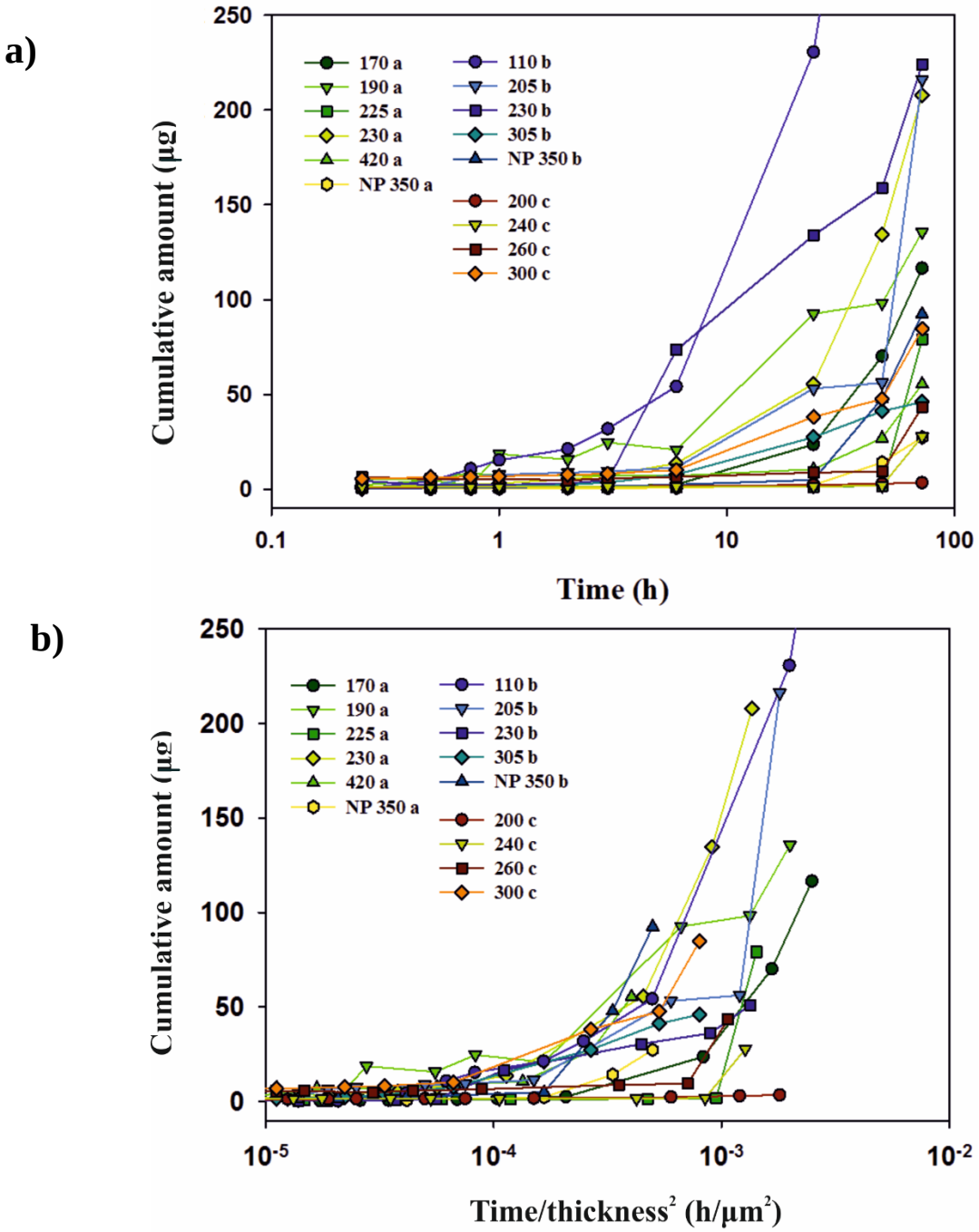

Figure 7.7: a) Cumulative amount of permeated caffeine plotted as a function of time for partially porated nails, the legend details the thickness (in µm) remaining from the base of the pore and the donor (a,b,c); b) Plot in which the data has been scaled by the thickness remaining, so the x-axis become time/ thickness².

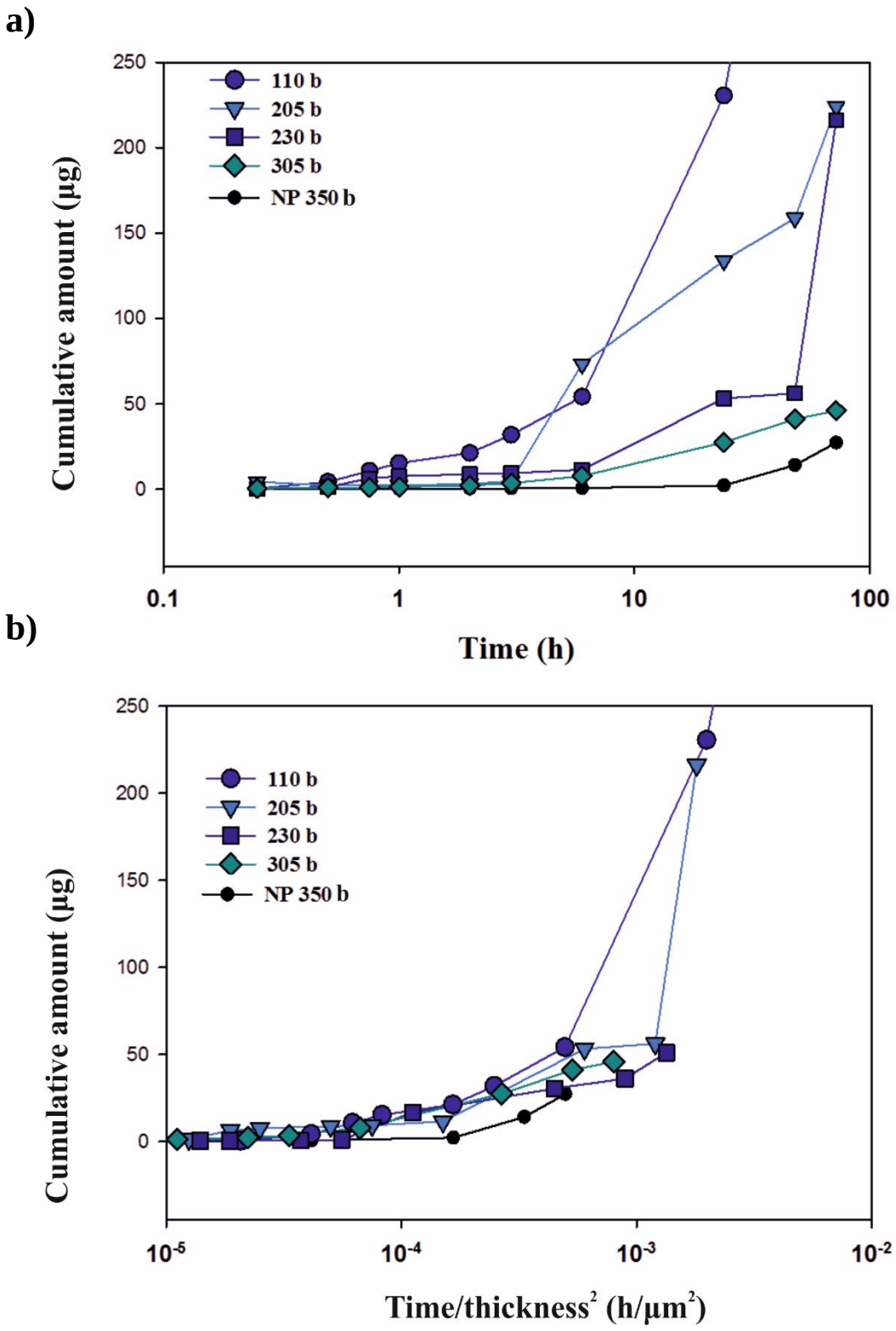

Figure 7.8: a) Cumulative amount permeated plotted as a function time for partially porated nails from donor b. The legend details the thickness remaining from the base of the pore in µm, b) Plot in which the data has been scaled by the thickness remaining, so the x-axis become time/ thickness^2.

7.4.3 Lateral Diffusion and Formulation Reservoirs

The lateral diffusion of molecules including Nile Red and Methyl Red have been demonstrated in the literature in intact nails and those porated with a derma roller [64,124]. Figure 7.9 shows a schematic representation of lateral diffusion of molecules in human nails. Initially, the molecules are confined in a donor compartment on the surface of the nail. From here they begin to diffuse down the concentration gradient, into the nail plate. As they diffuse into the plate, the molecules also spread out laterally. This results in diffusion into regions of the nail plate outside of the volume underneath the confined location of the formulation on the surface. This lateral diffusion can be harnessed, with laser poration to offer an opportunity for sequestration of a drug formulation, from which slow, continuous release might be envisaged [64].

A concern for lateral diffusion was coagulation that may seal off pores, as reported in skin when higher energies were used [71]. Scanning Electron Microscope (SEM) images displayed in Figure 7.10 show the interior of two pores. Panels a) and b) show a pore drilled with regimen #1. Pores drilled with this high energy regimen were shown to have the greatest heating of tissue surrounding the ablation zone in Chapter 6. These spaces are far larger (~2-10 μm) than any drug molecule and would offer pathways to aid lateral diffusion. This appeared to hold true for low energies, the pore in c) was drilled with Regimen #7, and also shows porous surrounding in the lower half.

We envisage the clinical use of partial poration by drilling the plate to ~95%. This would leave some level of barrier function in the nail, but drastically reduce the permeation path. These pores would be used as formulation ‘reservoirs’, they would be filled with a topical formulation and sealed off with a varnish. As well as permeation into the nail bed the drug would diffuse laterally into the surroundings, a useful feature for dealing with infecting organisms present within the nail plate itself.

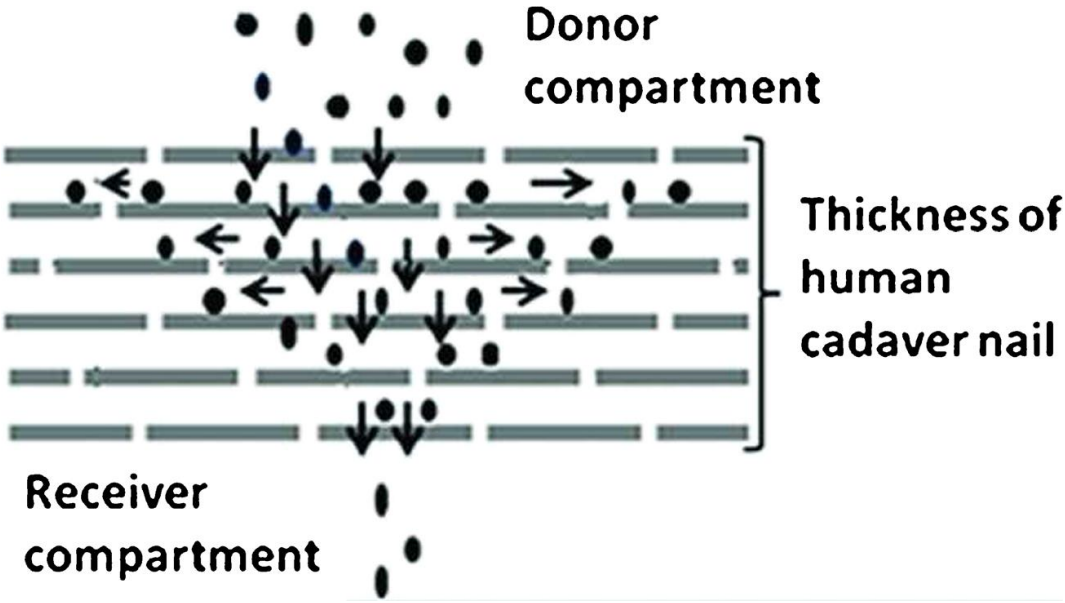

Figure 7.9: Schematic representation of lateral diffusion of drug molecules in human nails. The horizontal and the vertical arrows denote the lateral movement of the molecules and the transungual diffusion, respectively reproduced from [124] with permission.

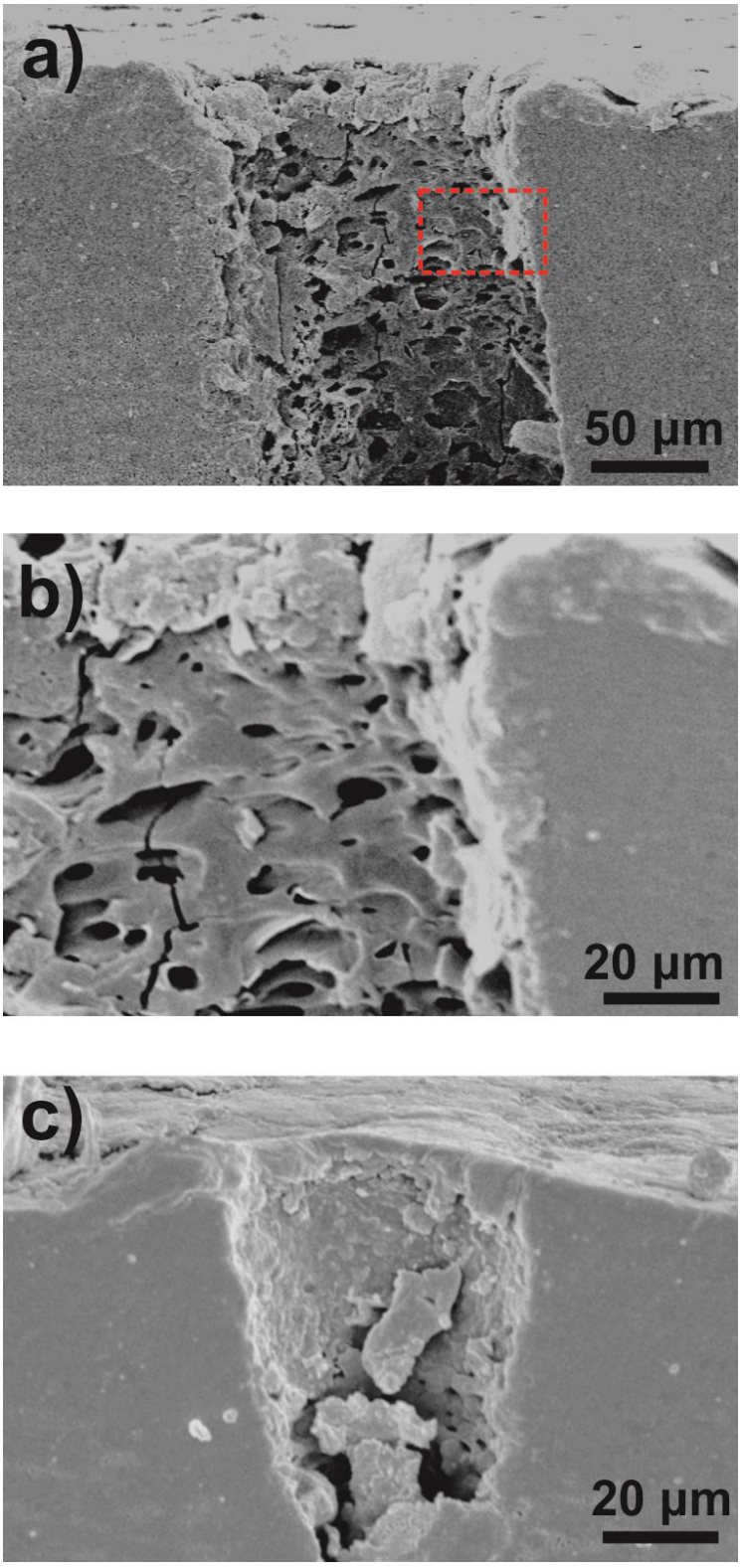

Figure 7.10: SEM images of microtomed nail sections after poration showing the porous appearance of nail structure adjacent to the ablation regime; a) pore drilled with regimen #1, (scale bar = 50 µm) b) Higher magnification micrograph captured inside the red box in a), c) pore drilled with regimen #7 (scale bar = 20 µm).

7.5 Concluding Remarks

This chapter presented the delivery of a model drug across nail plates modified by the laser-drilling of pores, either partially or completely across the plate. The results in this chapter demonstrate that full poration of nails completely circumvents the barrier provided by an intact, untreated sample. Partial poration, on the other hand, while not provoking such substantial effects on drug delivery, offers a strategy by which prolonged and controlled drug input to the nail itself, as well as the nail bed, may be achieved from sequestered formulations confined to the pores after their creation. Even with the highest pore drilling energy, the region surrounding the ablation zone appears porous, offering pathways for lateral diffusion into the surrounding plate. Both drilling modes offer attractive approaches for enhanced topical treatment of nail diseases.

Chapter 8

Conclusions and Further Work

Topical treatment of nail disease can be enhanced by physical modification of the nail plate, reducing the barrier to the permeation of drugs to the target site. Drilling of the nail plate with laser radiation is one possible technique to perform this. A range of microscopy and spectroscopy techniques have been used to study the nail plate's structure before and after optical drilling. For drilling of the plate, the first use of a femtosecond pulsed, visible light ($\lambda = 532$ nm), fibre optic laser was demonstrated. Due to the poor absorption of light by the nail plates it was necessary to stain the surface for facilitation of ablation. The amplitude of light pulses and exposure time were varied to porate to various depths within the plate. An optical chopper gave more time for the accumulated thermal energy to flow from the poration site, thus reducing thermal damage to the surrounding nail tissue. The geometry of pores, and the damage to the tissue surrounding them, was characterised with optical, electron and confocal microscopies.

It was observed that thermal treatment increases Raman scattering in the nail. An empirical relationship between the Raman scattering and the temperature was established for nail pieces heat-treated at specific temperatures. This relationship was used to create temperature maps across porated areas. These maps provided information on the drilling mechanism.

Nail samples were prepared by the drilling of pore arrays with various laser regimens. Permeation of a model drug, caffeine, through fully and partially porated nails was investigated.

8.1 Summary of Results

Optical, Scanning Electron (SEM) and Atomic Force (AFM) microscopies were used to study the nail plate. These techniques provided a reference to the plate's structure, and its variation across the nail thickness. Optical and SEM imaging displayed a rippling layered structure, with a high level of interdigitation between cells, but no clear pathways through the plate. Subsequently, AFM was used to resolve individual cells.

Fourier Transform Infrared (FTIR) and Raman spectroscopies were employed to investigate whether the chemical structure of the nail plate varies across its thickness. FTIR measurements were taken on the surfaces of nail plates (dorsal and ventral) and compared with the intermediate regions of the plates exposed by filing. The chemical structure of the dorsal and ventral regions was found to be similar. The intermediate region differed to the outer regions, with different ratios of protein secondary structures and amino acid groups. To complement FTIR measurements, Raman line scans were taken across the z-axis of nail plates. The background signal intensity was shown to be strongly depth-dependent being greatest in the ventral region and lowest in the intermediate region. With regards to the peak intensity and position of bond-specific Raman peaks, no clear variation was observed.

Further investigation of the structure of the nail with microscopic and spectroscopic techniques would provide additional information on the properties of the plate, potentially optimising treatment techniques. Gaps in knowledge of the nail plate exist, despite the rapid improvement of analysis techniques. For example, commonly used references are taken from dated studies of the nail structure that can be difficult to access, and which often display low-quality images obtained with optical or electron microscopies. Furthermore, a quantitative study of the nail plate with AFM would provide information previously unobtainable. Not only could the plate be characterised topographically across the thickness, but its mechanical properties could be probed using indentation operating modes. For instance, this would allow the effect of a chemical penetration enhancer on the plate to be studied. Also, it may be possible to elucidate changes to the peaks in Raman spectra, across the nail thickness, by sampling a larger number of donors. This could be further combined with a more thorough statistical analysis.

Poration of the nail plate was used to reduce the thickness of the membrane. Optical drilling was performed using a 532 nm femtosecond pulsed laser. The laser beam was focused onto the nail plate using a photonic crystal fibre. First results showed that this wavelength of light was poorly absorbed by the nail. Therefore, to facilitate absorption of light the plates were stained with a dye. This way, sufficient energy was trapped in the focal volume to initiate the ablation process, creating pores into and through the plate. These pore openings were investigated with optical microscopy.

'Optimal' pores were achieved with minimal burning to the surrounding material through manipulation of the average power and exposure time of the beam. In addition, visible burning around the pore was reduced by modification of the pulse train, using an optical chopper. Moreover, a custom chopper blade with a single slit was designed and tested, which further reduced the damage. Although this custom chopper blade reduced the damage surrounding a pore, the total drilling time was considerably increased.

The interior of pores was assessed by imaging cross-sectioned plates. Subsequently, Laser Scanning Confocal Microscopy (LSCM) was used to measure the depths of pores without the need for further processing of the sample.

Drilling regimens were established with varied laser parameters, to porate nail samples for permeation experiments. A second laser system was used for the preparation of samples for permeation experiments,. This system had five-times greater power output, therefore pores could be drilled through the entirety of the nail in less than a 10^{th} of a second.

The depth of drilling was shown to be dependent on the exposure time for a specific power. Discrete exposure times were achieved using an analogue shutter, in combination with the optical chopper. For further work, the use of a digital chopper would enable a wider range of exposure times to be tested. This would result in better control of the drilling depth, which might allow poration into specific depths and be of use in situations where nail plates may be altered due to the nail diseases.

Optical and LSCM imaging provided only qualitative information on the thermal damage caused to the plate during poration. Further to these, a quantitative technique was developed to provide greater detail of the damage to the tissue and insight into the drilling mechanisms. An empirical relationship was generated by heat-treating nail pieces in a furnace at specific temperatures, and then measuring the Raman scattering from dorsal

surface of the nails. This empirical relationship was generalised to take into account the variation in signal intensity across the nail thickness. Raman mapping was used to acquire an array of spectra, with the intensity of Raman scattering in each spectra was converted to a temperature. These data were then used to plot two- and three-dimensional temperature maps.

The maps allowed the drilling process to be characterised. The central region of pores was removed by plasma-mediated ablation. Optical breakdown of the stained surface in the path of the beam initiated a change to the base of the pore, increasing the susceptibility of the plate to absorb subsequent pulses. This self-seeding process ensured that drilling of the entirety of the plate was possible. Also, the edges of the pores were subject to heating, and if sufficient temperatures were achieved, photothermal ablation of the tissue occurred.

There are several potential uses of this technique for future work. The Raman mapping technique could be used for direct comparison of pores created with this system to those obtained with other systems. Moreover, this technique has additional use in measuring the thermal damage caused to other tissues or heat sensitive materials. Following the generation of a material-specific calibration curve, damage caused by accidental or intentional treatments could also be quantified.

With the drilling process characterised, permeation experiments were performed on control and porated nails, using caffeine as a model drug. Arrays of pores were drilled into the nail plates obtained from the donors. In comparison to control nails, the shortened permeation path length in partially porated samples reduced the time needed to reach steady-state. Complete poration of the nail enables orders-of-magnitude increases in the transport of the tested drug to the underside of the nail plate.

Partial poration of the plate offers a unique opportunity to treat nail disease. Further studies should investigate how permeation is affected when pores are drilled to greater than 70% of the thickness of the nail. It may be that sufficient delivery to the target site is achievable without the need to completely porate the plate, especially if the infection is confined to the plate. This would leave the nail in a less compromised state, and make post-operative management simpler.

The drilling technique, developed during this project, provides a solution to the poor topical permeation of drug, which might be used to aid the treatment of nail diseases. The

pores created were smaller in diameter than those reported in the literature, whilst control of drilling depth within the plate was achieved by simple manipulation of the average power and exposure time. In addition, visible light may be safer to work with in a clinical setting than the infrared frequencies used in some commercial tissue ablation systems. Several adaptions to the technique would provide even greater flexibility for further testing and/or use in a clinical setting. Firstly, the incorporation of the fibre into a small ergonomic laser delivery head would solve the issues with alignment. The fibre tip could be placed normal to the surface of a nail and drilling performed. This would simplify operator use, and drastically reduce the time to create an array. Secondly, the incorporation of a digital shutter into the setup for more precise control of exposure time would allow better adjustment for nails of varying thickness, which would be especially useful when the plate is drastically altered by disease. Finally, a post-operative strategy would need development, possibly the filling of pores with the appropriate drug for disease treatment and their covering with a protective sealant.

8.2 Concluding Remarks

The fibre laser system used provides a low-cost and compact light source for the drilling of the nail plate. Pores were characterised with optical, Raman, SEM and LSCM imaging allowing determination of the poration mechanism. Optimisation of the technique meant pores were drilled with minimal damage to the regions surrounding the site, whilst enhancing the permeation of a topically applied model compound. This thesis has therefore described a technique with which transungual delivery can be enhanced.

Bibliography

1 de Berker, D. A. R., André, J. & Baran, R. Nail biology and nail science. *International Journal of Cosmetic Science* **29**, 241-275, doi:10.1111/j.1467-2494.2007.00372.x (2007).

2 Lawry, M. & Rich, P. The nail apparatus: A guide for basic and clinical science. *Current Problems in Dermatology* **11**, 161-208, doi:http://dx.doi.org/10.1016/S1040-0486(99)90001-7 (1999).

3 Jiaravuthisan, M. M., Sasseville, D., Vender, R. B., Murphy, F. & Muhn, C. Y. Psoriasis of the nail: Anatomy, pathology, clinical presentation, and a review of the literature on therapy. *Journal of the American Academy of Dermatology* **57**, 1-27, doi:http://dx.doi.org/10.1016/j.jaad.2005.07.073 (2007).

4 Jiaravuthisan, M. M., Sasseville, D., Vender, R. B., Murphy, F. & Muhn, C. Y. Psoriasis of the nail: Anatomy, pathology, clinical presentation, and a review of the literature on therapy. *J. Am. Acad. Dermatol.* **57**, 1-27, doi:10.1016/j.jaad.2005.07.073 (2007).

5 Achten, G. & Parent, D. The normal and pathological nail. *Int. J. Dermatol.* **22**, 556-565, doi:10.1111/j.1365-4362.1983.tb02124.x (1983).

6 de Berker, D., Mawhinney, B. & Sviland, L. Quantification of regional matrix nail production. *Br. J. Dermatol.* **134**, 1083-1086, doi:10.1046/j.1365-2133.1996.d01-906.x (1996).

7 Fleckman, P. in *Nails. Diagnosis Therapy Surgery* (ed R. Scher, Daniel III, C. R.,) (Elsevier Saunders, 2005).

8 Schweizer, J. *et al.* New consensus nomenclature for mammalian keratins. *J. Cell Biol.* **174**, 169-174, doi:10.1083/jcb.200603161 (2006).

9 Lynch, M. H., Oguin, W. M., Hardy, C., Mak, L. & Sun, T. T. Acidic and basic hair nail (hard) keratins - their colocalization in upper cortical and cuticle cells of the human-hair follicle and their relationship to soft keratins. *J. Cell Biol.* **103**, 2593-2606, doi:10.1083/jcb.103.6.2593 (1986).

10 Garson, J. C., Baltenneck, F., Leroy, F., Riekel, C. & Muller, M. Histological structure of human nail as studied by synchrotron X-ray microdiffraction. *Cell. Mol. Biol.* **46**, 1025-1034 (2000).

11 Murdan, S. Enhancing the nail permeability of topically applied drugs. *Expert Opin. Drug Deliv.* **5**, 1267-1282, doi:10.1517/17425240802497218 (2008).

12 Kobayashi, Y., Miyamoto, M., Sugibayashi, K. & Morimoto, Y. Drug permeation through the three layers of the human nail plate. *J. Pharm. Pharmacol.* **51**, 271-278, doi:10.1211/0022357991772448 (1999).

13 de Berker, D., and B. Forslind. . in *Skin, Hair, and Nails, Structure and Function,* (ed M.Linberg and L. Norlen. B. Forslind) (Marcel Dekker, 2004).

14 Egawa, M., Ozaki, Y. & Takahashi, M. In vivo measurement of water content of the fingernail and its seasonal change. *Skin Res. Technol.* **12**, 126-132, doi:10.1111/j.0909-752X.2006.00141.x (2006).

15 Stern, D. K. *et al.* Water content and other aspects of brittle versus normal fingernails. *Journal of the American Academy of Dermatology* **57**, 31-36, doi:10.1016/j.jaad.2007.02.004 (2007).
16 Scher, R. K. Onychomycosis: A significant medical disorder. *Journal of the American Academy of Dermatology* **35**, S2-S5, doi:http://dx.doi.org/10.1016/S0190-9622(96)90061-4 (1996).
17 Elewski, B. E. Onychomycosis: Pathogenesis, diagnosis, and management. *Clin. Microbiol. Rev.* **11**, 415-+ (1998).
18 Zaias, N., Glick, B. & Rebell, G. Diagnosing and treating onychomycosis. *J. Fam. Pract.* **42**, 513-518 (1996).
19 Cohen, J. L., R. K. Scher, and A. S. Pappert. in *Cutaneous fungal infections* (ed B. Elewski) 106-122 (Igaku-Shoin Inc, 1992).
20 Dompmartin, D., Dompmartin, A., Deluol, A. M., Grosshans, E. & Coulaud, J. P. Onychomycosis and aids - clinical and laboratory findings in 62 patients. *Int. J. Dermatol.* **29**, 337-339, doi:10.1111/j.1365-4362.1990.tb04755.x (1990).
21 Zaias, N. Onychomycosis. *Arch. Dermatol.* **105**, 263-&, doi:10.1001/archderm.105.2.263 (1972).
22 Farber, E. M. & Peterson, J. B. Variations in natural history of psoriasis. *California Medicine* **95**, 6-& (1961).
23 Samman, p. D. Nail in psoriasis. *Medical and Biological Illustration* **15**, 148-& (1965).
24 Tosti A, P. B. in *Nails: therapy, diagnosis, surgery,* (eds Scher RK & Daniel III CR) (WB Saunders, 2005).
25 Elsayed, M. M. A. Development of topical therapeutics for management of onychomycosis and other nail disorders: A pharmaceutical perspective. *J. Control. Release* **199**, 132-144, doi:10.1016/j.jconrel.2014.11.017 (2015).
26 Lahfa, M. *et al.* Efficacy, Safety and Tolerability of an Optimized Avulsion Technique with ONYSTER (R) (40% Urea Ointment with Plastic Dressing) Ointment Compared to Bifonazole-Urea Ointment for Removal of the Clinically Infected Nail in Toenail Onychomycosis: a Randomized Evaluator-Blinded Controlled Study. *Dermatology* **226**, 5-12, doi:10.1159/000345105 (2013).
27 Baran, R., Hay, R. J. & Garduno, J. I. Review of antifungal therapy and the severity index for assessing onychomycosis: Part I. *J. Dermatol. Treat.* **19**, 72-81, doi:10.1080/09546630701243418 (2008).
28 De Doncker, P. Pharmacokinetics of orally administered antifungals in onychomycosis. *Int. J. Dermatol.* **38**, 20-27, doi:10.1046/j.1365-4362.1999.00010.x (1999).
29 Elewski, B. E. & Hay, R. J. Update on the management of onychomycosis: Highlights of the third annual international summit on cutaneous antifungal therapy. *Clin. Infect. Dis.* **23**, 305-313 (1996).
30 Pharmaceutica., J. (eds Janssen Pharmaceutica & N.J. Titusville) (1997).
31 Haria, M., Bryson, H. M. & Goa, K. L. Itraconazole - A reappraisal of its pharmacological properties and therapeutic use in the management of superficial fungal infections. *Drugs* **51**, 585-620 (1996).

32 Roseeuw, D. & Dedoncker, P. New approaches to the treatment of onychomycosis. *Journal of the American Academy of Dermatology* **29**, S45-S50 (1993).
33 Effendy, I., Lecha, M., de Chauvin, M. F., Di Chiacchio, N. & Baran, R. Epidemiology and clinical classification of onychomycosis. *J. Eur. Acad. Dermatol. Venereol.* **19**, 8-12, doi:10.1111/j.1468-3083.2005.01281.x (2005).
34 Elkeeb, R., AliKhan, A., Elkeeb, L., Hui, X. Y. & Maibach, H. I. Transungual drug delivery: Current status. *Int. J. Pharm.* **384**, 1-8, doi:10.1016/j.ijpharm.2009.10.002 (2010).
35 Mertin, D. & Lippold, B. C. In-vitro permeability of the human nail and of a keratin membrane from bovine hooves: Prediction of the penetration rate of antimycotics through the nail plate and their efficacy. *J. Pharm. Pharmacol.* **49**, 866-872 (1997).
36 Kobayashi, Y. *et al.* In vitro permeation of several drugs through the human nail plate: relationship between physicochemical properties and nail permeability of drugs. *Eur. J. Pharm. Sci.* **21**, 471-477, doi:10.1016/j.ejps.2003.11.008 (2004).
37 Higa, M., Tanioka, A. & Miyasaka, K. A study of ion permeation across a charged membrane in multicomponent ion systems as a function of membrane charge-density. *J. Membr. Sci.* **49**, 145-169, doi:10.1016/s0376-7388(00)80785-1 (1990).
38 Walters, K. A., Flynn, G. L. & Marvel, J. R. Physicochemical characterization of the human nail - solvent effects on the permeation of homologous alcohols. *J. Pharm. Pharmacol.* **37**, 771-775 (1985).
39 Repka, M. A., Mididoddi, P. K. & Stodghill, S. P. Influence of human nail etching for the assessment of topical onychomycosis therapies. *Int. J. Pharm.* **282**, 95-106, doi:10.1016/j.ijpharm.2004.06.010 (2004).
40 Flagothier, C., Pierard-Franchimont, C. & Pierard, G. E. New insights into the effect of amorolfine nail lacquer. *Mycoses* **48**, 91-94, doi:10.1111/j.1439-0507.2004.01090.x (2005).
41 Walters, K. A., Flynn, G. L. & Marvel, J. R. Physicochemical characterization of the human nail .1. Pressure sealed apparatus for measuring nail plate permeabilities. *J. Invest. Dermatol.* **76**, 76-79, doi:10.1111/1523-1747.ep12525318 (1981).
42 Kobayashi, Y., Miyamoto, M., Sugibayashi, K. & Morimoto, Y. Enhancing effect of N-acetyl-L-cysteine or 2-mercaptoethanol on the in vitro permeation of 5-fluorouracil or tolnaftate through the human nail plate. *Chem. Pharm. Bull.* **46**, 1797-1802 (1998).
43 Murdan, S. Drug delivery to the nail following topical application. *Int. J. Pharm.* **236**, 1-26, doi:10.1016/s0378-5173(01)00989-9 (2002).
44 Haria, M. & Bryson, H. N. Amorolfine - a review of its pharmacological properties and therapeutic potential in the treatment of onychomycosis and other superficial fungal-infections. *Drugs* **49**, 103-120 (1995).
45 Gupta, A. Combination therapy using ciclopirox topical nail lacquer 8% solution and oral terbinafine for the treatment of moderate to severe toenail

onychomycosis in dermatophyte-positive patients. *Journal of the American Academy of Dermatology* **52**, P123-P123 (2005).

46 Hay, R. J., Mackie, R. M. & Clayton, Y. M. Tioconazole nail solution - an open study of its efficacy in onychomycosis. *Clin. Exp. Dermatol.* **10**, 111-115, doi:10.1111/j.1365-2230.1985.tb00537.x (1985).

47 Hui, X. Y. *et al.* Ciclopirox delivery into the human nail plate. *J. Pharm. Sci.* **93**, 2545-2548, doi:10.1002/jps.20159 (2004).

48 Schissel, D. J. & Elston, D. M. Topical 5-fluorouracil treatment for psoriatic trachyonychia. *Cutis* **62**, 27-28 (1998).

49 Fredriksson, T. Topically applied fluorouracil in the treatment of psoriatic nails. *Arch. Dermatol.* **110**, 735-736, doi:10.1001/archderm.1974.01630110033006 (1974).

50 Rigopoulos, D., Ioannides, D., Prastitis, N. & Katsambas, A. Nail psoriasis: A combined treatment using calcipotriol cream and clobetasol propionate cream. *Acta Derm.-Venereol.* **82**, 140-140, doi:10.1080/00015550252948220 (2002).

51 Repka, M. A., O'Haver, J., See, C. H., Gutta, K. & Munjal, M. Nail morphology studies as assessments for onychomycosis treatment modalities. *Int. J. Pharm.* **245**, 25-36, doi:10.1016/s0378-5173(02)00321-6 (2002).

52 Stricks, W. & Kolthoff, I. M. Equilibrium constants of the reactions of sulfite with cystine and with dithiodiglycolic acid. *J. Am. Chem. Soc.* **73**, 4569-4574, doi:10.1021/ja01154a022 (1951).

53 Khengar, R. H., Jones, S. A., Turner, R. B., Forbes, B. & Brown, M. B. Nail swelling as a pre-formulation screen for the selection and optimisation of ungual penetration enhancers. *Pharm. Res.* **24**, 2207-2212, doi:10.1007/s11095-007-9368-3 (2007).

54 Pittrof, F., Gerhards, J., Erni, W. & Klecak, G. Loceryl(r) nail lacquer - realization of a new galenical approach to onychomycosis therapy. *Clin. Exp. Dermatol.* **17**, 26-28, doi:10.1111/j.1365-2230.1992.tb00273.x (1992).

55 Lauharanta, J. Comparative efficacy and safety of amorolfine nail lacquer 2-percent versus 5-percent once weekly. *Clin. Exp. Dermatol.* **17**, 41-43, doi:10.1111/j.1365-2230.1992.tb00277.x (1992).

56 Murthy, S. N., Wiskirchen, D. E. & Bowers, C. P. Iontophoretic drug delivery across human nail. *J. Pharm. Sci.* **96**, 305-311, doi:10.1002/jps.20757 (2007).

57 Hao, J. S. & Li, S. K. Mechanistic Study of Electroosmotic Transport Across Hydrated Nail Plates: Effects of pH and Ionic Strength. *J. Pharm. Sci.* **97**, 5186-5197, doi:10.1002/jps.21368 (2008).

58 Dutet, J. & Delgado-Charro, M. B. Electroosmotic transport of mannitol across human nail during constant current iontophoresis. *J. Pharm. Pharmacol.* **62**, 721-729, doi:10.1211/jpp/62.06.0008 (2010).

59 Hao, J. S., Smith, K. A. & Li, S. K. Iontophoretically Enhanced Ciclopirox Delivery into and Across Human Nail Plate. *J. Pharm. Sci.* **98**, 3608-3616, doi:10.1002/jps.21664 (2009).

60 Mididoddi, P. K. & Repka, M. A. Characterization of hot-melt extruded drug delivery systems for onychomycosis. *Eur. J. Pharm. Biopharm.* **66**, 95-105, doi:10.1016/j.ejpb.2006.08.013 (2007).
61 Abadi, D. & Zderic, V. Ultrasound-Mediated Nail Drug Delivery System. *J. Ultrasound Med.* **30**, 1723-1730 (2011).
62 Salter, S. A., Ciocon, D. H., Gowrishankar, T. R. & Kimball, A. B. Controlled nail trephination for subungual hematoma. *Am. J. Emerg. Med.* **24**, 875-877, doi:10.1016/j.ajem.2006.03.029 (2006).
63 Ciocon, D., Gowrishankar, T., Herndon, T. & Kimball, A. B. How low should you go: Novel device for nail trephination. *Dermatol. Surg.* **32**, 828-833, doi:10.1111/j.1524-4725.2006.32168.x (2006).
64 Chiu, W. S. *et al.* Drug delivery into microneedle-porated nails from nanoparticle reservoirs. *J. Control. Release* **220**, 98-106, doi:10.1016/j.jconrel.2015.10.026 (2015).
65 Chiu, W. S. *Visualization of the mechanism(s) of drug transport and delivery into and through the nail*, University of Bath, (2014).
66 Straight, R. C. Leon Goldman: Dermatologist & surgeon; pioneer and leader in laser surgery and medicine (1905–1997). *Lasers in Surgery and Medicine* **48**, 911-911, doi:10.1002/lsm.22605 (2016).
67 Buer, C. S., Gahagan, K. T., Swartzlander, G. A. & Weathers, P. J. Insertion of microscopic objects through plant cell walls using laser microsurgery. *Biotechnol. Bioeng.* **60**, 348-355, doi:10.1002/(sici)1097-0290(19981105)60:3<348::aid-bit11>3.0.co;2-i (1998).
68 Mohanty, S. K., Sharma, M. & Gupta, P. K. Laser-assisted microinjection into targeted animal cells. *Biotechnol. Lett.* **25**, 895-899, doi:10.1023/a:1024038609045 (2003).
69 Botvinick, E. L., Venugopalan, V., Shah, J. V., Liaw, L. H. & Berns, M. W. Controlled ablation of microtubules using a picosecond laser. *Biophys. J.* **87**, 4203-4212, doi:10.1529/biophysj.104.049528 (2004).
70 Konig, K., Riemann, I. & Fritzsche, W. Nanodissection of human chromosomes with near-infrared femtosecond laser pulses. *Opt. Lett.* **26**, 819-821, doi:10.1364/ol.26.000819 (2001).
71 Jacques, S. L., McAuliffe, D. J., Blank, I. H. & Parrish, J. A. Controlled removal of human stratum-corneum by pulsed laser. *J. Invest. Dermatol.* **88**, 88-93, doi:10.1111/1523-1747.ep12465112 (1987).
72 Walsh, J. T., Flotte, T. J., Anderson, R. R. & Deutsch, T. F. Pulsed co2-laser tissue ablation - effect of tissue-type and pulse duration on thermal-damage. *Lasers in Surgery and Medicine* **8**, 108-118, doi:10.1002/lsm.1900080204 (1988).
73 Gomez, C. *et al.* Laser treatments on skin enhancing and controlling transdermal delivery of 5-fluorouracil. *Lasers in Surgery and Medicine* **40**, 6-12, doi:10.1002/lsm.20590 (2008).
74 Garvie-Cook, H., Stone, J. M., Yu, F., Guy, R. H. & Gordeev, S. N. Femtosecond pulsed laser ablation to enhance drug delivery across the skin. *J. Biophotonics* **9**, 144-154, doi:10.1002/jbio.201500120 (2016).

75 Neev, J. *et al.* Ablation of human nail by pulsed lasers. *Lasers in Surgery and Medicine* **21**, 186-192, doi:10.1002/(sici)1096-9101(1997)21:2<186::aid-lsm10>3.0.co;2-d (1997).
76 Yang, C. H., Tsai, M. T., Shen, S. C., Ng, C. Y. & Jung, S. M. Feasibility of ablative fractional laser-assisted drug delivery with optical coherence tomography. *Biomed. Opt. Express* **5**, 3949-3959, doi:10.1364/boe.5.003949 (2014).
77 Lim, E. H. *et al.* Toenail onychomycosis treated with a fractional carbon-dioxide laser and topical antifungal cream. *Journal of the American Academy of Dermatology* **70**, 918-923, doi:10.1016/j.jaad.2014.01.893 (2014).
78 Raman, S. C. V. A New Type of Secondary Radiation. *Ind. J. Phys.* **2**, 387 (1928).
79 Szymanski, H. A. *Raman Spectroscopy*. Vol. 1 (Springer US, 1967).
80 Barry, B. W., Edwards, H. G. M. & Williams, A. C. Fourier-transform raman and infrared vibrational study of human skin - assignment of spectral bands. *J. Raman Spectrosc.* **23**, 641-645, doi:10.1002/jrs.1250231113 (1992).
81 Gniadecka, M., Nielsen, O. F., Christensen, D. H. & Wulf, H. C. Structure of water, proteins, and lipids in intact human skin, hair, and nail. *J. Invest. Dermatol.* **110**, 393-398, doi:10.1046/j.1523-1747.1998.00146.x (1998).
82 Edwards, H. G. M., Hunt, D. E. & Sibley, M. G. FT-Raman spectroscopic study of keratotic materials: horn, hoof and tortoiseshell. *Spectroc. Acta Pt. A-Molec. Biomolec. Spectr.* **54**, 745-757, doi:10.1016/s1386-1425(98)00013-4 (1998).
83 Widjaja, E. & Seah, R. K. H. Use of Raman spectroscopy and multivariate classification techniques for the differentiation of fingernails and toenails. *Appl. Spectrosc.* **60**, 343-345, doi:10.1366/000370206776342607 (2006).
84 Widjaja, E., Lim, G. H. & An, A. A novel method for human gender classification using Raman spectroscopy of fingernail clippings. *Analyst* **133**, 493-498, doi:10.1039/b712389b (2008).
85 Wen, W., Meng, Y. Y., Xiao, J., Zhang, P. L. & Zhang, H. Comparative study on keratin structural changes in onychomycosis and normal human finger nail specimens by Raman spectroscopy. *J. Mol. Struct.* **1038**, 35-39, doi:10.1016/j.molstruc.2013.01.051 (2013).
86 Smijs, T. G. *et al.* Detection and differentiation of causative organisms of onychomycosis in an ex vivo nail model by means of Raman spectroscopy. *J. Eur. Acad. Dermatol. Venereol.* **28**, 1492-1499, doi:10.1111/jdv.12324 (2014).
87 Rippon, W. B., Koenig, J. L. & Walton, A. G. Laser Raman spectroscopy of biopolymers and proteins. *Journal of Agricultural and Food Chemistry* **19**, 692-697, doi:10.1021/jf60176a012 (1971).
88 Zhao, J., Lui, H., McLean, D. I. & Zeng, H. Automated autofluorescence background subtraction algorithm for biomedical Raman spectroscopy. *Appl. Spectrosc.* **61**, 1225-1232, doi:10.1366/000370207782597003 (2007).

89 Lieber, C. A. & Mahadevan-Jansen, A. Automated method for subtraction of fluorescence from biological Raman spectra. *Appl. Spectrosc.* **57**, 1363-1367, doi:10.1366/000370203322554518 (2003).
90 Bonnier, F. *et al.* Analysis of human skin tissue by Raman microspectroscopy: Dealing with the background. *Vibrational Spectroscopy* **61**, 124-132, doi:10.1016/j.vibspec.2012.03.009 (2012).
91 Bonnier, F. *et al.* In vitro analysis of immersed human tissues by Raman microspectroscopy. *J. Raman Spectrosc.* **42**, 888-896, doi:10.1002/jrs.2825 (2011).
92 Binnig, G., Rohrer, H., Gerber, C. & Weibel, E. Surface Studies by Scanning Tunneling Microscopy. *Physical Review Letters* **49**, 57-61 (1982).
93 Binnig, G., Quate, C. F. & Gerber, C. Atomic Force Microscope. *Physical Review Letters* **56**, 930-933 (1986).
94 Lyubchenko, Y. L., Gall, A. A., Shlyakhtenko, L. S., Harrington, R. E. & Lindsay, S. M. Atomic force microscopy imaging of large double-stranded DNA-molecules. *Faseb J.* **6**, A149-A149 (1992).
95 Muller, D. J. *et al.* Observing membrane protein diffusion at subnanometer resolution. *J. Mol. Biol.* **327**, 925-930, doi:10.1016/s0022-2836(03)00206-7 (2003).
96 Janovjak, H. *et al.* Imaging and detecting molecular interactions of single transmembrane proteins. *Neurobiol. Aging* **27**, 546-561, doi:10.1016/j.neurobiolaging.2005.03.031 (2006).
97 Gorzelanny, C. *et al.* Atomic force microscopy as an innovative tool for nanoanalysis of native stratum corneum. *Exp. Dermatol.* **15**, 387-391, doi:10.1111/j.0906-6705.2006.00424.x (2006).
98 Grandbois, M., Dettmann, W., Benoit, M. & Gaub, H. E. Affinity imaging of red blood cells using an atomic force microscope. *J. Histochem. Cytochem.* **48**, 719-724 (2000).
99 Mathur, A. B., Truskey, G. A. & Reichert, W. M. Atomic force and total internal reflection fluorescence microscopy for the study of force transmission in endothelial cells. *Biophys. J.* **78**, 1725-1735 (2000).
100 Henderson, E., Haydon, P. G. & Sakaguchi, D. S. Actin filament dynamics in living glial-cells imaged by atomic force microscopy. *Science* **257**, 1944-1946, doi:10.1126/science.1411511 (1992).
101 Schindelin, J. *et al.* Fiji: an open-source platform for biological-image analysis. *Nature methods* **9**, 676-682 (2012).
102 Parent, D., Achten, G. & Stouffsvanhoof, F. Ultrastructure of the normal human nail. *Am. J. Dermatopathol.* **7**, 529-535, doi:10.1097/00000372-198512000-00004 (1985).
103 Meyer, J. C. & Grundmann, H. P. Scanning electron-microscopic investigation of the healthy nail and its surrounding tissue. *J. Cutan. Pathol.* **11**, 74-79, doi:10.1111/j.1600-0560.1984.tb00353.x (1984).
104 Forslind, B. & Thyresson, N. Structure of normal nail - scanning electron-microscope study. *Archiv Fur Dermatologische Forschung* **251**, 199-204, doi:10.1007/bf00561761 (1975).

105 Sowa, M. G., Wang, J., Schultz, C. P., Ahmed, M. K. & Mantsch, H. H. Infrared spectroscopic investigation of in-vivo and ex-vivo human nails. *Vibrational Spectroscopy* **10**, 49-56, doi:10.1016/0924-2031(95)00027-r (1995).
106 Hashimoto, K. Ultrastructure of the Human Toenail I. Proximal Nail Matrix. *J. Invest. Dermatol.* **56**, 235-246, doi:http://dx.doi.org/10.1111/1523-1747.ep12260883 (1971).
107 Venkatarayudu, T. The rule of mutual exclusion. *J. Chem. Phys.* **22**, 1269-1269 (1954).
108 Fang, J. Y. *et al.* Transdermal delivery of macromolecules by erbium : YAG laser. *J. Control. Release* **100**, 75-85, doi:10.1016/j.jconrel.2004.08.009 (2004).
109 Bachhav, Y. G., Heinrich, A. & Kalia, Y. N. Controlled intra- and transdermal protein delivery using a minimally invasive Erbium:YAG fractional laser ablation technology. *Eur. J. Pharm. Biopharm.* **84**, 355-364, doi:10.1016/j.ejpb.2012.11.018 (2013).
110 Scheiblhofer, S., Thalhamer, J. & Weiss, R. Laser microporation of the skin: prospects for painless application of protective and therapeutic vaccines. *Expert Opin. Drug Deliv.* **10**, 761-773, doi:10.1517/17425247.2013.773970 (2013).
111 Yu, F. & Knight, J. C. Negative Curvature Hollow-Core Optical Fiber. *IEEE J. Sel. Top. Quantum Electron.* **22**, 10, doi:10.1109/jstqe.2015.2473140 (2016).
112 Esenaliev, R., Oraevsky, A., Rastegar, S., Frederickson, C. & Motamedi, M. Mechanism of dye-enhanced pulsed laser ablation of hard tissues: Implications for dentistry. *IEEE J. Sel. Top. Quantum Electron.* **2**, 836-846, doi:10.1109/2944.577306 (1996).
113 Hou, W. C., Chang, W. H. & Jiang, C. M. Qualitative distinction of carboxyl group distributions in pectins with ruthenium red. *Bot. Bul. Acad. Sin.* **40**, 115-119 (1999).
114 Garvie-Cook, H. *Micro- and Nano-scale Assessment of*

Novel (Trans)dermal Drug Delivery

Strategies, University of Bath, (2014).
115 Iftimia, N. *et al.* Combined reflectance confocal microscopy/optical coherence tomography imaging for skin burn assessment. *Biomed. Opt. Express* **4**, 680-695, doi:10.1364/BOE.4.000680 (2013).
116 Vo, L. T. *et al.* Autofluorescence of skin burns detected by fiber-optic confocal imaging: Evidence that cool water treatment limits progressive thermal damage in anesthetized hairless mice. *J. Trauma-Injury Infect. Crit. Care* **51**, 98-104, doi:10.1097/00005373-200107000-00016 (2001).
117 Baias, M. *et al.* Thermal Denaturation of Hydrated Wool Keratin by H-1 Solid-State NMR. *J. Phys. Chem. B* **113**, 2184-2192, doi:10.1021/jp8094616 (2009).

118 Vogel, A. & Venugopalan, V. Mechanisms of pulsed laser ablation of biological tissues. *Chem. Rev.* **103**, 577-644, doi:10.1021/cr010379n (2003).
119 Paltauf, G., SchmidtKloiber, H. & Guss, H. Light distribution measurements in absorbing materials by optical detection of laser-induced stress waves. *Appl. Phys. Lett.* **69**, 1526-1528, doi:10.1063/1.117993 (1996).
120 Saner, M. V., Kulkarni, A. D. & Pardeshi, C. V. Insights into drug delivery across the nail plate barrier. *J. Drug Target.* **22**, 769-789, doi:10.3109/1061186x.2014.929138 (2014).
121 Wang, J. C. T. & Sun, Y. Human nail and its topical treatment: Brief review of current research and development of topical antifungal drug delivery for onychomycosis treatment. *J. Cosmet. Sci.* **50**, 71-76 (1999).
122 Rzhevskiy, A. S., Guy, R. H. & Anissimov, Y. G. Modelling drug flux through microporated skin. *J. Control. Release* **241**, 194-199, doi:10.1016/j.jconrel.2016.09.029 (2016).
123 Crank, J. *The mathematics of diffusion*. (Clarendon Press, 1975).
124 Palliyil, B. B., Li, C., Owaisat, S. & Lebo, D. B. Lateral Drug Diffusion in Human Nails. *AAPS PharmSciTech* **15**, 1429-1438, doi:10.1208/s12249-014-0169-9 (2014).